Design and Validation of High-Bandwidth Fuel Injection Systems for Control of Combustion Instabilities

by

Jonathan A. DeCastro

Thesis submitted to the Faculty of the
Virginia Polytechnic Institute and State University
in partial fulfillment of the requirements for the degree of

Master of Science
in
Mechanical Engineering

Approved:

William R. Saunders, Chair

Uri Vandsburger

Donald J. Leo

February 2003
Blacksburg, Virginia

Keywords: thermoacoustic instabilities, atomization, fuel modulation, compressibility, piezoceramic actuator, lean premixed

Design and Validation of High-Bandwidth Fuel Injection Systems for Control of Combustion Instabilities

Jonathan DeCastro

Abstract

The predictive design of fuel injection hardware used for active combustion control is not well established in the gas turbine industry. The primary reason for this is that the underlying mechanisms governing the flow rate authority downstream of the nozzle are not well understood. A detailed investigation of two liquid fuel flow modulation configurations is performed in this thesis: a piston and a throttle-valve configuration. The two systems were successfully built with piezoelectric actuation to drive the prime movers proportionally up to 800 Hz.

Discussed in this thesis are the important constituents of the fuel injection system that affect heat release authority: the method of fuel modulation, uncoupled dynamics of several components, and the compressibility of air trapped in the fuel line. Additionally, a novel technique to model these systems by way of one-dimensional, linear transmission line acoustic models was developed to successfully characterize the principle of operation of the two systems. Through these models, insight was gained on the modes through which modulation authority was dissipated and on methods through which successful amplitude scaling would be possible. At high amplitudes, it was found that the models were able to successfully predict the actual performance reasonably well for the piston device.

A proportional phase shifting controller was used to test the authority on a 40-kW rig with natural longitudinal modes. Results show that, under limited operating conditions, the sound pressure level at the limit cycle frequency was reduced by about 26 dB and the broadband energy was reduced by 23 dB. Attenuation of the fuel pulse at several combustor settings was due to fluctuating vorticity and temporal droplet distribution effects.

Acknowledgements

First and foremost, I would like to thank Dr. William Saunders for sharing his passion for this work with me. As mentor, he taught me a great deal about more than the subject matter at hand. I had the benefit of his patience and tireless enthusiasm throughout this endeavor as we discussed and worked through each theory, problem, and idea. He also gave me many opportunities for growth as a professional, giving me some time to work at NASA Glenn and allowing me to take on some key responsibilities.

I would also like to thank Dr. Uri Vandsburger for his advice with various aspects of the project as well as for a good chat about politics and the weather. In particular, the early stages of this work were greatly influenced by his comments and suggestions to the design class and myself. Drs. William Baumann and Donald Leo have both been excellent instructors and valuable resources for my understanding of dynamic systems and control theory.

I owe a debt of gratitude to the folks at NASA Glenn, who have sponsored this work under an NRA grant, and where I spent part of my summer cross-pollinating our research efforts. I want to thank Joseph Saus for showing me the ropes and being a gracious host during my stay. Clarence Chang provided me with various tidbits of knowledge that have definitely peaked my interest in gas turbines.

This work could not have been done without the help of some key players. In particular, I want to thank Wajid for support with the combustor at the VACCG Lab, Noah for

building and testing the valve, Ernie for his work with characterizing the piston, Jonathan for his work with compressibility, and the 2001-2002 ME Senior Design Class for lending a helping hand in putting together the valve system.

My office mates have always been good co-workers, but have also grown to be good friends during my studies here. I would like to thank Aaron, Dave, Jonathan, Matt and Noah for their encouragement and support while adding levity to the work environment.

Lastly, I would like to thank my loved ones for always being there: Mom, Dad, and Cheryl. As usual, they offer their moral (and financial) support, fill my life with humor and goodness, and bring me down to earth when the going gets rough.

Blacksburg, Virginia — Jonathan DeCastro

February 2003

Contents

List of Figures

List of Tables

Nomenclature

Symbol	Description
a	Channel radius
	Constant
A	Complex acoustic pressure amplitude (forward traveling)
	Hydraulic area
A/F	Mass basis air-fuel ratio
b	Channel radius
B	Complex acoustic pressure amplitude (reverse traveling)
c	Phase speed
C	Electrical capacitance
	Fluidic capacitance
C_d	Orifice discharge coefficient
C_v	Flow coefficient
d	Diameter
f	Frequency
	Force
FN	Flow number
i	Electrical current
j	Imaginary number
k	Stiffness
	Wavenumber $\left(\frac{\omega}{c}\right)$

Symbol	Description
L	Element length
m	mass
	Number of elements on the inlet
M	Total number of elements
n	Number of elements on the outlet
N	Total number of boundaries
p	pressure
P	Perimeter
PM	Percent modulation: flow basis
q	Heat release rate
Q	Volume velocity
R	Rayleigh Index
	Acoustic resistance ($Re\{Z\}$)
s	Laplace variable
S	Cross-sectional area of an element
SG	Specific gravity $\left(\frac{\rho}{\rho_{H_20}}\right)$
t	Time
	Film thickness
T	Period of oscillation
	Transmitted acoustic power
u	Particle velocity
v	Specific volume
V	Voltage
	Air bubble volume
x	Linear displacement
X	Displacement amplitude

Symbol	Description
	Acoustic reactance ($Im\{Z\}$)
Z	Acoustic impedance
Z_f	Mean gradient impedance
Z_j	Junction impedance
Z_m	Mechanical impedance
Z_L	End Impedance
α	Absorption coefficient
	Ratio of film sheet area to air core area
γ	Specific heat ratio
θ	Valve seat angle
λ	Thermal conductivity
μ	Dynamic viscosity
ρ	Mean fluid density
ρc	Specific acoustic impedance
τ	Pure time delay
	Rise time
ϕ	Equivalence ratio
ω	Angular frequency
∇	Gradient operator
∇^2	Lapalcian operator

Superscripts & Subscripts

Symbol	Description
$(\cdot)'$	Perturbed quantity
$\bar{(\cdot)}$	Mean or steady-state quantity
$(\cdot)_0$	Absolute or reference quantity
$(\cdot)_o$	Orifice quantity
$(\cdot)_p$	Pipe quantity
$(\cdot)_l$	Liquid property
$(\cdot)_g$	Gaseous property
$(\cdot)_{max}$	Peak or maximum quantity
$(\cdot)_{in}$	Inlet quantity
$(\cdot)_{out}$	Outlet quantity
$(\cdot)_1$	Upstream quantity
$(\cdot)_2$	Downstream quantity

Chapter 1

Introduction

1.1 Background and Motivation

With the fairly recent implementation of standards on gas turbine engine combustion emissions, operation of these engines must occur in more lean regimes. Specifically, lean conditions reduce the temperature of the flame, thus reducing the energy released by combustion to below the activation energy of nitrogen oxides (NOx). With the new initiative for lean combustion, the AGTSR and UEET programs were started, which spawned new concepts for low-temperature combustion. Lean, premixed, pre-vaporized (LPP) injection provided for the best reduction in emissions, but suffered from stabilization problems such as flashback and auto-ignition due to excessively high pressures. Lean direct injection (LDI) was developed to improve the practical issues with LPP injectors, namely by mixing and vaporizing the fuel inside the combustor region. In order for this to occur, atomization had to be improved. With 30 to 40 LDI injectors replacing every two conventional injectors, mixing would occur in a small region so that the resident burning time would be greatly reduced. An LDI injector array is shown in Figure 1.1 as developed by NASA Glenn Research Center.

Lean combustion allows small variations in equivalence ratio to lead to rather large variations in the instantaneous heat release rate. As a consequence, these engines exhibit a

Figure 1.1: An LDI injector array in a sector combustor at NASA GRC.

special form of self-excited resonant behavior known as thermoacoustic instabilities, which is a result of the heat release of the flame interacting with the acoustic field in the combustor. The fact that lean flames are more compact intensifies the source input, causing further encouragement of the instability. Reaching amplitudes of up to 10% of the mean pressure is not uncommon, therefore combustion instabilities have the unfortunate effect of causing damage to the lining of the combustor due to high cycle fatigue from both vibrational and thermal loading. In several cases, this has lead to catastrophic failure of the combustor [8]. These instabilities also have the effect of causing the flame self-stabilization limits to narrow, increasing susceptibility for blow-off or flashback to occur during normal operation.

Thermoacoustic instabilities are a form of self-excited feedback that occurs if the phasing of the acoustics and the heat release are such that they excite one another. In terms of stability margins, a limit cycle oscillation occurs at a frequency where the phase of the open-loop transfer function is equal to zero or 180 degrees. Lord Rayleigh developed his criterion in 1878 to describe the dependence of the phasing of heat release to acoustic

pressure. The Rayleigh index R is thus stated as:

$$R = \int_0^T p'(t)q'(t)dt \tag{1.1}$$

where $p'(t)$ is the oscillatory (acoustic) pressure at the flame location and $q'(t)$ is the oscillatory heat release. In words, the Rayleigh index is the integral of the product of the unsteady pressure and the unsteady heat release of a given system over one period of oscillation. When these two waveforms are in phase, R is positive and the amplitude increases; when the two are out of phase, R is negative and the amplitude is attenuated. The system is driven unstable when fluctuations in heat release are commensurate with the pressure at the flame location, according to this criterion. In order for these instabilities to occur, one can see that another mechanism must somehow encourage the oscillation. The acoustic properties of the combustor indeed create the necessary coupling if the standing waves allow the Rayleigh index to be positive. The acoustics play a role by the simple fact that if, at the location of the flame, the unsteady velocity excites the heat release such that it is in phase with acoustic pressure, then a thermoacoustic feedback system results. Of course, the heat release lags the velocity by a combustion time delay τ, which is important in finding the location of the flame with respect to the mode shapes of the combustor.

For the simple case of the Rijke tube represented in Figure 1.2, the velocity points upwards, so the flame must be placed in the bottom-half of the combustor in order to be unstable. With reference to Figure 1.3, the reason for this phenomenon is apparent. If the flame is located at the bottom half of the tube ($x < 0$), the phase of the velocity lags the pressure by 270 degrees. However, if the flame is in the top-half ($x > 0$), that velocity lags by 90 degrees. If the combustion delay, τ, lags in phase by less than 180 degrees, R is positive for ($x < 0$) and unstable oscillations result, with the best phasing being at 90 degrees. If τ were greater than 180 degrees, the instability would be attenuated at the bottom half and excited in the top half of the tube. For many real systems, the phase relationship between velocity and heat release is difficult to determine due to the complexity of the physical mechanisms and is the subject of ongoing research [22].

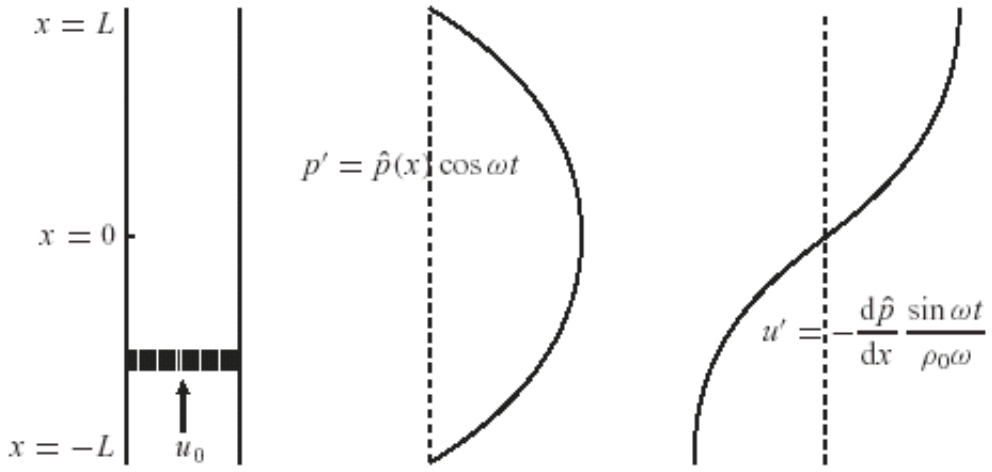

Figure 1.2: Diagram of the acoustic pressure and velocity characteristics of a Rijke tube [37].

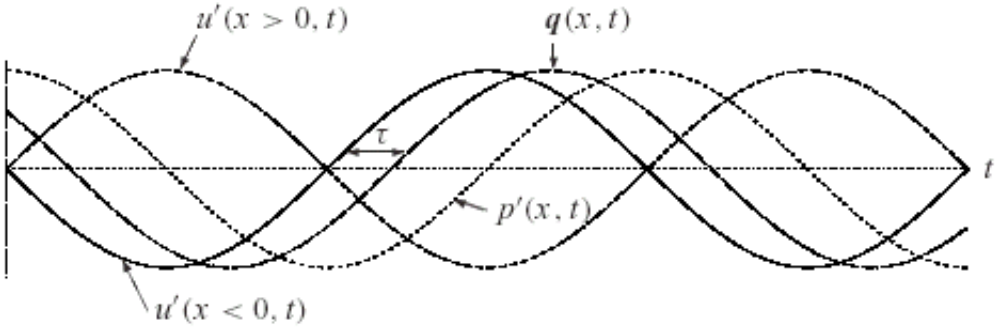

Figure 1.3: Diagram of the effect of combustion delay time on Rayleigh's criterion [37]. The heat release profile $q(x,t)$ shown is a result of the velocity $u'(x<0,t)$.

Other instability mechanisms than those generated by acoustics are present in the literature, such as: hydrodynamic effects due to bluff-body vortex shedding [35], and shock wave-induced instabilities. For the case of the Virginia Active Combustion Control Group (VACCG) liquid fuel combustor considered in this research, and many gas turbine combustors, the longitudinal modes of the system provide the coupling to promote the instability. Based on the measured frequency content of the instability, the VACCG combustor excites quarter wave modes, despite geometrical evidence that suggests that half wave modes exist

within the domain. The reason this is the case is because the entrance boundary possesses a large impedance. The combination of the area discontinuity, temperature gradient, droplet interaction, and combustion products all produce a cumulative effect of reflecting acoustic waves. Near-field evanescent effects caused by the steep temperature gradient are also shown to have an effect on the acoustics, as outlined in Khanna [22]. Thus determining the acoustics of the combustor systems is quite complicated, even for simplified tube combustor geometries. Another implication of this setup is that the Rjike tube instability mechanisms are not intuitive as to the source effect of the flame. One theory is that the phase between velocity and heat release is greater than 180 degrees due to a characteristic of the heat release transfer function. The complexity makes prediction of thermoacoustic instabilities quite difficult.

Much work has been done to develop strategies for passive and active control to suppress combustion instabilities. Passive control strategies have involved altering some aspects of the geometry of an existing combustion chamber in an attempt to reduce the acoustic modal influence on the instability. This has been accomplished by adding baffles and Helmholtz resonators to remove the energy at a particular frequency [13]. Another approach was to incorporate a linear array of injectors to shape the magnitude such that gain is at a minimum at the unstable frequencies [40]. Although these strategies offer some success, the designs are limited by the fact that they offer little robustness in attenuating the instability over a broad range of operating conditions. Moreover, each strategy requires a geometrical change to the combustor, and thus is not a viable option for space-limited combustors in aircraft engines. The approach that has been most widespread in combustors nowadays has been to simply map the high-oscillation operating points of the combustor, then to manage the operating envelope to circumvent those conditions.

In order to offer a robust control of thermoacoustic instabilities, focus has shifted in the last ten years toward active control techniques. To have active control, an element in the feedback loop between the acoustics and heat release must be actively intervened; that is, an actuator must impart some control upon the loop with reference to the signal provided

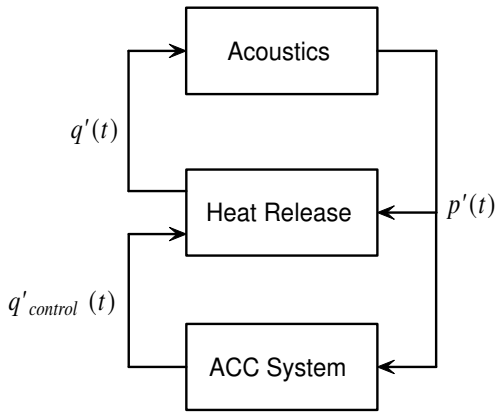

Figure 1.4: Self-excited feedback loop between heat release and acoustic plants with fuel injector-based ACC.

by some sensing device. Actuation of the acoustic field has been performed in the past, but a much more practical means of control is achieved by modulation of the fuel supply, which has the direct effect of controlling the heat release portion of the system as shown in Figure 1.4. Active control methods are the better alternatives than passive ones in terms of size and weight efficiency, especially in aero applications. With recent advancements in actuation and sensing technologies, these devices are moving towards implementation in the development cycles of high-performance engines. Industrial gas turbines are also in need for these devices, albeit they have completely different needs than aero engines.

The focus of the present work is to assess the dynamics of two of the most prominent fuel injection concepts used in the literature with respect to their ability to modulate the heat release rate. The two concepts, basically piston and throttle valve devices, were built and modeled in the hopes in developing tools for future designers in the optimal design of such devices given certain combustor specifications. It will be shown that the injection systems can be successfully modeled using linear theories, but the fuel flow in the combustion follows dynamics that are extremely complex to predict through modeling efforts. Several of the concepts developed thus far are outlined in the next section.

1.2 Literature Review

It is a requirement of any original research endeavor to identify the areas of work already performed in the specific research area so that it is clear to the reader how the present developments fit with these areas. In particular, the ACC systems developed herein are based on concepts developed by other researchers in hopes to augment the current understanding of these systems to the extent that these authors may not have addressed.

1.2.1 Early ACC Techniques and Solenoid Actuation

The concept of active combustion control (ACC) techniques and controller design was done at first by using loudspeaker actuators to modulate the acoustic pressure in laboratory scale combustors. In these early studies, McManus et al. [30] used a driver that excited the shear flow, requiring 30 W of electrical power to impart control on a 100-kW turbulent combustor rig. These studies proved successful because it showed that proportional control was effective but, aside from this fact, the actuator sizes were largely impractical for the end application.

Numerous attempts have been made in the literature to impart active control by modulating the heat release rate. One of the earliest active control effort to date was the work performed at Cambridge by Bloxedge et al. [5] in 1988. In this work, a mechanical shaker was used to modulate the incoming air flow to a 250-kW combustor. The results showed that a 20 dB reduction of the 88 Hz limit cycle frequency and a 11% reduction in overall energy of the combustor pressure response resulted. The novel technique proved the potential of a technique other than one that involved control of the acoustic field by loudspeaker actuators. However its power consumption shortcomings were still apparent, as the actuator required 300 W of electrical power to impart sufficient gain at the instability frequency.

To address the capability of fuel injection at a frequency and amplitude to establish control by way of heat release, the work by Langhorne, et al. [26] became extremely valu-

able for the efforts to come. In 1990, he used four Bosch solenoid-actuated injectors on a secondary, liquid fuel line to impart pulsations on a 3% addition of fuel, where the inlet was immediately upstream of a flameholder within a tube combustor. A zero-mean trigger was used to transform a filtered sine wave to the square wave necessary to command the solenoids in order to obtain control of a 250-kW combustor with a limit cycle frequency of 75 Hz. A 12 dB of reduction of the combustor pressure was achieved on the 164-dB SPL fundamental peak, which led to an 18% reduction of the broadband energy. The significance of this work was that this actuation scheme was one of the first of its kind to involve fuel modulation to establish control of an inherently unstable combustor.

In an attempt to achieve greater modulation amplitudes given a small-displacement actuator, Hantschk et al. [15] explored the possibility of augmentation of the incoming fuel pulse by means of acoustic tuning of the fuel line. Tuning the fuel line's length up to the atomizer was achieved by way of a simple eigenvalue analysis based on assumptions made on the boundaries. A MOOG DDV servo valve was used to actuate the system, as shown in Figure 1.5. The 137-kW combustor system was operated such that a limit cycle frequency produced a sound pressure level of 153 dB at 275 Hz. As a result of control, the limit cycle amplitude was be reduced by 30 dB. It was not known how well the acoustic tuning affected the system, nor the amount of amplitude on the flow that was achieved.

This was an improvement to the methods proposed previously, where either a loudspeaker or inlet air flow actuation was used to modulate the equivalence ratio. However, solenoids pose a problem for ACC for several reasons. The achievable bandwidth is extremely limited due to the inertia of the prime mover. In the case of Langhorne et al, the Bosch injectors had an achievable bandwidth of 140 Hz, which was sufficient to control the in-house combustor rig. In the research efforts by Hantschk et al, a dynamically optimal servo valve was used, developed by MOOG Corporation. This valve reportedly had a bandwidth of 450 Hz, the highest of all solenoids used in the literature, and allowed for modulation up to 26 gpm. Another limitation of solenoid actuation is proportionality. Although it was not reported in the findings of the time, it has since been shown that digital, or on-off, control

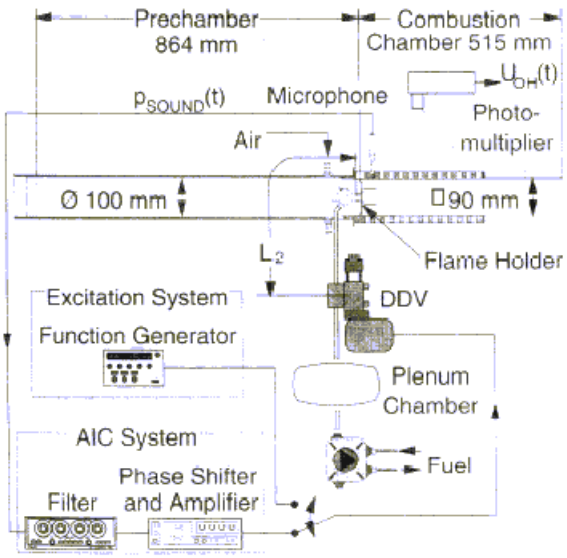

Figure 1.5: Schematic of fuel injection system used in Hantschk et al. [15].

is wasteful in terms of actuation energy for several reasons outlined in Carson et al. [6].

1.2.2 Proportional Actuation of Fuel

Studies relating to proportional control were done by researchers such as Hermann et al. [18]], who, in 1996, reported on the design of a fuel injector that proved successful control of an unstable combustor. In that work, a piezoelectric actuator with a bandwidth of 1000 Hz was used to drive a valve/piston combination in order to attain control of a 36-kW liquid fueled turbulent burner. Along the same lines as Hantschk's work, Hermann tuned the fuel line to appropriate frequencies to augment the modulation levels created by the actuator, as can be seen in Figure 1.6. A phase-shifting controller was used to impart closed-loop control of the system. This actuation method proved useful for the control of a 145-dB SPL, 360-Hz instability by 40 dB. Researchers such as Heising et al. [17], who used a Teflanol-D magnetostrictive actuator to modulate a valve, continued on the path of proportional modulation by attempting to modulate at each of the system modes within the actuator's bandwidth of 400 Hz. In 1994, Dressler et al. [10] used a voice coil actuator to drive a

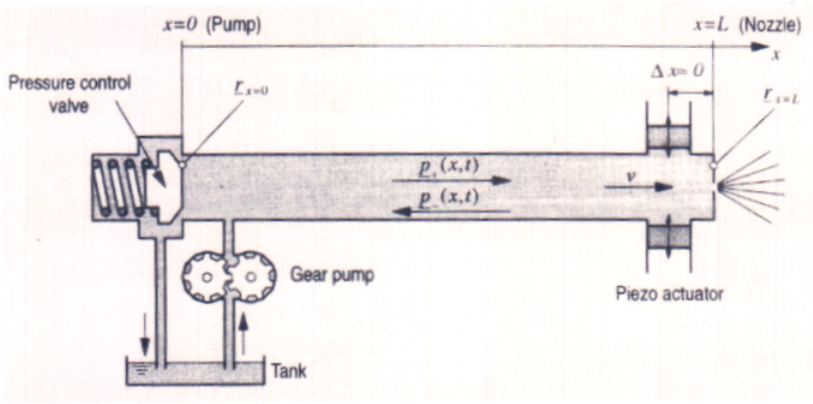

Figure 1.6: Schematic drawing of the acoustic system used by Hermann et al. [18].

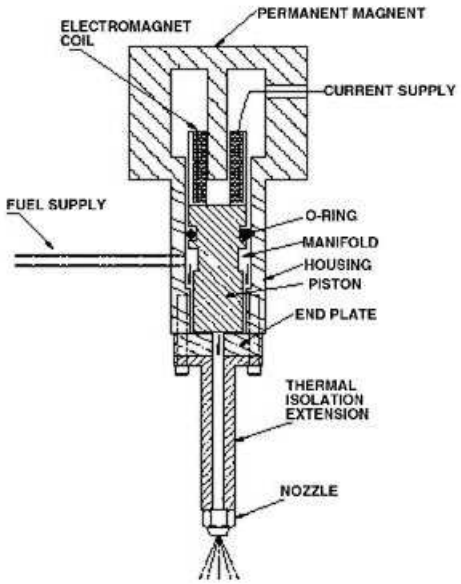

Figure 1.7: Drawing of a modulating piston device driven by a voice coil actuator used by Dressler et al. [10].

piston that would modulate the flow through a pressure-swirl atomizer, with an achievable bandwidth of at least 8 kHz. Success in the performance of this device in a small-scale combustor has lead to scaled experiments for use in suppressing instabilities in larger, sector combustors. A drawing of the scaled version of this piston device with a voice coil driver is shown in Figure 1.7

Several of the fuel injection modulation techniques employed above, including Langhorne, Hermann, and Heising, used secondary fuel injection which, strictly speaking, means the fuel is injected using a nozzle at a location sufficiently close to the flame to incur as little residence time in the combustor as possible. The secondary injector allows fuel to pass through the nozzle only when combustion control is on, modulating slightly above the mean flow rate. In so doing, the waveform entering the combustor has less chance to dissipate due to vorticity shedding and turbulence, as outlined in research work done by Yu et al. [42] and Munt et al. [32], thus transmitting more energy to the flame. In addition, these methods allow the fuel injector to modulate with a small portion of the fuel instead of the entire amount, which, in theory, would require less actuation authority. As pointed out in [26], secondary fuel injection is impractical for use in many premixed combustors. Instead, actuation on the primary line, or a secondary branch within the primary line, would utilize the existing main fuel atomizer.

1.2.3 Spray Diagnostics of Fuel Modulation

Studies on the effects of dynamic droplet breakup and dynamic mixing processes effects of the fuel pulse inside the combustor must be investigated in great detail before the performance of modulated injectors can be known, especially with the advent of lean direct-injection (LDI) injection schemes, where mixing and vaporization occurs before entering the combustion region. A drawing of one configuration of the LDI concept is shown in Figure 1.8, from work by Cooper et al. [7] in 2000.

Researchers such as Haile et al. [14], embarked upon such an investigation in 1998, in which the flow characteristics downstream of the atomizer was studied to determine how droplet distribution is affected by modulated flow. These droplet measurements were gathered using particle image velocimetry (PIV) and phase Doppler anemometry (PDA). The results showed that fuel modulation does not affect the distribution of droplet size significantly, as shown in Figure 1.9. Key in this study was that fuel modulation was measured

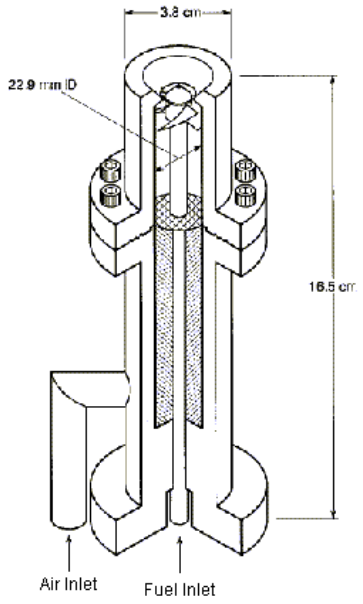

Figure 1.8: Drawing of one realization of an LDI nozzle. [7].

upstream of the valve by means of a pressure transducer and a hot-film anemometer. It was not reported how this upstream velocity differed from the ultimate velocity at the atomizer, leaving some question about the assertion of the distribution "smearing" effect.

Research work performed by Neumeier et al. [33], also in 1998, lead to different results that that obtained from Yu, whose findings suggested that atomization quality improved as modulation was imparted. For these experiments, the throttle valve injector used in [16] was used to modulate diesel fuel at 2400 Hz. A Phase Doppler Particle Analyzer (PDPA) was used to measure the droplet and velocity characteristics of the flame. From the data in Figure 1.10 (a), it can be seen that the mean droplet diameters decrease as the fuel is modulated. However, it can be seen in Figure 1.10 (b) that the mean velocity increases with modulation, and it was not made clear in the discussion whether or not the mean flow rate through the atomizer was held fixed. An increase in the mean flow would definitely be one cause of a decrease in the droplet diameter, which is an inherent property of pressure atomizers.

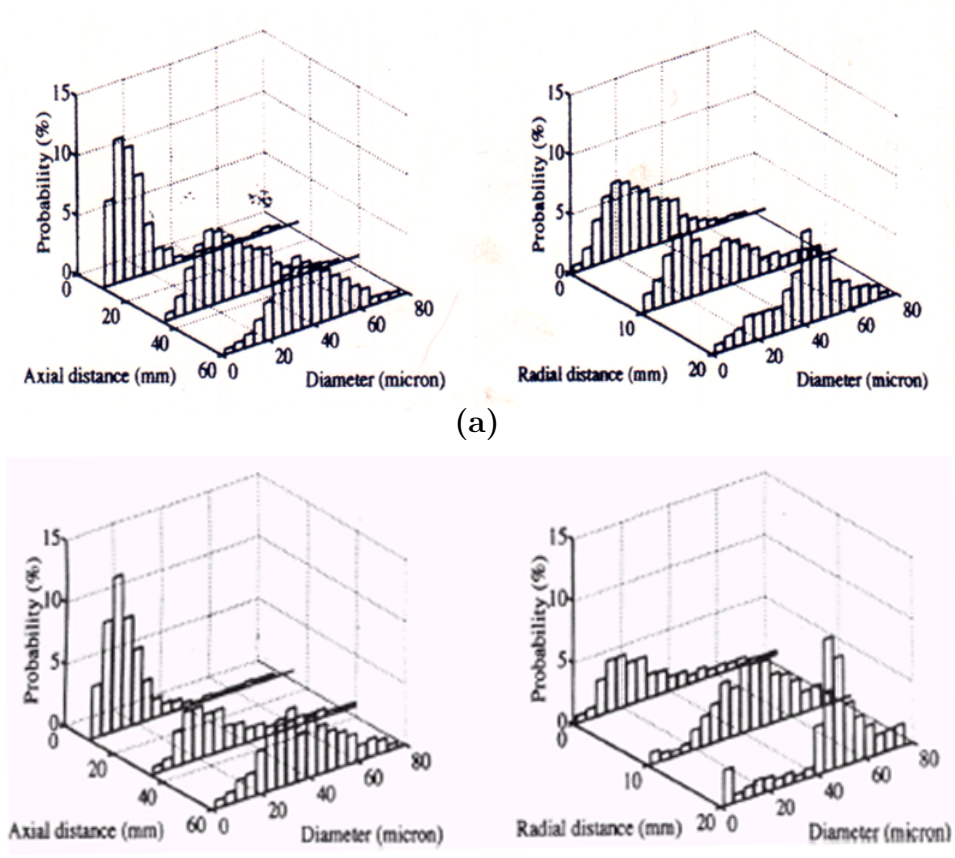

Figure 1.9: Droplet distribution at (a) steady flow and (b) 60 Hz from studies by Haile et al. [14]

1.2.4 Literature Review Summary

In the literature, it has been seen that injection schemes have mainly been of two types: primary or secondary fuel line actuation. The reasons for choosing either application were usually for practical reasons in particular laboratory rigs in question. In addition, it was noticed that the actuation devices have constituted either medium- to high-bandwidth valves or pistons. With a few notable exceptions, these valve devices were mostly solenoid-operated, which may suit the present need, but were of limited capability of being scaled. As outlined above, researchers such as Hermann, Heising, and Dressler were among the few to address solenoid limitations by incorporating proportional, high-bandwidth actuation. To

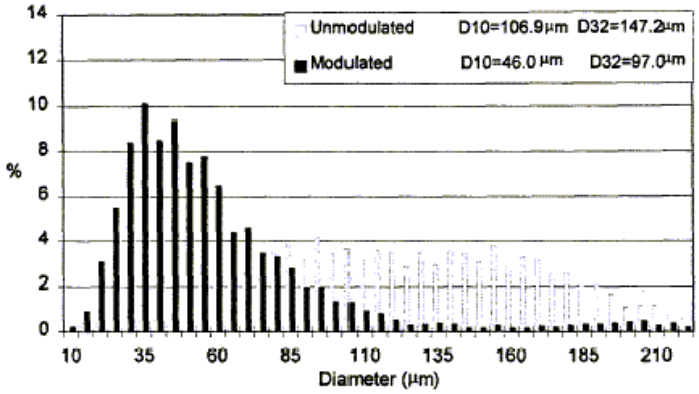

(a)

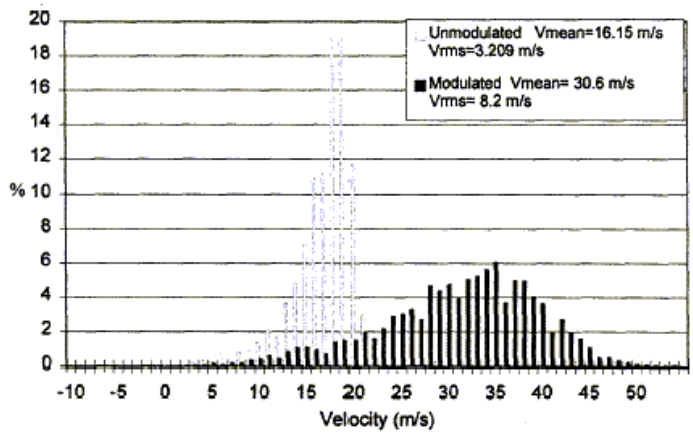

(b)

Figure 1.10: Histograms of (a) droplet distributions and (b) velocity distributions under modulated and un-modulated conditions reported by Neumeier et al. [33]

take performance a step further, researchers such as Hermann and Hantchk designed the fuel delivery system to possess acoustic properties such that amplification of the waveform would be possible, which was a novel technique. However, research in the literature has not provided conclusiveness on the dynamic effect of the fuel delivery line in actual gas turbine applications.

To be certain, proportional modulation is arguably a better option for ACC systems from the standpoint of energy requirements as well as that for control algorithm development.

While practical use of these systems is contingent on optimizing the package size and power requirements, no author has succeeded in developing useful design tools for the intention of performance-based design. It is the intent of this thesis to address such issues from a standpoint that involves end applications in actual-sized, liquid fuel gas turbines using tools that would determine their performance with a minimal set of experiments.

1.3 Research Objectives

In the present work, the objective is to develop *high-bandwidth, proportional* ACC hardware with both throttle valve and piston/check valve configurations for specific application to liquid-fueled combustors. The piston device was designed for use as a primary line fuel modulator, while the throttle valve was designed for either primary or secondary line modulation. The two fuel injectors were built with the intention of studying various authority benchmarks: the achievable velocity amplitude, the modulation bandwidth, and the overall performance as the operating parameters change. Ultimately, assessment of the performance of these fuel injector systems was done by examining their ability to control the heat release of a laboratory-scale swirl stabilized combustor.

A second goal of this research was to develop design methodologies to minimize the experimentation involved with fuel injector development in order to facilitate ACC implementation in gas turbine combustors. This modeling was performed using a one-dimensional acoustic transmission line approach, using linearized impedances and source inputs based on first principles. Although finite-element packages may provide a more accurate model of these systems, they may not generate the level of understanding required to optimize several components of the system. By developing these simple models, the fuel injection systems may be characterized at actual engine operating conditions that are too costly or time consuming to be reproduced on an experimental setup. Additionally, the models may be useful in optimizing several system components, such as the actuator and prime mover hardware, in producing a design with the desired authority. By taking advantage of the resonant con-

ditions of the fuel supply line, the steady-state velocity oscillations were maximized at the limit cycle frequency in the VACCG laboratory combustor. It is also hoped that the active combustion control community would benefit from these models because one would have the ability to couple these with models of the chamber processes and heat release to analyze the performance from a systems perspective.

Based on the literature to date, very little work has been done thus far to examine the actual fluctuating post atomizer velocity, and to study the complex dynamics between the atomizer and the flame. Thus the final goal of this work was to study the spray interaction with the combustor processes on an indirect basis by evaluating the fuel injector's performance in a combustion environment. Combustor control was performed in a 30-kW turbulent swirl-stabilized VACCG laboratory combustor fueled by kerosene. Experiments with a simple phase-shift controller were performed in order to validate the control authority of the injection systems that will be useful as a benchmark for future studies that will correlate fuel injector modulation to heat release.

1.4 Organization of Thesis

This thesis follows a logical progression of the research performed in order to achieve the goals set forth above. Chapter 2 outlines the analysis and design of the two fuel injector systems with identification of original design configurations and changes to those designs. The piston configuration is presented first: starting with a quasi-steady analysis, then moving to selection and construction of components, followed by preliminary testing results. The throttle valve development is presented next in a similar fashion. The acoustics of the system are discussed in Chapter 3, starting from general acoustic equations then moving to detailed models of the two systems. Model-based testing of the piston configuration is then presented, followed by that of the throttle valve. Along the way, several conclusions for the validity of the models and solutions to improve the authority of the two systems are addressed. Chapter 4 reveals the applicability of these models to high-amplitude conditions by comparing the

results of scaled models and experiments over a variety of operating conditions. The chapter also covers phase-shift instability control experiments on the VACCG laboratory combustor and mapping the control authority at several operating conditions. To conclude, Chapter 5 summarizes the current status of ongoing proportional injection investigations, where several conclusions are made with regard to the suitability of the two hardware configurations and the design methodologies explored in this research.

Chapter 2

Design and Development of Piston and Throttle Valve Systems

This phase of the thesis work was focused on developing fuel injector concepts that are based upon designs seen in ACC literature. The design considerations for these injector systems were based on the needs of the aero gas turbine industry, such as bandwidth, flow rates, and the existing fuel delivery system. However, the limited facilities with which to test these injection systems placed additional requirements on the flow rates and atomizer size. Throughout this research work, each of the limiting factors in conversion of the electrical actuation signal to the nozzle exit velocities will eventually be addressed. It is plain to see that the bandwidth of the actuator coupled with the prime mover is essential to this criterion, along with any reactive and dissipative effects on the fluid, such as compressibility and nozzle resistance. This will be dealt with in Chapter 3, where an acoustic analysis will be performed but, for the purposes of design, it is now assumed that quasi-static design strategies are sufficient if appropriate factors of safety are imposed on the design of each individual component. Because the major goal of this thesis research is to arrive at design methodologies that will circumvent ad-hoc approaches to design, the validity each design strategy must first be assessed.

This chapter will cover the process and methodology used to design two fuel injector concepts: a piston/check valve and a throttle valve arrangement. The two designs must

be mindful of several practical requirements that do not necessarily have specific metrics associated with them. The following is a list of several specific considerations that must be accounted for in the final designs:

- The ACC systems must, of course, be lightweight in size and have a small package volume in order to serve any practical value to the gas turbine industries.
- The designs must alter the existing fuel delivery line as little as possible and be suited for necessary placement at a location some distance away from the injection location.
- The equipment should not require power when the ACC system is inactive.
- All dominating transients should be nonexistent by a reasonable percentage of the time constant of the instability envelope, optimally a fraction of the instability period.
- The amplitude of modulation must be sufficient to bring the thermoacoustic poles to the stability regions and to maintain them in that region.
- The design must be robust enough to deal with changes in the physical parameters of the fuel and changes in pressures and flow.

Throughout the chapter, these design constraints are given careful attention and those with specific design metrics are associated with target specifications.

2.1 Target Specifications

Industry and government corporations that have a stake in high performance gas turbine engines often have a need to reduce thermoacoustic instabilities in their combustors. A list of target specifications for ACC systems is found in Table 2.1, which was compiled primarily based on discussions with personnel at NASA Glenn Research Center. NASA's ACC validation tests were performed on a United Technologies Research Center (UTRC)

sector test rig using three atomizers (there referred to as fuel injectors) associated with the three air inlet nozzles, which constitute the secondary flow path. This secondary line is modulated by a single fuel injection device, and is termed "tri-wall" fuel injection. The total flow number of all three injectors is 110, which means that 77 gph per atomizer is typical at a 300-psi pressure drop. The flow number FN is a commonly used metric for relating pressures to flow rates across an orifice with ease. For the remainder of this thesis, the following definition will be used:

$$FN = \frac{\rho Q}{\sqrt{\triangle p}} \qquad \left[\text{lb/hr}/\sqrt{\text{psi}}\right] \tag{2.1}$$

Appendix A contains a list of Delevan Inc. simplex atomizers used in this study with their respective flow numbers. Based on the flow number, nozzle characteristic curves can be generated, which relate the pressure required to impart a certain flow rate. Figure 2.1 shows the nozzle characteristic curves for several of these Delevan atomizers, revealing the nonlinear nature of the relationship. In accordance with convention used in the literature, the flow modulation in many instances throughout this thesis were determined by applying Equation 2.1 to the assumed pressure gradient across the atomizer. The validity of this assumption will be discussed in Chapter 3, but for now, the flow was estimated in this manner. The 700-Hz bandwidth specification in the table is a result of the fact that the instability modes are primarily longitudinal, not azimuthal, the latter of which are typically seen in gas turbine afterburners.

The VACCG kerosene-fueled, turbulent swirl stabilized laboratory combustor in which these combustion control experiments will be performed has limitations that prevents the target flow rates and pressures to be achieved. The specifications that were used for this study were based on a maximum power output of 90 kW on the test combustor, imposing a limit of 4 gph on the maximum fuel flow rate. However, the limit cycle frequency in this combustor is approximately between the range of 100 and 110 Hz. The rig was limited to atmospheric conditions due to practicality issues, but the fuel pump and atomizer will allow realistic pressure drops to be replicated. To that end, a Suntec Corp. gear pump was used

Table 2.1: Specifications required by ACC stakeholders.

Criteria	**Unit**
Bandwidth	Between 50 and 700 Hz
Mean Flow Rate (all injectors)	500 gph
Combustor Pressure	400 psi
Mean ΔP Across Atomizer	300 psi
Modulation Level	40% of mean
fuel Type	JP-5
Lifetime	2000 hrs
Number of Atomizers	20 - 30
Modulated Atomizers	10 - 15
Atomizer Flow Number	110 lb/hr/$\sqrt{\text{psi}}$ (37 lb/hr/$\sqrt{\text{psi}}$ per atomizer)
Fuel Injector Resistance	negligible

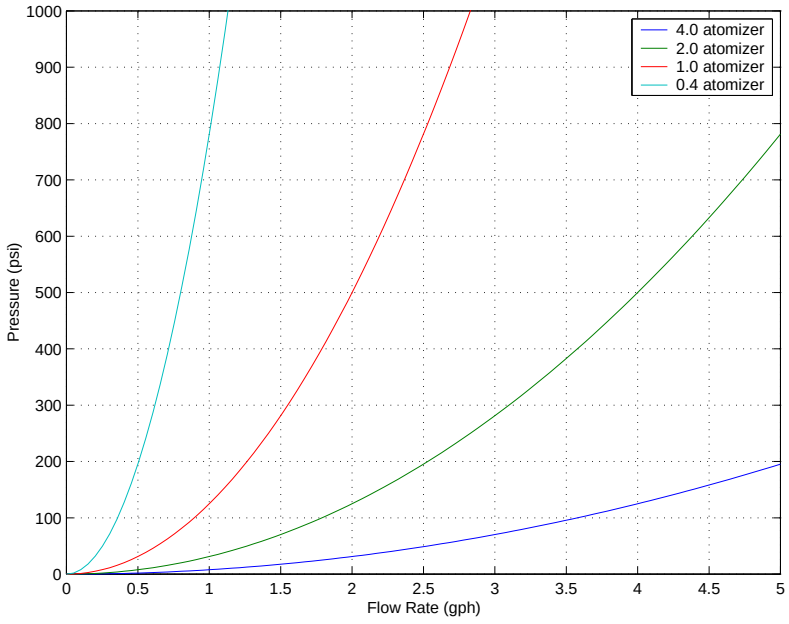

Figure 2.1: Nozzle characteristic curves for several Delevan atomizer models used in this study.

on the primary line that has a 300-psi operating pressure and a 27-gph maximum flow rate. In accordance with Figure 2.1, a reasonable compromise would be to use a 4.0 atomizer at a pressure of about 125 psi. Thus, the systems designed in this chapter will be limited to the above specifications, but will not hinder the argument of scalability potential.

2.2 Proportional Fuel Injection

The performance capability of a fuel injection system is very much the result of the proportionality of the fuel modulation, which is intimately dependent on the hardware components involved with the design. Earlier attempts in testing ACC fuel injection concepts involved using solenoid-actuated valves to modulate in a digital, or on-off, manner [26, 14], as outlined in Chapter 1. From an energy standpoint, modulation authority can be viewed as the power expended by an actuator at a given frequency to provide a certain open-loop gain. Because the energy required to control a limit-cycling instability is shown only to exist at the fundamental mode of the instability [6], square wave actuation wastes energy to the harmonics. Also, the fact that pulse-width modulation (PWM) techniques were used has adverse control effects, because the gain relationship at the fundamental frequency is nonlinear. Because control algorithms using a linear gain will benefit greatly from proportionality, this characteristic is desirable for ongoing research in adaptive control methods for ACC, such as that by Greenwood [12].

Although harmonic content is undesired, it is not completely necessary to obtain a signal that is identical in shape to the input waveform, if such a signal is unavoidable. It will be shown that harmonic content cannot be completely suppressed as amplitudes grow large, due in part to the fact that the nozzle characteristic is a nonlinear relationship. It will be assumed for the work, however, that the fundamental flow amplitudes are linear with respect to input voltage.

A generalized profile that is generally adopted by proportional ACC system designs is

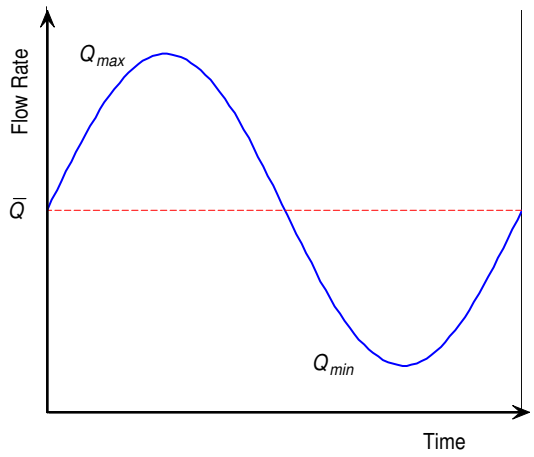

Figure 2.2: Typical flow profile of modulating fluid.

shown in Figure 2.2. The mean flow rate $\bar{Q}$ is unaffected by the onset of the fuel modulation, where the peak and trough values, again, are assumed linear with combustor pressure for proportional modulation. An important benchmark in fuel injection operation is the normalized amplitude of modulation, expressed as a percentage. The percent modulation PM is defined as the integral of the oscillatory component of volume exiting the nozzle over one period normalized to the mean volume:

$$\begin{aligned} PM &= 100 \cdot \int_0^T [Q(t) - Q_{min}]\, dt \\ &= 100 \cdot \frac{Q_{max} - Q_{min}}{2\bar{Q}} \end{aligned} \tag{2.2}$$

For a sine wave, the modulation is simply the flow rate amplitude normalized to the mean flow rate $\bar{Q}$. It is this proportional modulation principle that will be adopted for the remainder of this design. Based on the specifications provided by industry in Table 2.1, the target PM will be 40%.

2.3 Comparison of Primary and Secondary Fuel Line Actuation Concepts

Fuel modulation can be classified as either primary or secondary, where primary modulation is simply the term used to describe actuation imparted on the entire fuel flow entering an existing fuel atomizer [10, 18] Secondary fuel modulation is defined in the literature, such as Richards [36], to mean that modulation occurs in a fuel line that bypasses the primary line, which only experiences flow when the ACC system is active. Often, this also implies that a secondary atomizer is placed at an injection location closer to the flame. Because these devices experience only part-time flow, the motionless fuel within those atomizers tends to pyrolize due to excessive thermal loads that clog its narrow passages. Implementing this second atomizer becomes problematic in actual gas turbines, thus secondary modulation is a term used here to mean that the modulation occurs in a dedicated secondary branch that rejoins the primary line upstream of the atomizer.

The piston concepts outlined in Section 1.2.2 are best suited with primary modulation techniques, because the pumping action of the piston effectively creates an alternately positive and negative flow that results in a waveform with zero mean. The fact that piston components do not impart a pressure drop in the primary line make for easy implementation and also do not require throttle control of the mean flow rate. Little alteration in the existing fuel delivery system is needed because the hardware components are relatively simple, also minimizing potential failure modes of the fuel injector.

Secondary fuel modulation is characterized by actuation in a fuel line that bypasses the primary fuel line. In this respect, it is a requirement that nearly all of the secondary fuel must be modulated so that an excess of the mean flow is not experienced. The technique usually used to employ this modulation principle is by controlling the energy dissipation by throttling the flow [26, 33, 15]. A set of high-bandwidth valve devices must be used for this application: one actuating the primary, and one actuating the secondary. With reference to

Figure 2.2, the primary-line valve would actuate only to reduce the mean flow rate from $\bar{Q}$ to Q_{min} in the primary line, in accordance with the desired PM required by the controller. Modulation of the secondary line valve would create a sine wave with peak-to-peak flow rates between $Q_{max} - Q_{min}$ and zero with a mean of $\bar{Q} - Q_{min}$. It is clear that this practical realization of a secondary line throttle valve requires a much more complex setup than the piston arrangement, which is a disadvantage of this type of arrangement. To provide a flow rate Q_{max} in excess of the mean flow $\bar{Q}$ through the same atomizer, a second pressure source must used drive the secondary line in order to achieve Q_{max}. Due to the complexity of the setup, there may be an instance where the negligible pressure drop requirement may be relaxed in favor of a primary-line throttle valve arrangement. Only one pressure source would be needed to drive the system, with the valve constantly regulating the mean pressure.

In terms of scalability to higher flow rates, the piston assembly is faced with difficulty because the source is volumetric in nature. If a given piston injector were used in a higher-flow application with a given PM requirement, a larger amount of volume would need to be modulated each cycle. Obviously, this would require a design with a greater piston surface area or actuator displacement. It is possible that the energy and space requirements of the actuator and prime mover may become taxing and, as a result, may become difficult or impossible to implement. The throttle valve is relatively easy to scale to higher flow rates because all that is needed is a higher secondary supply pressure, allowing the valve's hardware to remain unchanged. Despite the greater number of components than the piston device, very little of the hardware has to be reconfigured in designing for different applications.

Because of inherent limitations in achieving a certain percent modulation at relatively large flow rates, the primary-line system was first designed with a flow requirement of 0.4 gph mean flow with a 0.4 atomizer, which was the typical mean flow operating condition for 9 kW thermal power in the VACCG combustor. Once the concept was tested and modeled, the components would be redesigned for use with higher flow conditions. Due to its ease in scalability, the throttle valve design would be given a higher flow modulation requirement. Thus, the mean flow would be 4 gph with a 4.0 atomizer, as stated in Section 2.1, providing

Table 2.2: Summary of target specifications for piston and throttle valve designs.

Criteria	**Piston/Check Valve Design**	**Throttle Valve Design**
Configuration	Primary Line	Primary or Secondary Line
Bandwidth	700 Hz	700 Hz
Modulation Level	40% of Mean Flow	40% of Mean Flow
Mean Flow Rate	0.4 gph	4 gph
Atomizer Flow Number	0.3 lb/hr/$\sqrt{\text{psi}}$	3 lb/hr/$\sqrt{\text{psi}}$

the potential for 90 kW of thermal power. Table 2.2 summarizes the target specifications for the two fuel injector designs.

2.4 Primary-Line Piston and Check Valve Development

Piston-based fuel injectors have been typically designed for fuel to enter the chamber of the piston with as little resistance as possible and exit axially to a tube leading to the fuel nozzle. As the piston modulates, concerns with a portion of the flow expelled during the forward stroke being lost to the supply line have called for an additional check valve to be placed immediately upstream of the inlet port to the piston chamber. In principle, this check valve would close when the piston is moved forward and open when the piston retreats. In this design, two high-bandwidth actuators would be chosen to drive two prime mover assemblies. The design methodology consisted of an analysis for individual requirements of the piston and check valve followed by the selection of appropriate components.

It should be noted that the actual effectiveness of the check valve under dynamic conditions must be thoroughly tested before an accurate justification can be made for its existence. If these hardware components can be minimized or eliminated, this would go a long way in fulfilling the space, weight and energy requirements of aero engines. This may be accomplished by substituting them with a simpler means of preventing transmission loss, such as an acoustic muffler. Thus, the effectiveness of such an alternative will be addressed

in Chapter 3, but for now, the check valve design was considered without regard to such alternatives.

2.4.1 Selection of Appropriate Piston Actuation Methods

A semi-qualitative assessment of candidate actuators was performed in order to narrow the criteria to aid in the designs of the prime mover assemblies. Besides proportionality, the actuators in question were required to exhibit a bandwidth of at least 700 Hz and either a high force or high displacement capability. Additionally, cost and robustness were important factors considered here to address feasibility. The proportional actuators that were considered for this design were: voice coil, piezoelectric, electrostrictive, and magnetostrictive.

Voice coils are typically used in speakers and mechanical shakers due to their high frequency capabilities. They operate based on Lorenz forces created by the interaction between a magnetic field and a coil with an induced current. Typically, they can provide fairly large displacements that are on the order of an inch, but generate forces that are limited by the size of the amplifier and the permanent magnet. For example, in order to generate 300 lbf, a 10-in diameter by 7-in height permanent magnet must be used, which is largely inefficient due to its size and weight.

Piezoelectric, electrostrictive, and magnetostrictive actuators are all linear devices that operate based on the piezoelectric effect: a force or strain is induced under the presence of an electric field. Magnetostrictive actuators require a magnetic field to create a strain, but require a bias field in order to modulate proportionally. They also tend to heat up significantly and must have either external cooling or a limited usage time. Both piezoelectric and electrostrictive materials require an electric field to cause a strain, however electrostrictives are not truly linear and require a bias field. Active materials have the advantage of high force generation, but are limited in the amount of displacement they can provide. Table 2.3 shows a qualitative comparison of the various actuators with solenoids included for comparison

Table 2.3: Comparison of various types of high-bandwidth actuators.

Actuator	**Bandwidth**	**Displacement**	**Force**	**Linearity**	**Power Consumption**	**Size**	**Cost**
Solenoids	450 Hz	Large: mm's	Smallest	On/Off	Small	Small	Low
Voice Coils	20 kHz	Large: mm's	Small	Linear	Large	Largest	High
Piezoelectric	10 kHz	Small: μm's	Large	Linear	Large	Med	High
Electrostrictive	10 kHz	Small: μm's	Large	Strain $\propto V^2$	Large	Med	High
Magnetostrictive	10 kHz	Small: μm's	Large	Linear	Large	Large	High

purposes.

Based on the table, voice coils and piezoelectric stacks offer about equal performance with regards to bandwidth and linearity. The displacement and force traits of piezoelectric materials are different from those of voice coils, but both have relatively high energy densities. It was expected that, in this application, a voice coil would be operated close to its maximum force limits, and thus be operated away from its optimal performance region. In addition, provisions would have to be made to increase the stiffness, as the piston and fluid's mass are likely to have an effect on the actuator's displacement and bandwidth. Thus piezoelectric actuators were chose to drive the piston assembly and check valve due to their favorable force characteristics.

One characteristic that makes piezoelectric stacks an attractive option is the ease through which their operation can be simulated. The force-displacement characteristic curve is a reliable method for determining if the actuator will be force limited during any portion of the cycle. As shown in Figure 2.3, the area under the area under a straight line between the actuator's free displacement and the blocked force describes the region where the stack may be operated. For the simple case where the stack is driving a spring with constant k_m, the maximum transfer of work between the actuator and the system results when the external stiffness is equal to the actuator's stiffness k_{act}. Of course, for the present application, other dynamics exist such as displacement of the mass and the oscillatory pressures at the prime mover. Thus the shaded box describes the region where the highest efficiency may be

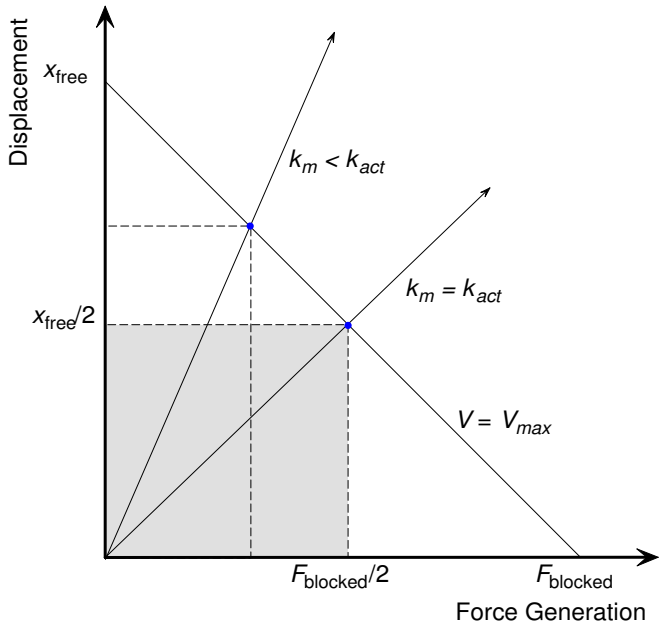

Figure 2.3: Force-displacement curve of a typical piezoelectric actuator with optimal efficiency region shown as the shaded box.

achieved, and will be targeted for each of the hardware designs.

2.4.2 Piston Assembly Analysis and Design

For a piston assembly to operate properly, it would be necessary that the piston push the required flow to achieve the required 40% modulation within the required frequency range. As outlined above, the piston fuel injection system was designed for a 0.4 gph mean flow rate with a 0.4 atomizer. The design parameters sought are the piston surface area, the actuator displacement, and the actuator force requirement. These parameters were found by way of a quasi-static simulation similar to that performed in Lagimoniere [25]

Conceptually, the piston's velocity is proportional to the flow rate through the atomizer. Essentially, a cosine wave must be generated in the displacement in order to produce a

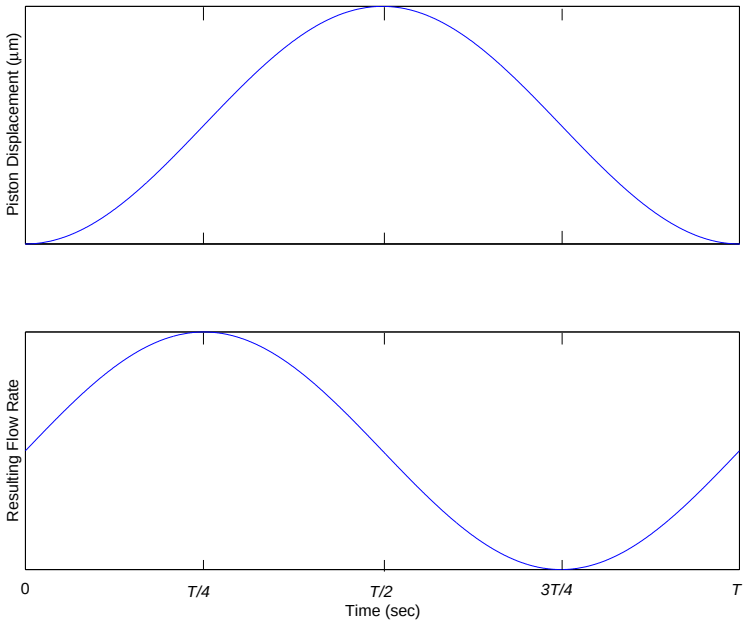

Figure 2.4: Conceptual input waveform to piston actuator and expected flow profile.

sine wave in the velocity. Expressions of the piston's displacement and velocity profiles are thus given by:

$$x(t) = X\cos(\omega t) + x_{bias}$$
$$v(t) = \omega X\cos(\omega t) \tag{2.3}$$

where X is the displacement amplitude provided by the stack and x_{bias} is the bias offset required to operate the stack given the amplifier saturates at zero. Because of the velocity amplitude's dependence on ω, the actuator is expected to be limited in providing the desired modulation as frequency goes to zero. Thus, the lower bound on the modulation capability of the fuel injector was arbitrarily set to 50 Hz. A plot of this input waveform and resulting flow profile is shown in Figure 2.4.

The flow at the atomizer is simply the sum of two time-dependent flow sources: one from the fuel pump and the other from the piston according to the following equation:

$$Q_a(t) = A_p v(t) + Q_p(t) \tag{2.4}$$

where A_p is the piston's surface area, $v(t)$ is the piston velocity from Equation 2.3, and $Q_p(t)$ is the supply flow acted upon by the check valve. In theory, the check valve's square wave signal creates a discontinuous supply flow rate, so the resultant flow rate is also expected to be discontinuous. When the check valve is completely closed, $Q_p(t) = 0$ and a positive-valued sine wave results in the flow for the first half of the period. During the second-half of the period, the check valve is fully open and $Q_p(t)$ is added with the negative-valued portion of the sine wave. The profile of the piston, check valve, and resulting pressure influence is shown in Figure 2.5, with the check valve's square wave signal included for reference. During the second half of the cycle, the flow rate goes actually goes below zero, but the waveform is clipped at zero flow. It should be noted that the mean flow (represented by the dashed line) is not decreased relative to the steady-state flow rate, which is an important characteristic of primary fuel injection systems. For this case, 100% modulation results because, during the second half of the cycle, the check valve is open and the piston induces a flow rate equal to $-A_p v(t)$.

Due to the clipping at zero flow, the mean flow rate is actually a function of the waveform's amplitude. This amplitude-dependent flow is plotted versus various peak-to-peak displacement amplitudes $2X$ and piston diameters A_p at a driving frequency of 50 Hz and a supply flow rate of 0.4 gph in Figure 2.6. Note that the mean flow rate reaches exactly one half of the supply flow rate, 0.2 gph, when the piston modulation becomes small enough that the signal is no longer clipped. After some iteration, a piston diameter of one inch was chosen, which calls for 16 microns to achieve a mean flow rate of 0.4 gph.

The maximum instantaneous force required of the actuator was determined from the pressure-flow relationship from the atomizer's flow number (Equation 2.1). At time $T/4$, the flow rate reaches its maximum value, which, for the case of a one-inch piston and a 16-micron peak-to-peak displacement, is equal to 1.21 gph. With the piston's area, one can solve for the instantaneous force given the peak pressure, found to be 576 lbf. Upon conducting a search through several piezoelectric stack vendors, the actuators provided by Piezomechanik GmbH were the most attractive for the present application. Namely, the actuators were

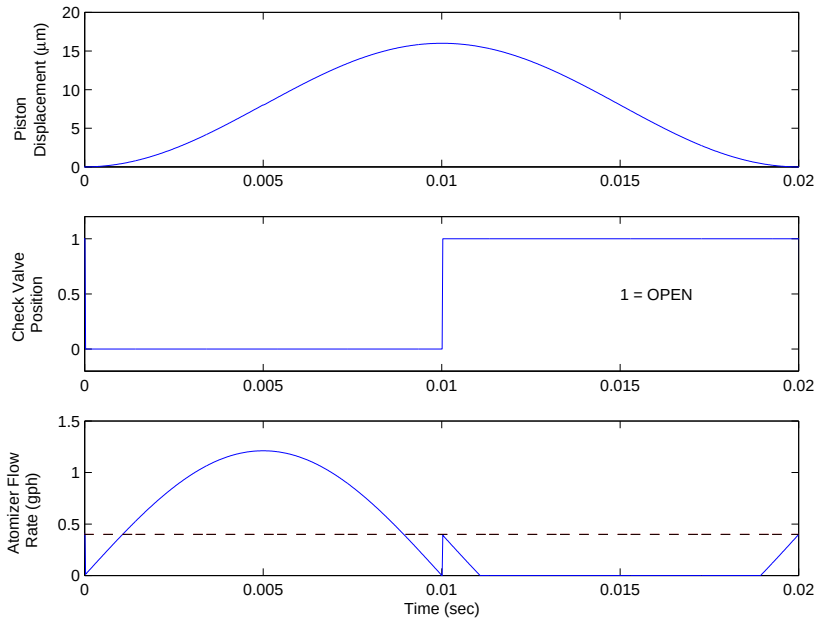

Figure 2.5: Quasi-steady flow waveform created by a piston/check valve combination at 50 Hz modulation. - - $\bar{Q} = 0.4$ gph.

outfitted with a pre-stress casing, allowing them to experience some amount of tensile force during its operation that would normally cause damage to the piezoceramic material. At high frequencies, such forces are expected with the inertia of the piston and fluid. The stack actuator chosen for the piston was that with model number PSt150/14/20, which possessed a 20-micron free displacement and a 1570-lbf blocked force. The specifications of this particular stack are well suited for this application because modulation takes place within the high-efficiency region of Figure 2.3.

In any high-voltage application, the power output of the amplifier is usually the limiting factor in frequency response. Specifically, the driving velocity is a function of the current input to the stack, which is governed by the electrical impedance relationship for an AC signal:

$$i_{max} = \omega C V_{max} \tag{2.5}$$

where V_{max} is the maximum voltage amplitude, C is the open circuit capacitance of the stack,

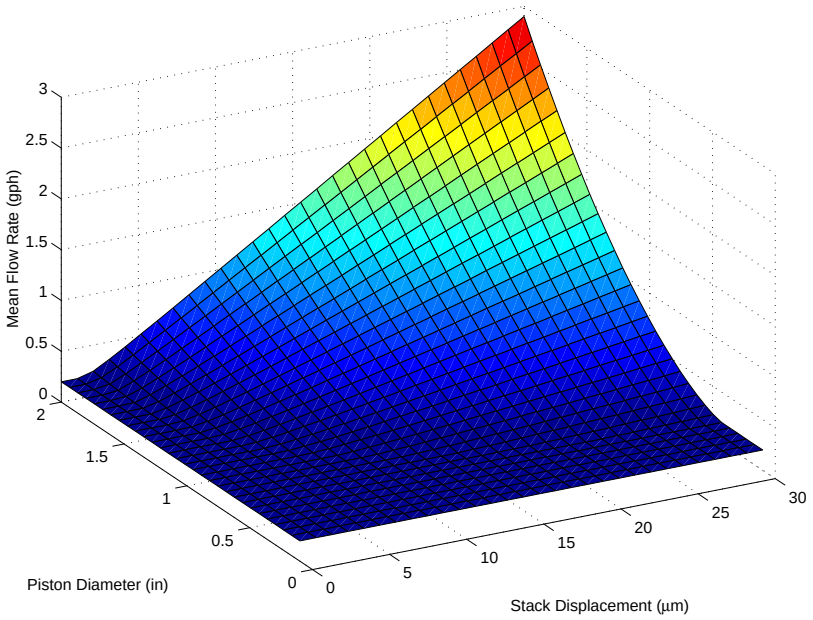

Figure 2.6: Quasi-steady mean flow rate versus piston diameter and actuator displacement at 50 Hz modulation and a 0.4 gph supply flow.

Table 2.4: Specifications of the PSt150/14/20 piezoelectric stack and LE150/200 amplifier.

Maximum Voltage (V)	**Max. Displacement (μm)**	**Blocked Force (lbf)**	**Coupled Bandwidth at Full Scale (Hz)**
150	20	1570	590

and i_{max} is the maximum current provided by the amplifier. The actuator chosen for this application has a capacitance of 7.2 μF and a voltage limit of 150 volts. With an amplifier with a current capability of 2 amps, the peak-to-peak displacement would only reduce to 16 microns at 700 Hz based on Equation 2.5, which is within the requirement in obtaining 40% modulation. Thus, a Piezomechanik LE150/200 amplifier was selected to drive the actuator. The coupled specifications of the actuator and amplifier are shown in Table 2.4, with a more exhaustive list shown in Appendix B.

The prime mover hardware was purchased from Bimba Inc., a manufacturer of hy-

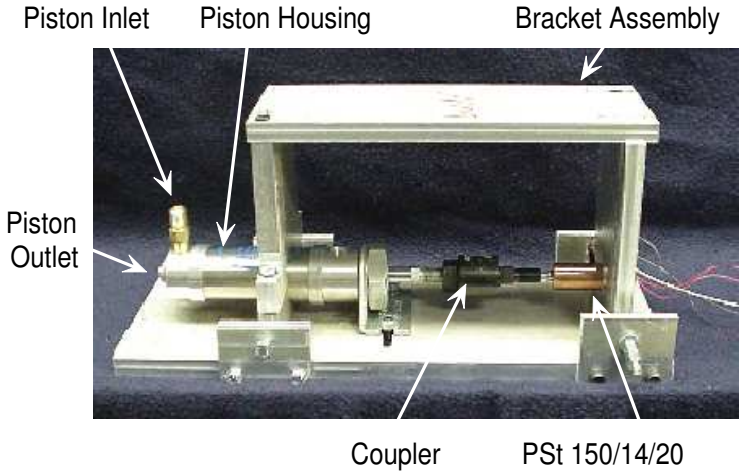

Figure 2.7: Photo of original assembled piston device.

draulic piston assemblies. The particular model chosen (H-172-DUZ) has a piston diameter of 1.5 inches, which increases the required area from the above calculations by a factor of 2.2. This alteration effectively reduces the required displacement to 7.3 microns, but doubles the force required to 1300 lbf, which still allows for operation within the stack's high-efficiency region. In order to be usable, a few modifications were made to the hardware components. The existing opening on the side of the piston chamber would be suitable as the inlet port, but a new hole was machined on axis with the piston to serve as the exit port. A coupling device with slop adjustment was altered with a threaded connection so that interface between piston and stack would be possible. The piping to and from the assembly would consist of 1/4-inch stainless steel Swagelock tubing, which would attach to the housing by means of brass NPT unions. The mounting brackets for the system were fabricated out of 3/8-inch thick aluminum, configured in such a way that the actuator would be joined with the piston housing on two sides in an effort to eliminate any flexibility. Figure 2.7 shows the completed piston actuator and prime mover assembly.

2.4.3 Check Valve Assembly Design

As stated at the outset, the check valve must be designed so that flow would completely stop when shut and that the flow resistance be negligible when open. Additionally, the valve must respond within a fraction of the modulation period. It was determined that a response time on the order of 5% of the period would be sufficient in order not to limit the fuel injector's performance. The pros and cons of both passive and active designs were explored for this application. A passive design would be a cheap, low maintenance option, but would suffer from the limitations due to the reliance on the fluid's force to shut the valve. The inertia of the valve mechanism would not permit this design to meet the rise time requirements, so focus was placed instead on an actuated check valve design.

For the same reasons as those for the piston design, a piezoelectric stack actuator was to be used to control this valve. Again, the limitations of this actuator call for design calculations to be made before selection of the prime mover hardware is made. To find the displacement, the quasi-static pressure drop across the valve is found at the fully-open and fully-closed positions. Of course, the valve being shut requires the displacement be equal to zero and thus the pressure drop be equal to the supply pressure. When the valve is open, the flow path through the valve is as shown in Figure 2.8. By applying the energy equation, the pressure gradient across the orifice can be related to the flow rate:

$$\begin{aligned} \triangle p &= p_p - p_o = \frac{\rho}{2}\left(v_o^2 - v_p^2\right) \\ &= \frac{\rho Q^2}{2C_d^2 A_o^2}\left(1 - \frac{C_d^2 A_o^2}{A_p^2}\right) \end{aligned} \tag{2.6}$$

where C_d is the discharge coefficient, A_p is the pipe area, and A_o is the orifice area of the valve fully open. We can assume that $A_o \ll A_p$, which simplifies computation of the orifice area, which is the perimeter P times the discharge thickness:

$$A_o = Px\cos(x) \tag{2.7}$$

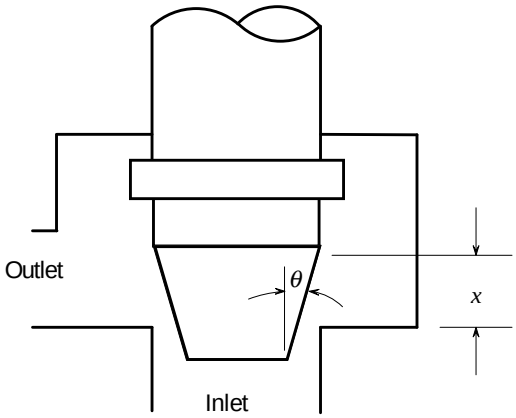

Figure 2.8: Schematic operation of the check valve.

By applying Equation 2.7 to 2.6, the following relationship is obtained:

$$x = \frac{Q}{C_d P \sin\theta} \left(\frac{\rho}{2\triangle p} \right)^{1/2} \tag{2.8}$$

Given the number of parameters involved with the displacement calculations, several candidate valves were chosen first, then down-selected based on calculations of their actuator requirements.

Ultimately, the valve chosen for this application was a Circle Seal 9400 solenoid-operated shutoff valve with a 1000-psi operating pressure. In accordance with the zero power requirement when ACC is off, this valve was configured to operate in a normally-open operation; i.e., the actuator must push down to close the valve. This particular model had a 0.156-inch stem diameter and a 2-degree trim angle, which, based on Equation 2.8, requires a displacement of at least 127 microns in order to obtain a pressure drop below 10 psi. This criterion would be achievable even with the displacement limitations of piezoelectric actuators.

A rough calculation on the rise time requirement of the valve revealed that the actuator must respond within 0.07 milliseconds, based on a 5% rise time on a 700 Hz period. There is an inherent difficulty in obtaining high displacements at high bandwidths with piezoelectric stacks, represented in the electrical impedance relationship (Equation 2.5). Most power

Table 2.5: Specifications of the PSt1000/10/150 piezoelectric stack and LE1000/100 amplifier.

Maximum Voltage (V)	**Max. Displacement (μm)**	**Blocked Force (lbf)**	**Coupled Bandwidth at Full Scale (Hz)**
1000	150	900	816

amplifiers are current limited and therefore limited in their achievable bandwidth as the voltage requirements, representative of the displacement, increases. It was decided to remain consistent with the displacement specification and relax the achievable bandwidth, so the Piezomechanik PSt1000/10/150 stack actuator and the LE1000/100 amplifier were selected to operate the valve. As shown in Table 2.5, the free displacement of the stack is 150 microns, but the bandwidth is limited to 816 Hz. To be specific, the rise time is approximately 0.25 milliseconds, which would provide a 5% rise time on a 200-Hz signal, still acceptable for the validation tests that would be performed. Given a 125-psi supply pressure, the stack would have to overcome about 2.4 lbf to close the valve. While this operates away from the stack's optimal efficiency region, it is a necessary provision to maintain the negligible pressure drop requirement.

Upon implementation, the solenoid was replaced with a coupling device that was designed to interface with the stack using a threaded union. Due to the fact that the valve closes some distance before the stem reaches the hard stop, this coupling device must have a provision in which it can be calibrated to maximize the actuator's effectiveness. Given that the threaded union has a resolution of about 320 microns per turn, the coupler could be turned slightly until the desired steady-flow condition is met. This would be accomplished by setting the stack to full displacement, then incrementing the coupler until the point at which flow stops is reached. The bracket assembly was not of great concern in this application due to the small forces expected of the actuator during operation of the valve. 1/4-inch thick support members were used to couple the actuator and the valve housing with access slots such that adjustment of the coupler would be possible. The completed setup is pictured in

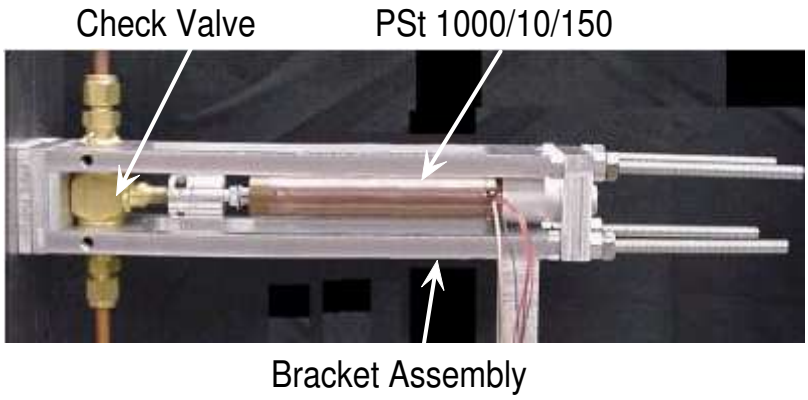

Figure 2.9: Photo of assembled check valve components.

Figure 2.9. An internal diagram of the piston/check valve fuel injector assembly is shown in Figure 2.10

2.4.4 Controller Design

As shown in Figure 1.5, the ACC system must make use of a reference signal from the combustion process and output an appropriate waveform of fuel into the combustor to compensate the instability. The simplest and most widely used sensing method is high-frequency measurement of the oscillatory pressure within the combustor, a method adopted in the present research. Linear phase shifters are commonly used in prototyping hardware designs because they allow for a more direct assessment of the authority of the fuel injection hardware. However, they require user intervention to adjust the gain and phase in real time, which has its limitations if the plant changes rapidly. This control strategy was used for the entirety of this work and was designed using SIMULINK software with the intent of compiling to a dSPACE DS1103 control prototyping computer. Once implemented, the fuel injector controller and hardware systems will fit into the ACC system as shown schematically in Figure 2.11 as atomization and combustion chamber processes, which are also known to affect the performance of ACC systems.

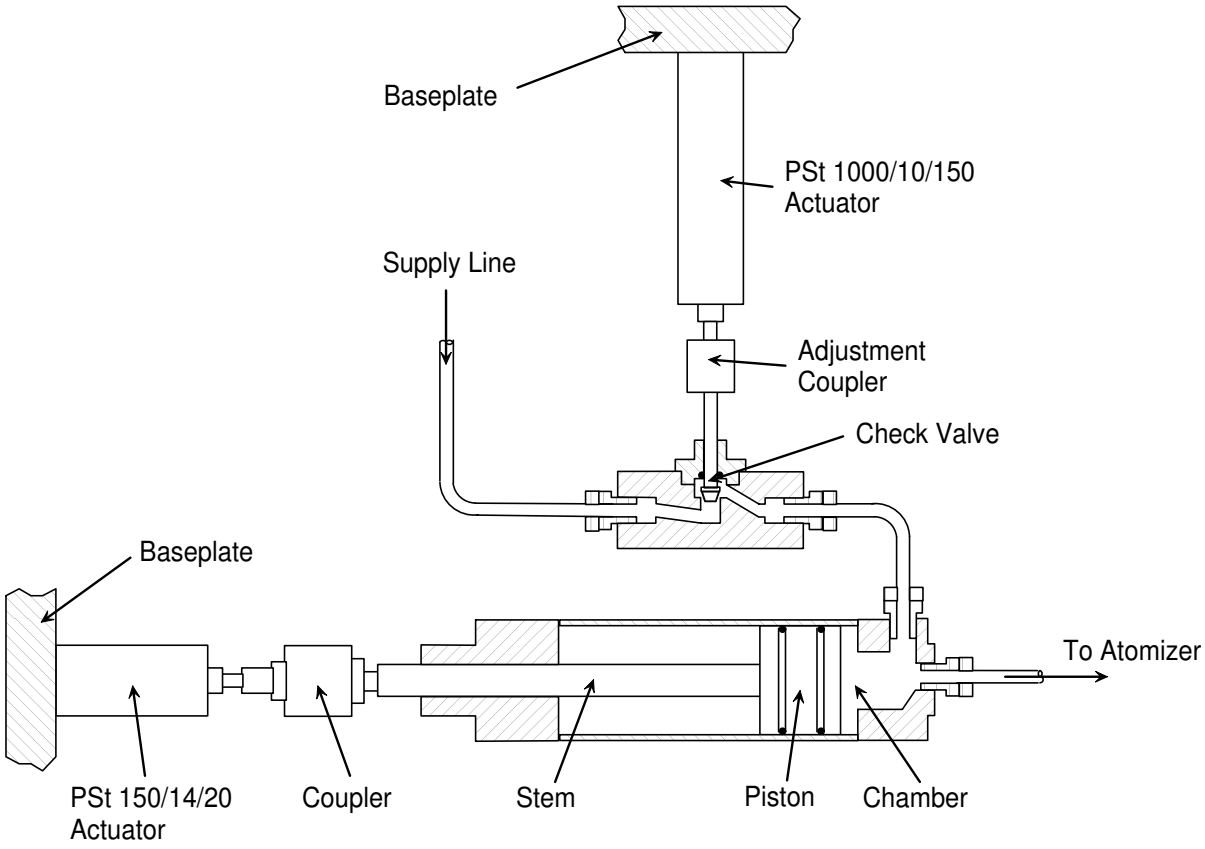

Figure 2.10: Cutaway diagram of assembled piston/check valve fuel injector.

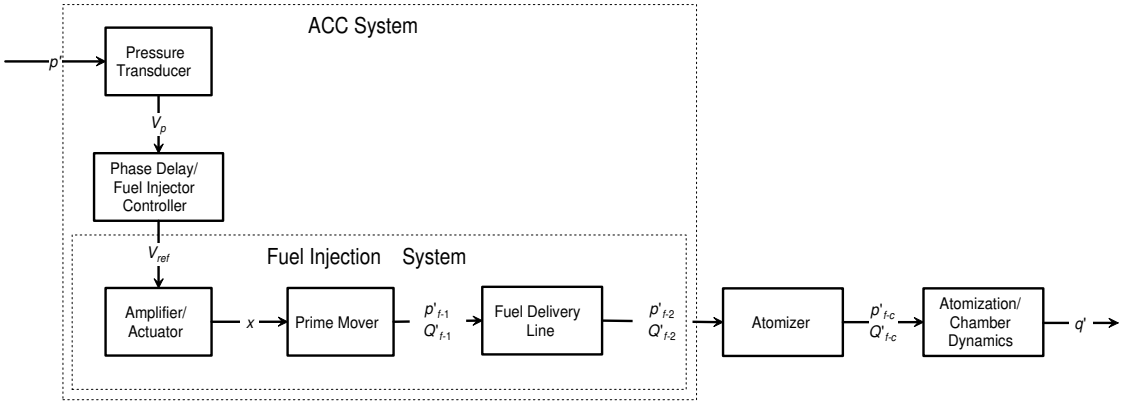

Figure 2.11: Open loop representation of the ACC system.

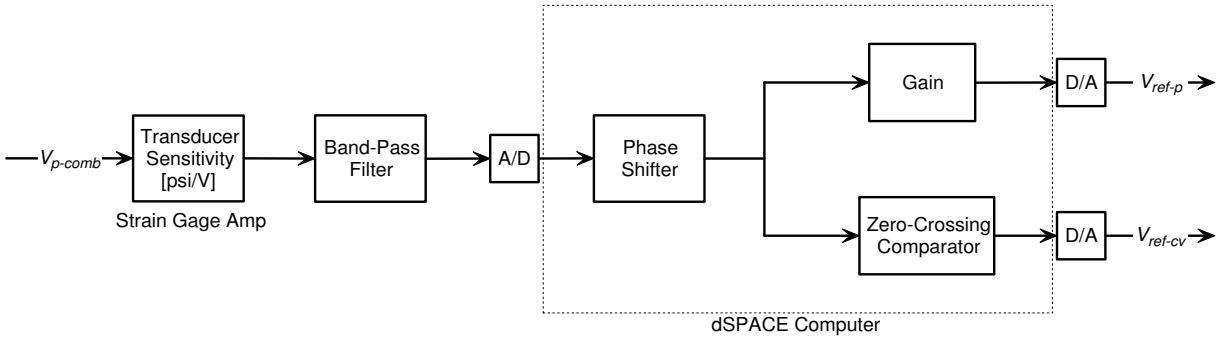

Figure 2.12: Control schematic for the piston and check valve.

From Figure 2.11, the phase delay and the fuel injector controller blocks were processed on the dSPACE computer. Before entering the A/D, the signal would be band-pass filtered to isolate only the limit cycle amplitude. The signal would then be phase shifted, which was achieved by implementing a time delay based on a user-defined input. Once shifted, the signal would be conditioned appropriately to drive the piston and check valve devices. Again, a user-defined input for the gain was used to scale the signal before driving the piston assembly. A comparator was used to trigger the check valve open and closed at times at which the slope of the piston displacement signal reached its maximum and minimum values, respectively. The control loop used to regulate the piston and check valve is shown in Figure 2.12.

2.5 Benchmark Testing of the Piston and Check Valve Assembly

Understanding the dynamics of each component and subassembly facilitates knowledge of the expected performance of the piston/check valve system. The piston actuator was first tested for bandwidth and linearity uncoupled and coupled with the prime mover hardware. Next the steady-state characteristics of the check valve were determined, followed by a simple

dynamic assessment of both the piston and check valve components in the presence of the liquid fuel.

2.5.1 Piston Actuator Tests

The actuation system chosen to drive the piston was tested for dynamic capability by first generating frequency response functions (FRFs) of the amplifier's dynamics, followed by free displacement tests of the actuator. The effect of the added prime mover hardware was then determined by performing the same diagnostics of the actuator coupled with the piston device.

In generating FRFs of the LE150/200 amplifier, the stack was replaced with a capacitor with identical specifications to the open-circuit capacitance of the PSt150/14/20 actuator. This measure was implemented so that variations in the stack's capacitance with voltage and self-heating did not compromise the experiment. By applying a sine sweep signal to the stack, an FRF was generated of the amplifier's voltage output versus reference signal, with data collection performed with a Hewlett Packard FFT analyzer. The amplifier output was easily determined using the monitor output channel, which scales the output voltage by a factor of 1/100, thereby easing data acquisition. Figure 2.13 shows the frequency response of the amplifier with varying signal amplitudes. As expected, an amplification of 30 results at low frequencies. As the frequencies increases, however, a first-order roll-off occurs, whose break frequency is dependent on Equation 2.5. At full-scale amplitude, the break frequency is approximately 800 Hz, about 200 Hz greater than that predicted from Equation 2.5. The error between the theoretical and experimental values is most likely due to a small error in the reference capacitance value. Nonetheless, the measured data may still be useful as an approximation of the expected bandwidth.

The dynamics of the stack were evaluated next over the same range of frequencies as with the amplifier. Measurement of the free displacement was accomplished by using a

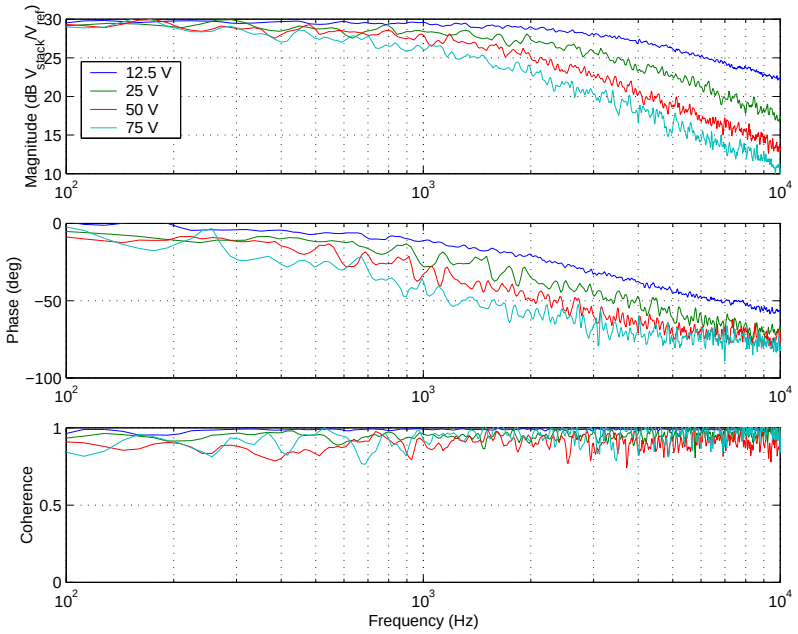

Figure 2.13: FRFs of LE150/200 amplifier output to the input signal at various amplitudes.

laser vibrometer to measure the free end of the stack with the other end fixed in a vibration isolation bracket. The FRF was generated using the vibrometer signal as the output and the amplifier monitor signal as the reference. The resulting FRFs revealed that the stack's response is insensitive to the excitation amplitude, with one case shown in Figure 2.14. Throughout the zero to 700-Hz bandwidth, the expected sensitivity of -17.5 dB was maintained, which indicates that the amplifier will exclusively govern the dynamics. The measured full-scale displacement amplitude of 20.6 microns was very close to the 20 microns reported by the manufacturer. It should be noted that the unloaded resonance is at 7 kHz, which is not expected to be of concern even with the added mass of the prime mover assembly.

The stack was also tested for linearity by observing its hysteresis effects at a certain frequency. Using a 1-Hz sine wave input, the hysteresis curve shown in Figure 2.15 was generated, showing a slight nonlinearity in the stack's output, which is expected for piezoelectric materials because their physical parameters change a small amount with voltage.

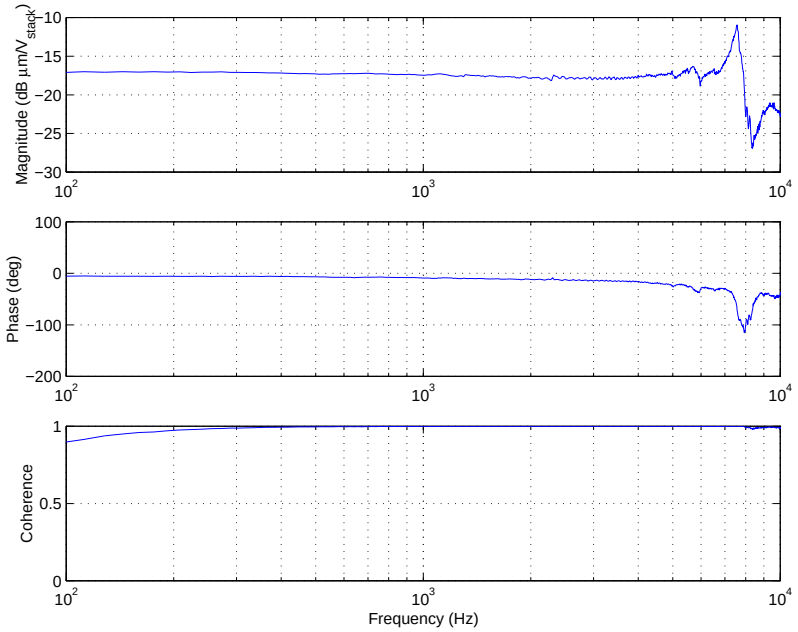

Figure 2.14: FRFs of the PSt150/14/20 actuator displacement to the amplifier output.

This nonlinear behavior was not a concern for the present piston design aside from the fact that this would encourage some self-heating to be generated within the stack.

2.5.2 Steady-Flow Check Valve Experiments

The check valve hardware was next tested in static operation to determine if the actual flow characteristics were as expected. Based on the findings with the piston actuator, the bandwidth of the check valve actuator was not a cause for concern because it was not likely to be any less than the theoretical value determined from Equation 2.5.

The goal of this testing was to determine if a 150-micron displacement would be sufficient to drive the valve. To achieve this, an empirically determined flow coefficient was found, accomplished by measuring the pressure gradient and flow at various known valve displacements. In essence, this was performed by simply measuring the pressure drop across the check valve with a 0.4 atomizer and a 125-psi supply pressure, the exact conditions to

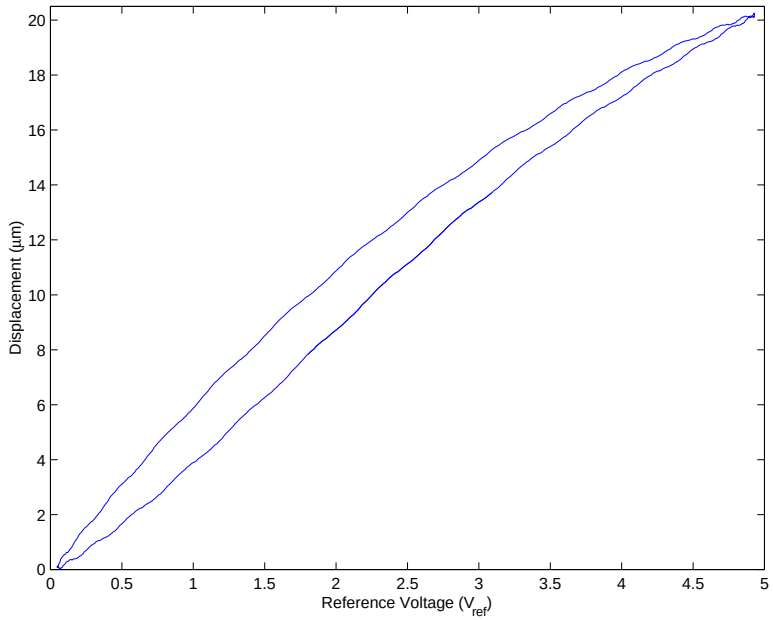

Figure 2.15: Hysteresis plot of the PSt150/14/20 actuator at 1 Hz.

be run in the combustor experiments. The resulting data taken of the pressure gradient versus stack displacement is shown in Figure 2.16, along with the theoretical estimate from Equation 2.8. The data in the figure was obtained after careful calibration of the check valve coupler was performed in accordance with the procedure outlined Section 2.4.3. When the stack's voltage was brought to zero, a 5-psi pressure drop resulted, which is quite close to that predicted in the theoretical estimate. The conclusion to be made is that the 150-micron stack is indeed suitable for operation of the check valve.

2.5.3 Preliminary Dynamic Flow Experiments

The objective of this line of testing was to determine the fuel injection system's performance at a single operating frequency. The piston system was tested in a kerosene test bed, fitted with a 0.4 atomizer. The existing gear pump was used to pressurize the liquid and a relief valve was used to regulate the pressure. A length of tubing of about three feet was installed

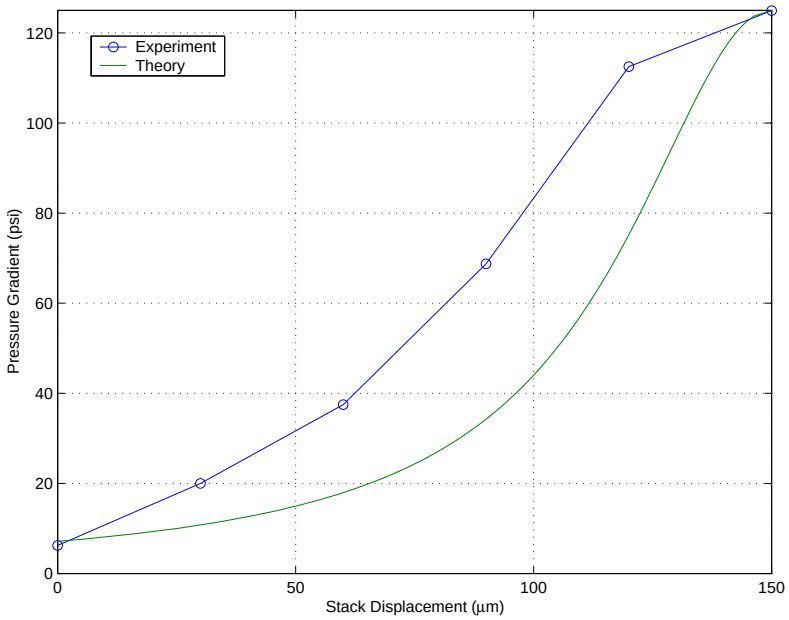

Figure 2.16: Check valve pressure drop versus stack displacement.

between the piston exit and the atomizer to simulate the actual length at the entrance to the combustor. An Entran EPX-V01 pressure transducer was placed in the fuel line immediately upstream of the atomizer to measure the dynamic response on the pressure. The dSPACE phase shifting controller was run with a 100-Hz reference signal scaled to produce 20 microns peak-to-peak displacement, a theoretical 100% modulation. The upstream pressure was set to 125 psi to provide a 0.4-gph mean flow rate. In calculating the percent modulation on the flow, it was assumed that the fluctuating pressure at the transducer location was equal to that inside the atomizer and that Equation 2.1 holds true.

The result of this testing was that only a 4% modulation on the flow was achieved, well below the expected 100% modulation. The cause of this discrepancy was investigated, including determining the possibility of seal deflection, tube swelling, and air compressibility. In order to determine the dynamic nature of this dissipation, a step signal was input to the check valve in order to command its instantaneous closure. The pressure and flow rate were qualitatively observed over time, and it was found that there was an apparent first-order

decay in the pressure and flow over the course of three seconds. After running the system under mean flow over time, the test was performed again. It was now observed that the decay time had shortened to nearly 1 second. It was therefore determined that the modulation authority was compromised by the capacitive nature of an air volume within the fluid. For the present design effort, it was necessary to find and implement solutions to the problem, then to assess the results.

One solution to the problem was to attempt to bleed the system by orienting the piston assembly vertically and ensuring there were no local high-points within the fuel system components in which air may collect. At the exit of the piston assembly, the piping reached a high point, in which a ball valve was installed so that air that collected in this location could be purged easily by opening the valve. A further measure was to swap the 150-micron stack from the check valve to the piston assembly in order to increase its free displacement potential by a factor of 7.5. Under loaded conditions, it was recognized that the actual displacement would be force limited, but it was hoped that the authority would be an improvement over that provided by the 20-micron stack. In swapping the check valve, the line pressure was increased to 165 psi to obtain a pressure drop of 40 psi at the check valve in the fully open position. With reference to Figure 2.16, this would increase the sensitivity of the check valve's pressure drop to stack displacement such that the downstream peak-to-peak pressure would be about 35 psi based on steady-state assumptions.

When testing was again performed on this system at a theoretical 100% modulation and 0.4 gph, the time trace shown in Figure 2.17 was achieved for both the piston with check valve in operation (blue line). While still not the expected 100% modulation, the authority was now at nearly 22% modulation, an improvement of about 5 times that achieved in the previous setup. The modulation of the check valve alone is shown as well in the figure (green line) to assess the extent of the bleeding improvements. Without the air compressibility, the check valve should have modulated with an amplitude of nearly 18 psi, however, however, an amplitude of 2 psi resulted. Based on this result, it was apparent that that bleeding provisions still did not significantly reduce the air volume within the system.

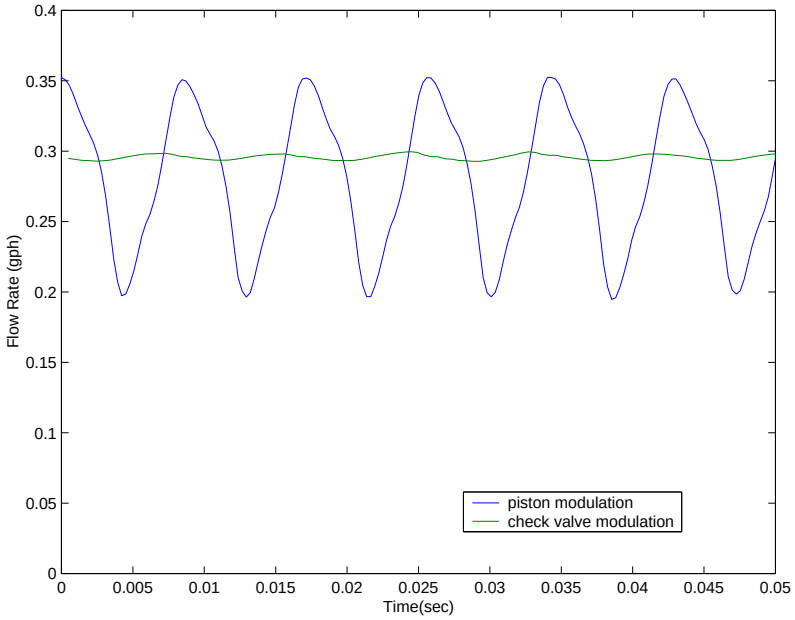

Figure 2.17: Modulation of piston/check valve (blue) and check valve only (green), determined with pressure measurement.

At this point, other causes for low stiffness effects were identified, with the most likely being bracket deflection. If this is the case, it is fairly obvious that the small displacements provided by the stack would be seriously compromised. Another possibility was viscoelastic seal deflection, which may occur at the various O-rings within the piston and check valve components. It should be noted that it is unlikely that these effects would be totally mitigated by imparting additional preventative measures, especially in light of the attempts made so far. Moreover, with the present level of understanding, it is not possible to determine the nature of the achievable modulation in the presence of these effects. Thus, it is necessary to model the effects in a dynamic sense so that future fuel injector designs may optimize the prime mover hardware specifications in order to produce the desired modulation. These efforts are explored further in the acoustic modeling of the piston/check valve device in Chapter 3.

2.6 Secondary-Line Throttle Valve Development

The throttle valve fuel injector was designed next in accordance with the specifications outlined in Table 2.2. The major differences between the present design and the piston/check valve designs were that the nominal mean flow rate would be 4 gph and an atomizer size of 4.0 would be used. As described in Section 2.3, throttle valve designs may be installed as either primary or secondary line arrangements, which are marked by varying degrees of complexity in the hardware setup. In this work, the valve will be incorporated into a secondary system, but will not make use of a fast-response primary line regulator to maintain a constant mean flow rate when ACC is on. Instead, the valve will maintain its mean flow, adding with the primary line regardless of whether ACC is on or off. This will allow the throttle valve prototype to be as simple as possible to prove the concept of this fuel injection method.

Because modulation takes place by energy dissipation, concerns about losing the energy provided by the secondary pump have prompted methods for conserving this energy. Depending on the pump's flow output, it is likely that most of the flow would be diverted back to the fuel tank, thereby compromising the overall efficiency. One solution found to reconcile this was to add an accumulator upstream of the valve, which would serve as a fluidic capacitance and continually fill and discharge during normal operation of the valve. By storing the unused energy, the accumulator can maintain the supply pressure and allow the to be turned off periodically. This would necessitate a logic circuit to control the pump cycle to maintain a predetermined pressure range. In the following sections, the design and selection of several components will be discussed, such as the secondary fuel pump, the accumulator, and the throttle valve device. The schematic shown in Figure 2.18 shows how the secondary fuel injection system components tie in with the existing primary line hardware. Pump #1 refers to the existing gear pump on the combustor rig. Fine control of the pressure and flow is achieved by the flow regulators, pressure regulators, and metering valves in the two systems. Also note that pressure measurements were taken at locations upstream and downstream of both fuel injector devices.

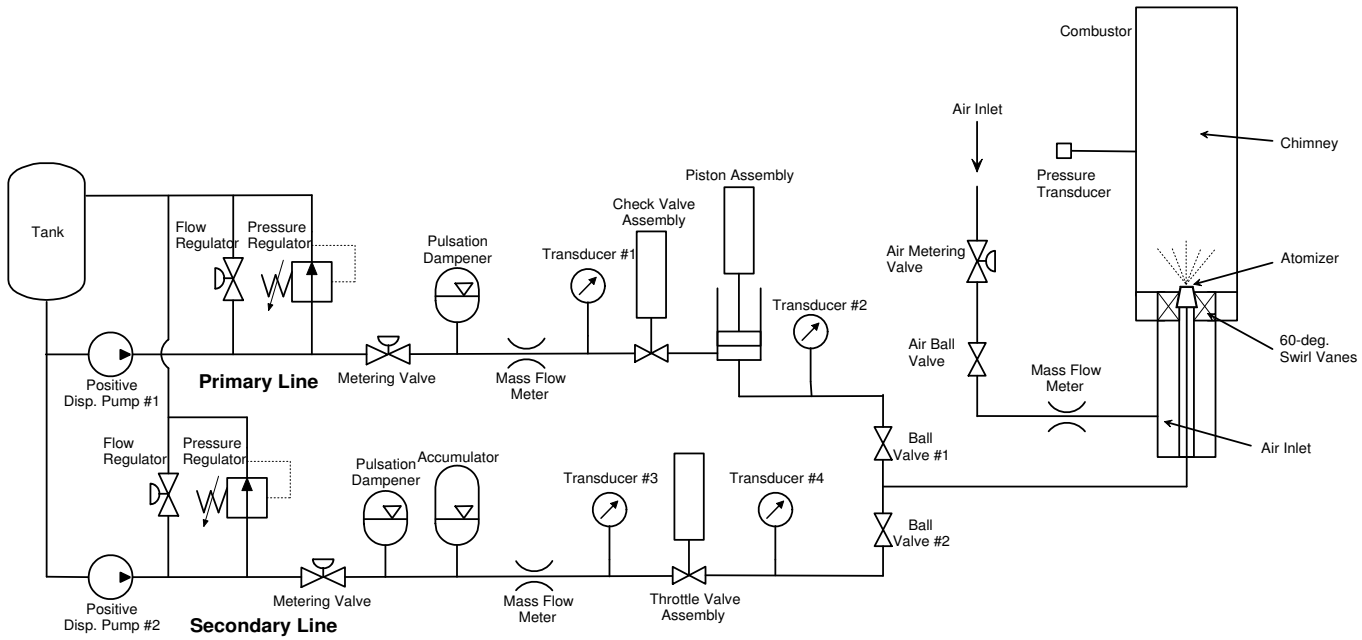

Figure 2.18: Schematic of secondary fuel line components relative to the existing primary line.

2.6.1 Supply-Side Component Design

The first component to be chosen for this design was a fuel pump, whose exact requirements were determined based on the desired flow profile of Figure 2.2. If the ACC system is expected to provide 40% modulation, the trough of the flow profile Q_{min} must be equal to 2.4 gph, with a pressure of 45 psi. At this time, the secondary line should output zero flow, so the entirety of the flow must come from the primary line. When the throttle valve output reaches its peak, the combined flow rates Q_{max} must be equal to 5.6 gph, resulting in a downstream pressure of 245 psi. To satisfy this requirement, the secondary line must be able to provide at least 3.2 gph at 245 psi.

Most pumps have the ability to provide flow rates on the order of several gallons per minute, so difficulties arose in finding one that provided appropriate pressures and applicability to the working fluid. Positive displacement pumps are generally favorable in any

application where a high power density is required; that is, high flow rates at high pressures. Gear pumps are positive displacement pumps that provide the lowest amount of system noise, but are very expensive when non-lubricating liquids, such as kerosene, need to be pumped to high pressures. Piston pumps are typically less expensive and have the ability to pump to pressures greater than 500 psi. These pumps generally produce strong 30 Hz harmonics in the fuel line, which have the possibility of detracting from the authority of the ACC system. The fuel line must therefore have provisions to dissipate the incoming pulses in order to eliminate the pump noise. One provision was to install a pulsation dampener in the line, which uses compressed gas to attenuate the lower-frequency harmonics due to the low stiffness of the gas.

A Hydra-Cell Inc. F20-G piston pump was chosen because of its pressure and flow characteristics. With a 1450-rpm motor, its rated maximum flow rate is 13 gph and maximum pressure is 1500 psi, which satisfy the requirements. Based on the pump characteristic in Figure 2.19, the flow degrades only slightly over the range of operation. A high operating pressure is favorable because, if more modulation were required, one would simply increase the supply pressure instead of increasing the actuator output.

Part of the supply system would consist of an accumulator that would store the unused pump energy. This accumulator must be capable of storing a large enough volume so that the pump cycle would be kept to over a minute under normal operation of the throttle valve. To control the pump, an analog comparator circuit would be set to predetermined high and low pressure limits and use a low-pass-filtered pressure transducer signal upstream of the throttle valve to provide the reference signal. With the mean pressure set to throughput 4 gph, the secondary line would be required to throughput a 1.6 gph mean at 40% modulation. This would require the accumulator to be at least 0.0267 gallons, or about 6.2 in^3 for a 1-minute cycle to occur. The accumulator selected for use was a 30 in^3 bladder accumulator with model number AM3031003 from Accumulators Inc. On a steady-flow basis, the drain time for this accumulator would be well over 4 minutes.

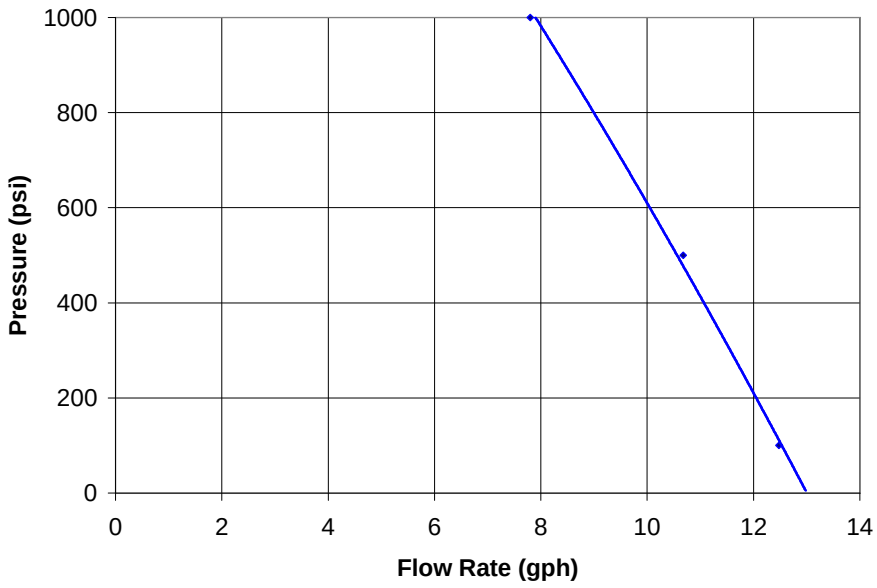

Figure 2.19: Pump curve for the HydraCell F20-G piston pump.

2.6.2 Valve Analysis and Design

The throttle valve design was approached in the same way as the piston/check valve development in that quasi-static, incompressible assumptions would be used to calculate the specifications for each subassembly. It was decided to minimize the cost of constructing the new ACC system by designing the hardware to incorporate the existing PSt1000/10/150 actuator to drive the valve. Because the dynamic forces on the valve were not expected to be very large, the dimensions of the stem could be chosen such that the discharge area achieved by displacing the stack can be maximized. Thus, a globe valve configuration was the most logical choice because this discharge area is dependent on the stem's perimeter, as shown in Equation 2.7.

The flow rate through the valve is dependent on the supply pressure and the combined resistance of the valve and the atomizer in series. The flow coefficient C_v through a globe valve as a function of discharge area is obtained from an empirical relationship from Lyons

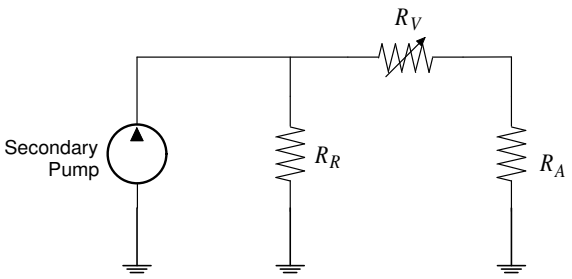

Figure 2.20: Resistance network for quasi-steady flow model.

[29]:

$$C_v = 5.89 \times 10^4 A_o \left[1.3 + 0.2\left(\frac{A_p}{A_o}\right)^2\right]^{-1/2} \qquad \left[\text{gph}/\sqrt{\text{psi}}\right] \tag{2.9}$$

where A_p is the valve face area and A_o is the discharge orifice area. The flow coefficient can then be converted to a fluidic resistance by applying the following relationship:

$$R \equiv \frac{\triangle p}{Q^2} = \frac{3600}{C_v^2} \qquad \left[\text{psi}/\text{gph}^2\right] \tag{2.10}$$

Based on the components that were specified for this throttle valve design, a simulation was performed to determine the idealized flow modulation of the system. For simplicity, it was decided to model the system without the addition of the primary line. In the simulation, the valve would not completely shut at the trough of the waveform as stated before, but output Q_{min}. The model was formed by first identifying the resistances of the pressure regulator, throttle valve, and atomizer in the fluidic circuit shown schematically in Figure 2.20. In the figure, R_R designates the resistance of the pressure regulator, R_V is the variable resistance created by the throttle valve given by Equation 2.9 and 2.10, and R_A is the atomizer resistance. The pump was modeled as a variable flow source with the characteristic shown in Figure 2.19. Expressions for continuity and conservation of momentum were then solved to find the upstream and atomizer pressures.

With a stem diameter of 1 inch, a plot of these pressures versus actuator displacement at a 500-psi supply pressure and a 4.0 atomizer is shown in Figure 2.21. Based on this plot, in

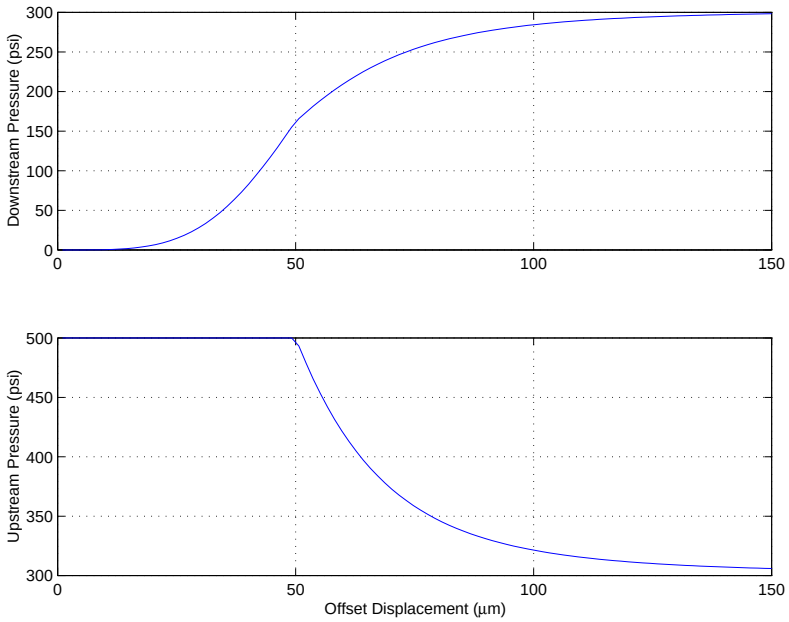

Figure 2.21: Results of simulation at 500 psi upstream pressure and a 4.0 atomizer.

order to modulate 40% about 4 gph, the required peak-to-peak displacement is 34 microns. The fact that the upstream pressure begins to drop off at a displacement of 50 microns is indicative of the flow limitation due to losses to the pressure regulator. However, it is likely that this effect will not happen at high frequencies due to the inertia of the pressure regulator mechanism, so these results give a conservative estimate of the required displacement.

Most piezoelectric stacks are manufactured with a pre-stress casing, which allows for a safety measure for the stack if it should be placed under excessive tensile loads. Because the PSt1000/10/150 actuator may only provide 100 pounds of force under tension, it is desired to orient the stack such that it may only experience compressive forces. Thus the inlet side of the valve, always at a higher pressure than the outlet, should be facing towards the side of the stem that would compress the stack. The stack would push against the pressure gradient during positive motion and be assisted by the gradient with restorative motion. Based on the maximum expected pressure gradient of 455 psi, the stack must overcome 357 lbf when opening the valve, which is within the operating limits of most stack actuators. One

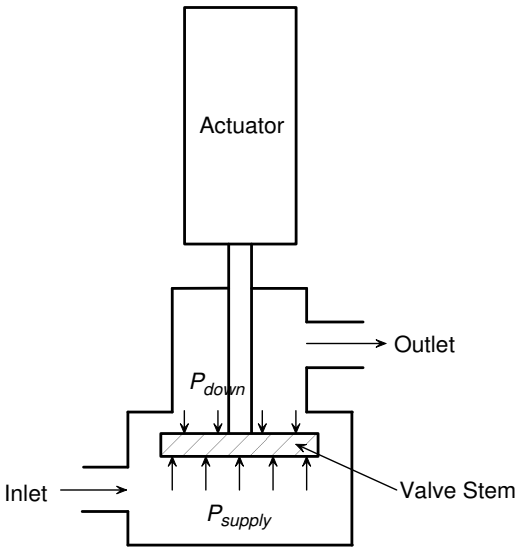

Figure 2.22: Conceptual diagram of throttle valve subassembly.

further requirement was that the valve should be shut when the actuator power is zero. This necessitates a normally-closed, or push-to-open, valve configuration as a further requirement of the design. As a combined result of all the considerations mentioned above, the throttle valve must be configured as shown in Figure 2.22.

Other specifications of the valve are that the body must be able to withstand at least the maximum operating pressure of 500 psi, but here we impose that it withstand up to 1000 psi as a factor of safety. Also, the seals and seats must be made of a material that will not deflect when shut, such as hard plastic or stainless steel. This will eliminate uncertainties in the performance and maximize the available displacement provided by the stack because there will be no viscoelastic seat deflection. The final requirement is that there must be a way to orient the valve such that both the inlet and outlet chambers may be bled easily.

After an exhaustive search though many off-the-shelf valves available in catalogs, it was decided that the most feasible option was to fabricate the valve in-house. In so doing, the valve materials could be selected, a normally-closed operation could be implemented, and a bleeding mechanism could be installed. One problem with customizing a valve is that

Table 2.6: Specifications for the valve stem and seat.

Specification	Unit
Material	Nickel Alloy
Stem Outer Diameter	1.203 in
Seat Inner Diameter	1.087 in
Stem Face Angle	45°
Spring Constant	235 lbf/in

there are limits on the precision to which one can machine a hard-material valve seat and face such that it would seal when shut. To resolve this, a pre-fabricated valve seat and stem were used for this design. Automotive fuel-injection valve stems are well suited for high-pressure operation with a gasoline working fluid and are readily available at low cost. The valve chosen had a stem diameter of 1.203 inches and was made from a nickel alloy. In order to accommodate the valve stem design, the valve body was constructed from aluminum as shown in Figure 2.23. Flow would enter the supply chamber of the valve through an inlet port at the bottom of the valve body. In order to relieve the air trapped in the upstream portion of the system, the valve body had a bleed port incorporated towards the top of the chamber, in which a ball valve would be installed. To minimize the possibility of air being trapped in the outlet chamber, the outlet port would be oriented on the upper part of the valve body, so that the air would likely be flushed out of that chamber. The stem was modified such that a threaded rod tack welded to the stem would join with the stack's tapped end. An added feature of automotive valve is that it has a return spring attachment because the valves are solenoid actuated. This return spring would be beneficial for the present application in further reducing the possibility loading the stack in tension as well as ensuring that the stem is seated with a pre-stress force. The stem spring was pre-loaded such that it would exert 60 lbf on the stem when the valve is shut. Several of the specifications for this valve stem assembly are given in Table 2.6. It should be noted that a VACCG reference due in late 2003 by Schiller will outline more specifics of this valve design.

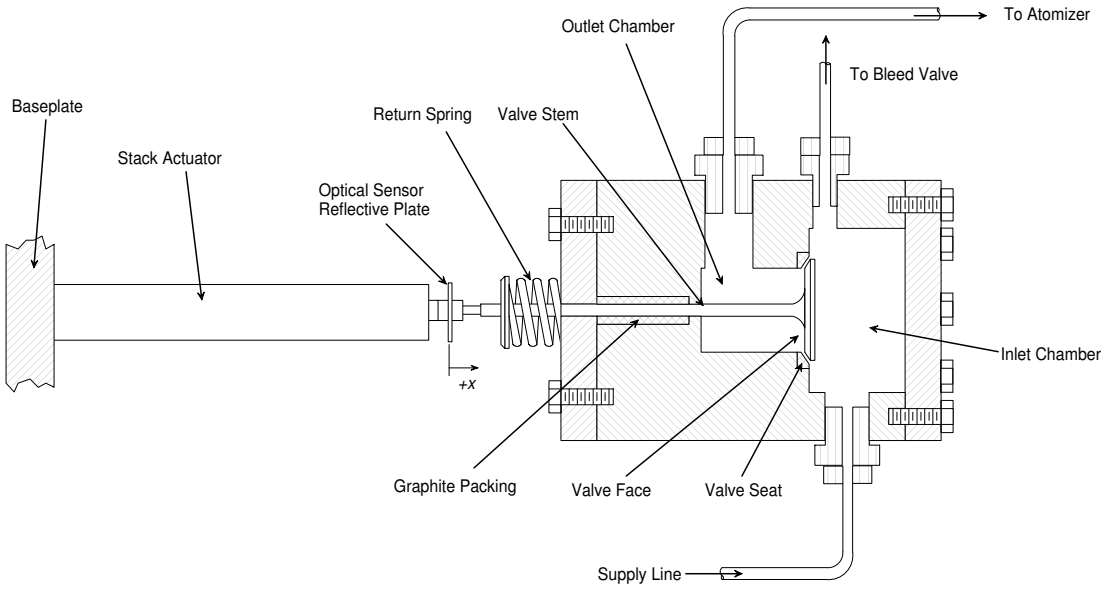

Figure 2.23: Cutaway diagram of assembled throttle valve fuel injector.

2.6.3 Piezoelectric Stack Replacement and Bracket Design

Failure of the PSt1000/10/150 actuator prompted selection of a new stack and amplifier combination to drive the valve. The new stack would be of a higher displacement rating than the previous one because of uncertainty in the actual authority due to losses such as those existent in the check valve as described in Section 2.5.3. Due to inherent current limitations of driving amplifiers, the bandwidth of the new actuator was not expected to meet the 700 Hz requirement stated earlier. Suspending this criterion for the time being is helpful in meeting one of the main objectives of this research: minimizing the actuator size required to produce certain percent modulation, which may require high displacement amplitudes to perform initial validation experiments before optimizing the system. As long as the bandwidth allows for most of the actuation to occur at the 100-Hz limit cycle frequency of the VACCG combustor, the present actuator would be satisfactory. It will be left to future research to optimally select an actuator size that will suit specific requirements.

The actuation system selected was a 500-micron displacement stack capable of pro-

Table 2.7: Specifications for the Pst1000/16/500 actuator and the LE1000/100 amplifier.

Maximum Voltage (V)	**Max. Displacement (μm)**	**Blocked Force (lbf)**	**Coupled Bandwidth at Full Scale (Hz)**
1000	500	2700	150

viding 2700 lbf of blocked force, with model number PSt1000/16/500 from Piezomechanik. For this application, an amplifier with model number LE1000/100 was chosen to provide a maximum output of 1000 volts and 1 amp to the stack. The free dynamics of the stack are likely to change significantly with the addition of the valve stem, so it becomes necessary to compute a new resonant frequency. Based on the 17-N/μm stiffness estimate provided by the manufacturer, the resonance would move to 1.26 kHz with the additional stem mass, which is still well above the amplifier's expected corner frequency of 150 Hz. Table 2.7 shows a list of several key specifications of the actuator/amplifier combination, with a more extensive list contained in Appendix B.

To address the concern of the possibility of bracket deflection in the piston/check valve device, the present bracket structure was designed to be quite rigid. The bracket assembly supported the stack to the valve housing on three sides: on two sides by 3/8-inch thick aluminum members and a 5/8-inch member on the third. The stack's base-plate was made from one-inch aluminum, with a fine-threaded nut to adjust the valve's null position. The completed valve housing and brackets for the throttle valve subassembly is shown in Figure 2.24 as configured for initial fuel injection validation experiments.

The controller for the throttle valve was identical to the phase shifter used in modulating the piston from Section 2.4.4. The only dissimilarity was in the bias voltage input to the stack. The mean voltage is expected to correspond to a certain flow rate, and it will not be until accurate information of the flow coefficient that voltage may be precisely correlated to flow rate. Thus, the addition to the existing SIMULINK code was a user-defined input for this bias voltage to the stack. The output voltage was saturated at zero and 5 volts to prevent driving the amplifier past its limits.

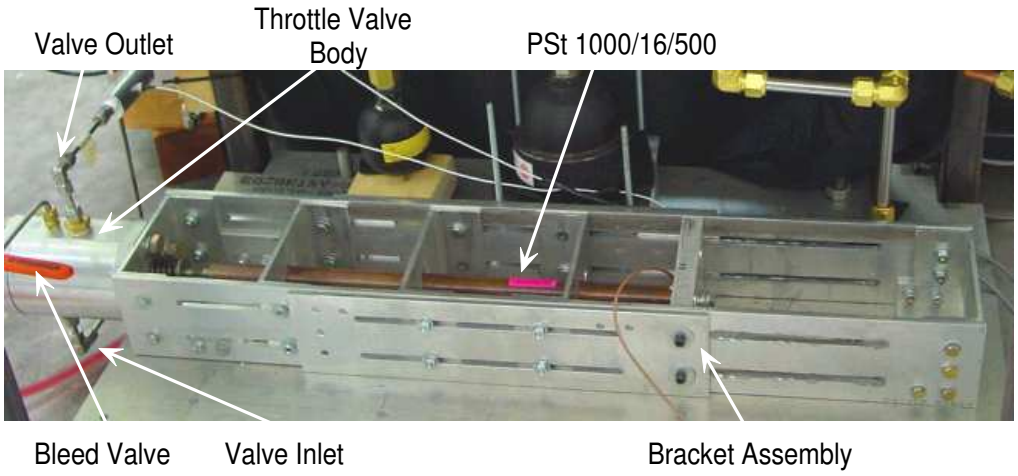

Figure 2.24: Photo of completed throttle valve and actuator bracket assemblies.

2.7 Benchmark Testing of the Throttle Valve Assembly

Validation testing of the throttle valve device requires that the ACC system hardware and control strategies be as simple as possible. After the initial validation is complete, higher degrees of complexity to practically realize the system may be then experimented upon. Thus, the system will be first tested in a primary line arrangement despite the intended design and it will be left to future research efforts to validate the secondary-line modulation authority. Indeed the simulation results from Figure 2.21 show that the current hardware in a primary-line setup will provide 40% modulation, therefore no alterations would need to be made to the present design.

The purpose of performing the initial set of dynamic experiments was to determine the frequency response of each subsystem de-coupled from the fluid. After this was gained, several experiments were performed with the fluid present to gain insight on the actual characteristics of the valve. As a result of this testing, several non-ideal effects were found to dominate the valve's operation over all frequencies, prompting several corrective measures

to be put into place.

2.7.1 Valve Actuator Tests

The frequency capabilities of the PSt1000/16/500 actuator were evaluated by gathering FRFs of the displacement at varying amplitudes of excitation. The resulting responses of the laser vibrometer output to the input signal are shown in Figure 2.25. Based on these FRFs, empirically determined break frequencies based on 45-degree phase crossings were plotted in Figure 2.26 in red, along with a curve fit extrapolated to 1000 Hz. Over an extended period of operation at frequencies close to the break frequencies, the amplifier has an increased tendency to trip the interlock breaking circuit. This is due to the fact that the amplifier has a current boosting stage that allows for higher currents to exist for a short period of time, which becomes depleted within a matter of seconds. Operating the stack near these frequencies has been shown to increase the thermal loading of the stack, which reduces its lifetime significantly, and therefore should be avoided if possible. The dashed blue line in Figure 2.26 is an extrapolated curve of the points in which the interlock condition was encountered during fixed sine dwell tests. Note that, at full amplitude, this reduces the operating range to below 80 Hz, an apparent detriment to the intended use of piezoelectric actuation for bandwidth capability. Most of this unused displacement will be used to achieve a mean valve position.

To test the nonlinear character of the valve's displacement, its hysteresis was evaluated. The stack was now attached to the valve stem, as shown in Figure 2.24, and its displacement measured again using the laser vibrometer. Figure 2.27 was generated with a 1-Hz full-scale input while measuring the vibrometer output. The plot reveals a nonlinear loop at the peaks of the sine wave, most likely a result of high static friction that the valve stem must overcome when the velocities become small. Another interesting point is that the peak-to-peak range of motion is decreased by about 3 dB to nearly 370 microns, and contains a small phase lag as evidenced by the larger loop. It should be noted that applying a DC

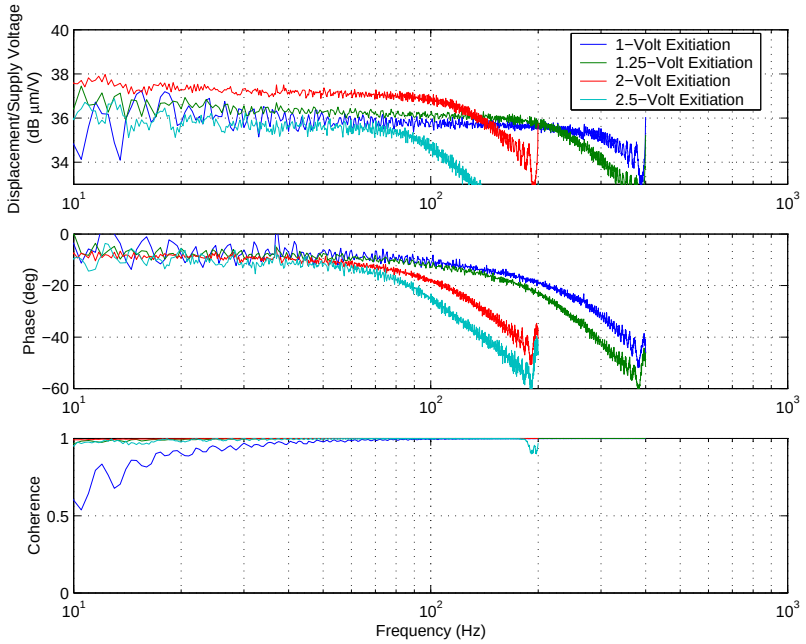

Figure 2.25: FRFs of the PSt1000/16/500 actuator displacement output to the LE1000/100 amplifier input at various amplitudes.

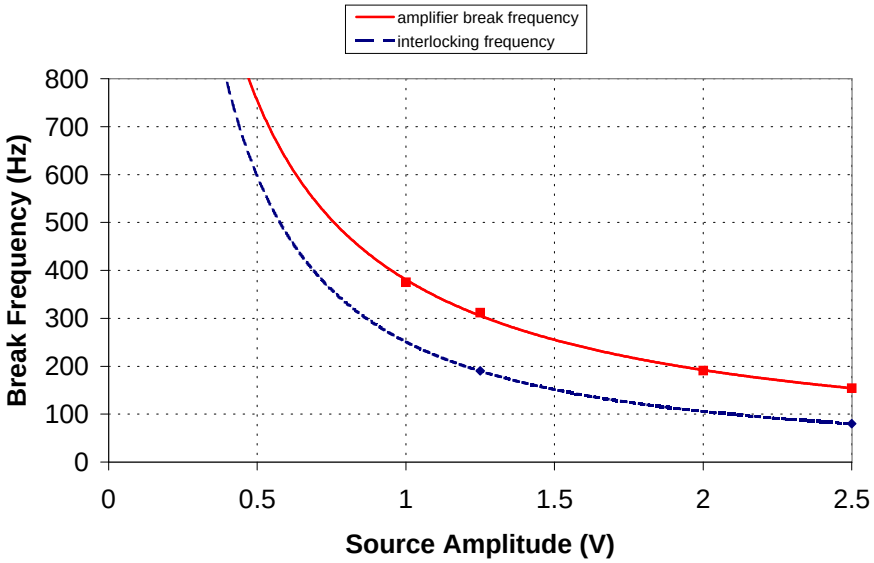

Figure 2.26: Operating limits of the PSt1000/16/500 actuator showing the amplifier corner frequencies and interlocking condition.

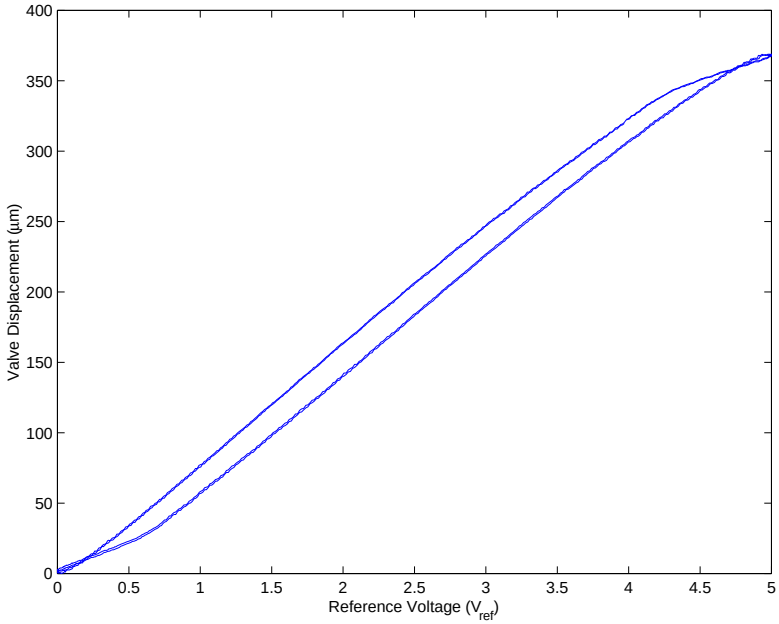

Figure 2.27: Hysteresis curve of the PSt1000/16/500 actuator coupled with the valve assembly at 1 Hz.

voltage to the stack provided a free displacement of only 453 microns. This decreased motion is not of concern because only a 34-micron amplitude is needed to produce 40% modulation.

2.7.2 Fluid-Loaded Experiments

The throttle valve was installed in the fluid system according to the schematic in Figure 2.18, with ball valve #1 closed to test the valve in a primary configuration. The stack was first energized with a DC bias in order to allow the valve to throughput a mean flow rate. When this was attempted, it quickly became apparent that its performance was governed by unexpected dynamics. When the stack was commanded to this DC voltage, the downstream pressure and flow rate responded with an apparent first-order time decay, followed by a much slower and unpredictable transient, as illustrated in the time trace in Figure 2.28. In the

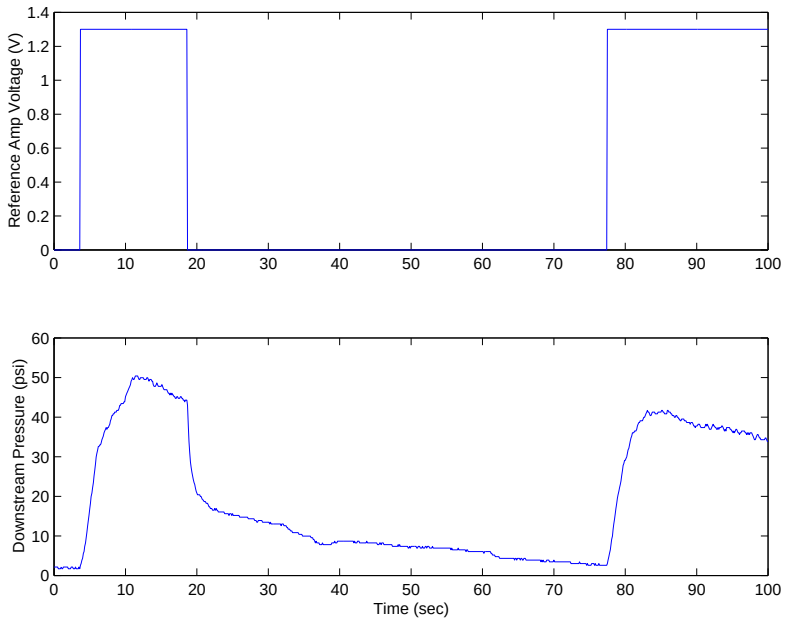

Figure 2.28: Transient pressure behavior given low voltage step inputs to the valve.

figure, a 1.3-volt step, or 130-micron free displacement, was imparted at various times with differing results, clearly the result of an extremely slow transient effect.

To explore the nature of this effect further, step inputs of varying amplitudes were provided to the stack and the resulting pressure was observed. With low voltage steps, pressure would quickly rise then fall off slowly, similar to that seen in Figure 2.28 continued to occur. This continued to occur until a certain voltage was reached, in which case the downstream pressure followed the initial transient, then steadied out at the supply pressure. The downstream pressure response caused by various step inputs to the valve is shown in Figure 2.29, which illustrates the nonlinear behavior of the valve that is henceforth referred to as "valve hydrodynamics".

It was found that using smaller atomizers affected the response considerably, as the rise time τ and the transient during $t > \tau$ became much longer. Naturally, as the system's resistance decreases, one would expect that the potential energy stored in a member with finite stiffness would dissipate at a much slower rate. If some part of the valve stem were

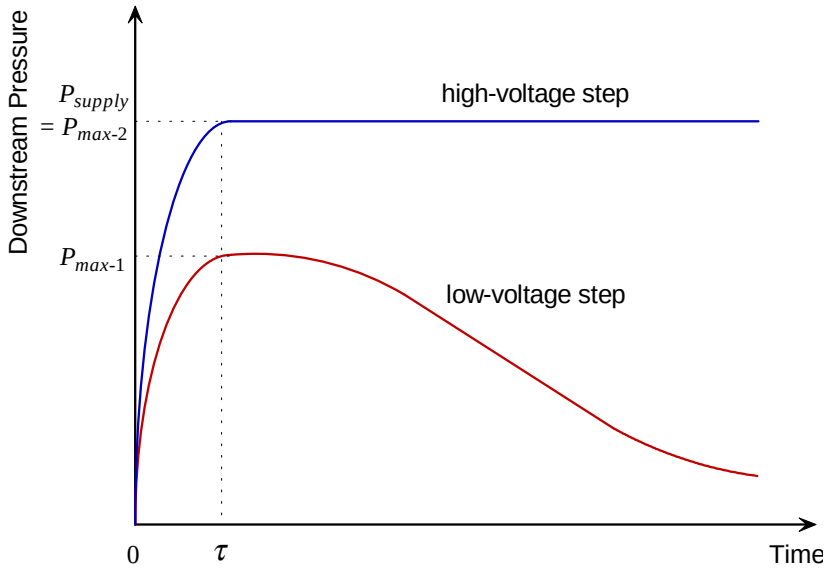

Figure 2.29: Conceptual time history of pressure behavior for two step inputs to the valve.

deflecting with a net increase in potential energy, these transients would be expected if the stem were to be instantaneously moved. This spring-damper theory is further supported by the fact that the transient during $0 < t < \tau$ follows the characteristics of a first-order system. Also, it was observed that the $t > \tau$ behavior depicted by the blue line in the above figure occurred at lower downstream pressures as the atomizers decreased in size. These hydrodynamic trends would severely limit the ability of small FN atomizers to obtain the desired modulation levels and mean flow rate settings. Because τ improves with FN, a downstream metering bypass valve was inserted in the line between the throttle valve and the nozzle so that the downstream FN may be properly set to achieve the desired modulation levels.

In an attempt to validate the theory of a system controlled by the stiffness of the valve's components, the pressure transient should be correlated with the valve's offset. Due to limited ability to measure the displacement of the valve face, the stack's position was measured instead using an optical displacement sensor as shown in Figure 2.23. Upon performing identical testing, the stem displacement followed the same trend as the downstream

pressure, but a total motion of only 4 microns resulted. It was concluded that deflection of the stack is likely not the only reason for the pressure variation; it is possible that either the stem itself or the valve face was deforming in some way.

Accurate understanding these hydrodynamic effects is obviously crucial in modeling the frequency response of the valve's flow rate. In an attempt to determine if the hydrodynamic regime during $0 < t < \tau$ is in fact dominated by linear effects, hysteresis curves of the pressure to the input voltage would reveal a curve similar to that simulated in Section 2.6.2. A series of hysteresis curves was generated with a 1-Hz sine wave imparted on the stack while monitoring the downstream pressure and the reference voltage. The supply pressure was set to 550 psi when the valve was closed and the bypass valve was set to two turns open, corresponding to a FN of 2.1. Data was collected with varying mean pressures by manual real-time adjustment of the stack's offset voltage. The tests were again repeated with the bypass setting at four turns, or a FN equal to 5.2. Because the mean voltage cannot be correlated with pressure, the hysteresis curves were manually shifted so that the locus of the data points would generate an even curve.

Figure 2.30 shows these the result of these tests. Based on these plots, it is apparent that the valve's offset range is broadened by the hydrodynamics, because the inferred reference voltage is 4 volts greater than the amplifier's saturation point of 5 volts. Another noticeable characteristic is the nonlinear loop that occurs in the data at high voltages. At the top of the loop, the pressure slowly decreases with time, which is because of the accumulator's transient draining. While the linear portion of the curve appears to be similar in shape to that from Figure 2.21, the voltage sensitivity is much less than that predicted in the simulation. Thus, the amplitudes cannot be assumed to be dominantly linear within the range $0 < t < \tau$ and therefore cannot be identified with a transfer function.

Based on testing conducted thus far, three important results are revealed. For one, these hydrodynamic effects result in the maximum achievable pressure resulting from a step input to occur at time $t = \tau$, with reference to Figure 2.29. From the step characteristics

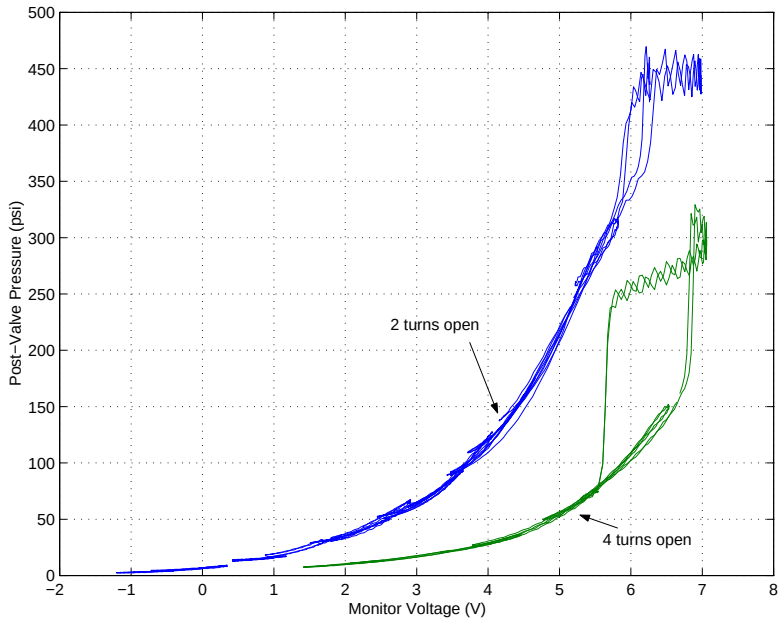

Figure 2.30: Hystersis curves at bypass valve settings of two and four turns.

of the pressure during $0 < t < \tau$, it appears that these effects can be described by a first order, high-pass system, whose rise time τ is dependent on the downstream flow number. It is possible that the bypass FN may be optimized such that the hydrodynamic bandwidth could be increased close to the instability frequency to maximize the achievable amplitude. Another result is that, due to the nonlinearities present, the valve system is not easily modeled. Thus, prediction of the a priori performance of the throttle valve would be more difficult than previously thought. A third result is that the nonlinear transient following τ does not allow a mean position to be held constant by open-loop control of the valve. Thus, some sort of feedback control would be necessary to maintain a desired mean pressure.

2.7.3 Mean Position Controller Development

It so happens that the PSt1000/16/500 actuator possesses a large amount of unused displacement over a large portion of the frequency range of interest, and this unused capability

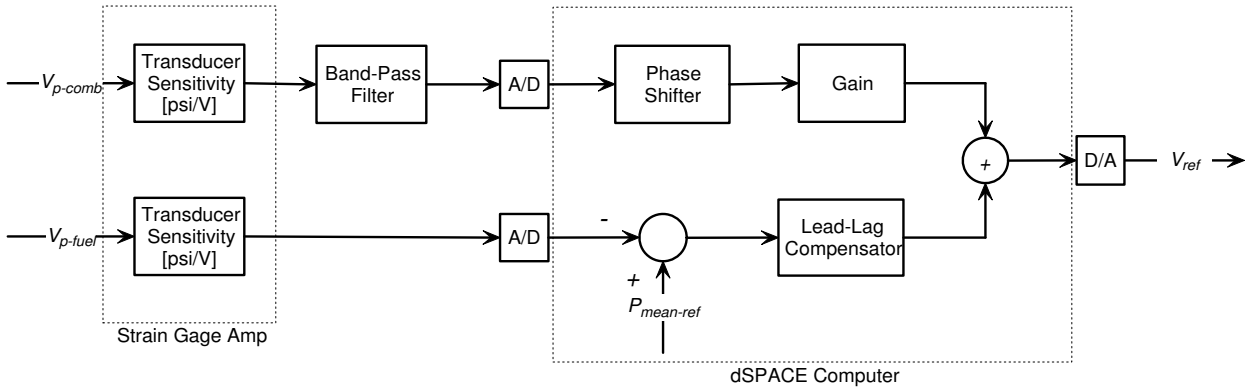

Figure 2.31: Block diagram of the phase shift and mean position controllers for the throttle valve.

may be used to compensate for the valve's drift. For the immediate need, this is favorable because a second actuator will not be needed to complicate the valve design. This low-bandwidth position controller was designed in SIMULINK and would be downloaded to the dSPACE computer as a modification to the phase shifting program originally created to control the stack. This controller would maintain a certain mean pressure by utilizing the downstream pressure transducer signal along with a user-defined reference pressure. It was decided that a lead-lag compensator would be suitable for control if the corner frequency were to be placed at about 10 Hz, well below the combustion control frequency range. An open loop block diagram of this controller is found in Figure 2.31. For more specific detail on this controller, the reader is referred to Schiller, due in late 2003.

The mean controller performed well with every atomizer except those with low flow numbers, namely those with a 0.5 size or smaller. It is most likely that the reasons for this are the same as the observations made in the previous subsection. To overcome these effects, the downstream FN was adjusted with the bypass valve would need to be adjusted to allow the stack to achieve control at lower downstream pressures.

2.8 Chapter Summary

The main outcome of this chapter is that the expected modulation levels of both the piston and check valve designs were different than anticipated given the present level of understanding of each system. It was shown that the piston/check valve exhibited modulation that was lower than expected because of the effects of compressibility. On the other hand, the throttle valve had more authority potential depending on the flow number setting, as it was limited by hydrodynamic deflection of the valve. Identification of these authority-limiting phenomena is important because it is possible that one can improve authority considerably by making informed corrections to each fuel injector device. This would save having to correct the situation by scaling the actuators, obviously resulting in a more costly, cumbersome system. Also, this reduces the possibility of the actuators suffering from being significantly band-limited, as was the case in selection of the PSt1000/16/500 actuator.

Both systems were designed based on a maximum modulation level of 40% of the mean flow, but each had different mean flow rate criteria. The piston design was intended for use with a 0.4 atomizer, while the throttle valve was capable of higher flows, and was designed for a 4.0 atomizer. The piston/check valve device modulated close to 22% of its intended level and was severely limited by compressibility effects. The throttle valve was marked with several non-ideal behaviors; namely, a slow drifting of the downstream pressure, due to hydrodynamic deformation of the valve. Closed-loop control was implemented to maintain a constant valve position, but a fast transient effect was also found to affect the system. Although this effect could not be characterized due to its nonlinear nature, it would provide for large amplitudes given a high downstream FN and upstream pressure setting.

The focus of the remainder of this research is to develop and validate tools through which a designer may identify and eliminate problem points for fuel modulation and then down-select actuators to meet the desired requirements. Improvements to a design approach that may be considered ad hoc has motivated a detailed look into the acoustic nature of each fuel injection system. The following chapter will reveal the results of acoustic modeling of

the two fuel injection systems to assist to that end.

Chapter 3

Acoustic Flow Analysis and Validation Experiments

In active combustion control, the necessary equivalence ratio fluctuations required to stabilize an existing thermoacoustic instability are a result of fuel velocity perturbations at the flame. To date, researchers have not succeeded in describing dynamic velocity characteristics in fuel injector systems with the intent of determining the performance of a given fuel injection system in realistic combustor environments. It is the goal of the present research to introduce modeling tools that will enable designers to identify the hardware required to create desired velocity perturbations, which would enable prediction of the authority of certain ACC systems with respect to an intended combustor application.

Because of practical requirements, ACC fuel injection systems must be placed at least several inches away from the atomizer at the combustion location. This is not only because of thermal loading and limited space considerations, but also because the fuel injectors may be required to drive multiple atomizers around the annulus (see Table 2.1). In most aero gas turbine combustor applications, ACC hardware must be placed upstream of the fuel manifold, so the distance between the injector and each atomizer would vary anywhere

between 9 inches to 3 feet. Because of the acoustic interaction of the fuel line components with the actuated fuel waveform, determining the exact level of fuel modulation is likely to be difficult without the aid of reliable models. At high frequencies, the dynamics of the fuel line are described by acoustics, which means that the reactive nature of area changes within the flow path may cause attenuation of the pulse at the atomizer. In extreme cases, the velocity may be influenced by resonances and antiresonances at discrete frequencies. Without a prior understanding of these effects, it would be difficult to design fuel injectors to meet desired authority criteria especially in light of weight, size, and power efficiency requirements.

By validating simple modeling techniques, designers may estimate the unsteady injection velocities for any fuel injector device installed in an arbitrarily complex fuel delivery system. This model may then be used to investigate their performance at actual working conditions, where replication on a bench test stand becomes costly and impractical. Additionally, the model may allow designers to rapidly identify the best hardware setup for the particular application by allowing a simple means to study the trade offs between different fuel injector configurations and actuator types. Techniques to further minimize the actuator size may then be sought out, such as elimination of dissipative mechanisms and acoustic amplification of the narrowband response, such as utilization of acoustic resonances.

In this chapter, the methodology for modeling the two fuel injection designs from Chapter 2 will be presented. Specifically, the models were formed using one-dimensional transmission line methods to assess the forced response (particular solution) of the flow rate at the atomizer exit. These fuel injector devices were validated through experimentation by starting with well-known boundaries and progressing towards those that were more complex and realistic. By using a phenomenological approach, several key components could be isolated, allowing their dynamics to be fine-tuned in a methodical and accurate manner. This analysis culminated in performance validation experiments at scaled conditions close to those used for combustor control experiments.

3.1 Water Bench Test Apparatus

A water-based test stand was developed in order to conveniently perform most of the validation experimentation in this study. The system was designed to reproduce the fuel injection system in the combustor bay, consisting of primary and secondary supply lines as shown in Figure 3.1, similar to the system in Figure 2.18, with the exception of the combustor inlet. Pumps #1 and #2 were piston pumps, both of the same model number as that from Section 2.6.1. The pumps on both lines fed into regulation networks, followed by a pulsation dampener on the primary line and a pulsation dampener and accumulator on the secondary line. The two lines fed into flow meters, then into fine-adjust needle valves before entering the two fuel injection devices. Note that the check valve is not present in the primary line, which is because subsequent studies were focused on the effectiveness of the piston with a simple line constriction. Because both systems were to be tested in primary line arrangements, ball valves on the primary and secondary lines (#1 and #2, respectively) were shut off depending on which device was being tested. The piping lengths between those valves and the adjoining tee coupler were kept as short as possible to minimize their acoustic influence. A bypass valve was installed on the throttle valve system to improve the response characteristics with low-FN atomizers. For this system, 1/4-inch stainless steel and copper tubing was used downstream of the regulation valves, with Swagelock fittings to connect the various components.

Several arrangements were to be used for the specific validation tests and diagnostics of the two injection systems. Tubing lengths downstream of the injection devices were chosen to obtain dynamics within a frequency range between zero to 800 Hz. For the preliminary work, two tube coil lengths were chosen: one eight feet in length and the other five feet in length. Several Entran steel diaphragm pressure transducers were used to obtain dynamic measurements, identical to those used in Section 2.5.3. In the throttle valve line, a transducer with 1000-psi dynamic range was placed five inches upstream of the valve inlet, while a 500-psi transducer was located seven inches downstream of the valve outlet. In the piston line,

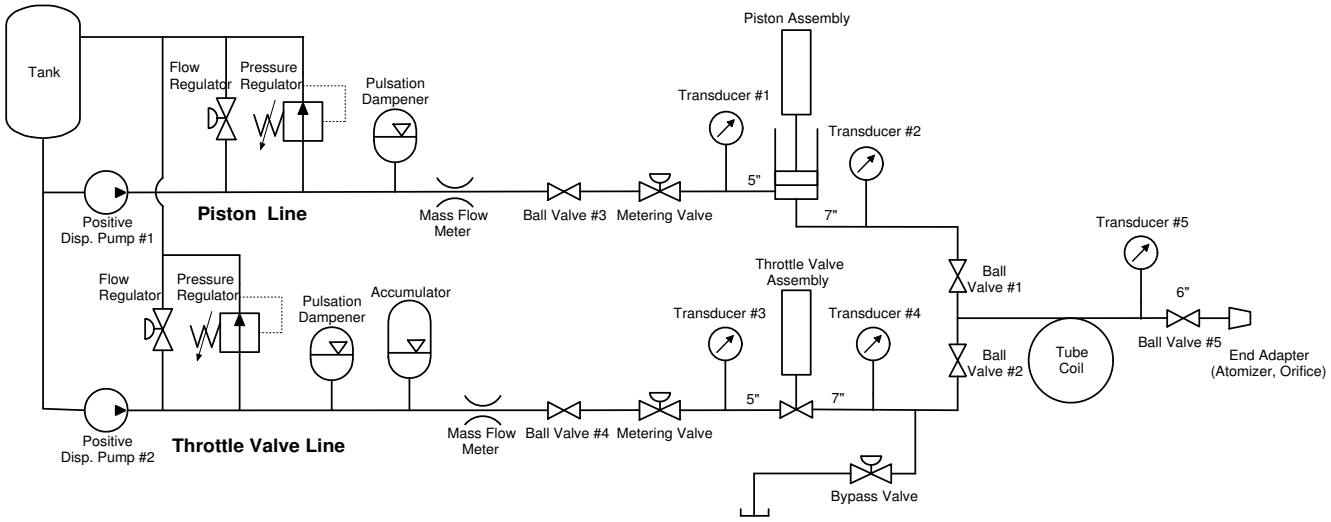

Figure 3.1: Schematic of water-based fuel injector test system.

the transducers were placed at the same locations relative to the inlet and outlets, but a 500-psi transducer was used on the upstream side. An additional 500-psi transducer was placed six inches before the end adapter to estimate the pressure at the boundary. The transducer signals were fed into a Vishay Measurement Instruments 2100 stain gage amplifier and signal conditioner. Data acquisition and signal generation were both performed with an HP FFT analyzer. In order to test the various boundary condition scenarios, the end conditions had the ability to be adapted to different configurations. To create rigid boundary conditions, ball valve #5 immediately upstream of the end adapter and either #3 or #4 upstream of the fuel injectors were shut. To create boundaries with flow, the ball valves would be open and the upstream impedance adjusted with the metering valve. An adapter at the end of the piping was fitted with either an orifice plate or one of various atomizers, depending on the conditions to be tested.

3.2 General Acoustic Equations

The present analysis utilizes the solution of the acoustic wave equation to solve for the acoustic standing waves within a bounded system. A numerical simulation was initially considered for the analysis of these fuel injection systems [1], but this approach was abandoned due to several practical issues. For one, the simulations would be too time consuming to provide usefulness and, for another, the level of understanding on how the separate fuel components affect modulation would not be gained. Thus a one-dimensional, linear transmission-line approach was developed for the analysis. These transmission line models were formed using the matrix form of the one-dimensional equations of motion and continuity to determine the pressure and velocity oscillations at any point in the medium. The matrix allows for coupling between the separate elements, the dynamics of the actuator, and the end impedances. In order to fully understand the formulation and assumptions of the present models, it is necessary to begin with the derivation of the wave equation.

3.2.1 The State Equation and Conservation Laws

In acoustics, energy is transferred by the compression and rarefaction of a fluid medium. The motion of a pulse moving through a fluid is governed by conservation of mass and conservation of energy. The compressibility of the particular medium governs sound speed, which is defined as

$$c^2 = \frac{\partial p}{\partial \rho} \tag{3.1}$$

An ideal gas undergoing an adiabatic compression is governed by the state equation

$$\frac{p}{\rho^\gamma} = \frac{p_0}{\rho_0^\gamma} = a \tag{3.2}$$

where a is a constant. This can be rearranged to obtain

$$\gamma \ln v + \ln p = \ln a \tag{3.3}$$

where v is the specific volume, v or $\frac{1}{\rho}$. Differentiation of the above equation yields

$$\gamma \frac{\partial v}{v} + \frac{\partial p}{p} = 0 \tag{3.4}$$

Rearranging and substituting density for volume, we have

$$\frac{\partial p}{\partial v} = -\frac{\gamma p}{v} = -\frac{\rho^2}{m}\frac{\partial p}{\partial \rho} \tag{3.5}$$

The definition of the sound speed in terms of the properties of the medium is thus

$$c^2 = \frac{\gamma p_0}{v_0} \tag{3.6}$$

where p_0 and ρ_0 result because it is assumed that the amplitude of these quantities is much smaller than their mean component. The sound speed can be thought of as the ratio of the reactance terms, where the compliance of the fluid is in the numerator and the inertia is in the denominator.

The conservation of mass is used to account for the fluid's motion by relating the particle velocity to the density. This relationship is based on the assumption of no-slip conditions, where the fluid does not cavitate or separate from the walls. The net flow of fluid entering a differential volumetric element causes an increase in density of that volume to increase. The corresponding equation is

$$\frac{\partial u(x,t)}{\partial x} + \frac{1}{\rho_0 c^2}\frac{\partial p(x,t)}{\partial t} = 0 \tag{3.7}$$

The first term of the equation represents the net velocity entering the elemental volume; the second term represents the density increase due to the mass flux.

The equation of motion is necessary to describe any dynamic system, so it is necessary to write the conservation of momentum that results in Euler's equation. The momentum equation is written in general, three-dimensional terms as

$$\frac{d}{dt}\iiint_V \rho u dV = \iint_S \mathbf{f}_S dS + \iiint_V \mathbf{f}_B dV \tag{3.8}$$

which represents Newton's Second Law, with the sum of the momentum on the particles composing a certain volume equivalent to the sum of the forces acting on that volume. The

force $\mathbf{f}_S$ is the surface force per unit area exerted on the fluid, while $\mathbf{f}_B$ is the body force exerted on the fluid. The body force is neglected due to the small contribution of gravity on fluid particles. The fact that the surface forces act normally on the surface implies $\mathbf{f}_S = -\mathbf{n}p$ and results in

$$\iint_S f_S dS = -\iiint_V \nabla p dV \tag{3.9}$$

With substitution of this equation into Equation 3.9, exchanging the time derivative in the left-hand side of Equation 3.9, and recognizing that the integrand must be zero results in Euler's Equation:

$$\rho_0 \frac{d\mathbf{u}(x,t)}{dt} = -\nabla p(x,t) \tag{3.10}$$

Another form of the conservation of momentum is the unsteady Bernoulli equation, which is spatially resolved at discrete locations in the fluid. The linear, one-dimensional form of this equation is as follows:

$$\frac{p_2(t) - p_1(t)}{\rho_0} = -\int \frac{\partial u(x,t)}{\partial t} dx + \bar{u}\left(u_1(t) - u_2(t)\right) \tag{3.11}$$

The solution to the resulting wave equation is the combination of the three relationships such that they form the equation of motion in terms of either pressure or velocity potential. Writing the wave equation in terms of pressure gives

$$\frac{\partial^2 p(x,t)}{\partial x^2} = \frac{1}{c^2}\frac{\partial^2 p(x,t)}{\partial t^2} \tag{3.12}$$

An important assumption inherent in the wave equation is that the perturbed levels are small compared with the absolute quantities, i.e. $u(x,t) \ll u_0$ and $p(x,t) \ll p_0$. The steady-state solution to the wave equation was found by deLambert, who proved that the total perturbed solution is a superposition of any function traveling in the positive direction and any function in the negative direction:

$$p(x,t) = F_1(\omega t - kx) + F_2(\omega t + kx) \tag{3.13}$$

which, for the case of pure-tone harmonics assumes the form:

$$p(x,t) = Ae^{j(\omega t - kx)} + Be^{j(\omega t + kx)} \tag{3.14}$$

Using Euler's equation, we can write the corresponding expression for the particle velocity as:

$$u(x,t) = \frac{1}{\rho_0 c}\left[Ae^{j(\omega t - kx)} - Be^{j(\omega t + kx)}\right] \tag{3.15}$$

The unknowns are the complex-valued coefficients that are determined by imposing boundary conditions on a multi-dimensional system. As will be shown in the next section, this equation is used in conjunction with continuity and momentum relationships along with discrete boundary conditions to form models for complex systems.

3.2.2 Transmission Line Modeling

It is not possible to obtain a closed-form solution by performing eigenfunction analyses in systems that are described by more than two boundaries. The geometry of the plumbing system, upstream and downstream boundaries, and the fuel injection device all contribute relatively large changes in cross-sectional area. Transmission line models may be developed to account for these geometrical complexities, along with the dynamic properties of the actuator and prime mover, the upstream and downstream boundaries, and the dynamics of inhomogeneous elements within the fluid, such as air bubbles.

The fuel delivery system's geometry is characterized by long tubing lengths with discrete area changes in the streamwise direction. Since the system involves several coupled elements, it is customary to form the expressions for pressure and velocity in matrix form to solve for the unknown coefficients. For each element, there are two coefficients to solve for: one for the forward traveling wave and one for the reverse. Thus, for M separate elements in the system, the total number of equations must be equal to $2M$. There are N discrete boundaries in any system and for any one-dimensional system of finite extent, N must at least equal two. This is illustrated in Figure 3.2, which shows a simple case with two elements and two boundaries. If the wave originates from a piston at $x = 0$, as the wave reaches $x = L_1$, a portion of the wave is reflected and a portion is transmitted to the next section. The same happens with the reflected wave when it reaches $x = 0$. Mathematically, the interfaces

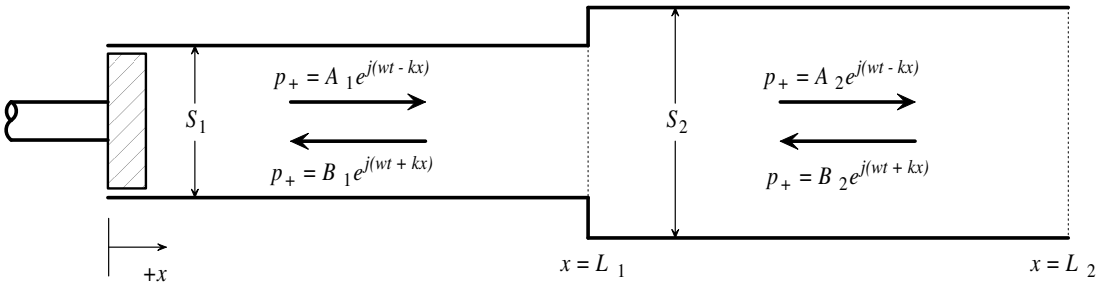

Figure 3.2: Simple transmission line model with two elements and two boundaries.

and boundaries in which a wave can experience a local reflection are represented by acoustic impedances and determine which basis functions exist within the entire system.

For each element, the continuity and momentum expressions are solved at each interface to account for the $2M - N$ remaining equations needed to solve for the coefficients. For the system shown in Figure 3.2, there would need to be two equations representing the interface between the two elements. The wave equation solution would then be substituted into these conservation expressions of the system by forming the equations with the deLambert solutions to the wave equation. For each interface between elements, such as a change in the cross-sectional area, conservation equations are written as:

$$p_{in,1}(L,t) = p_{in,2}(L,t) = \ldots = p_{in,m}(L,t)$$
$$= p_{out,1}(0,t) = p_{out,2}(0,t) = \ldots = p_{out,n}(0,t) \tag{3.16}$$
$$\sum_{i=1}^{m} Q_{in,i}(L,t) = \sum_{j=1}^{n} Q_{out,j}(0,t) \tag{3.17}$$

The interface between elements is treated as an infinitely thin control volume. Only the fluctuating quantities are used in these expressions, so the $p(x,t)$ are the total fluctuating acoustic pressures and the $Q(x,t)$ are the total fluctuating acoustic volume velocities. The first equation is a result of imposing zero resistance and zero reactance on the unsteady Bernoulli's equation from Equation 3.11, while the second equation is simply the continuity expression from Equation 3.7. Note that these equations are generalized for more than two elements meeting at an interface, where m is the number of inlet elements and n is the

number of outlet elements. The usefulness of this system of equations becomes apparent when placing Equation 3.17 in terms of cross-sectional areas S and total acoustic particle velocities $u(x,t)$:

$$\sum_{i=1}^{m} S_{in,i} u_{in,i}(L,t) = \sum_{j=1}^{n} S_{out,j} u_{out,j}(0,t) \tag{3.18}$$

For the particular system in Figure 3.2, Equations 3.16 and 3.18 simplify to:

$$\begin{aligned} p_1(L,t) &= p_2(0,t) \\ S_1 u_1(L,t) &= S_2 u_2(0,t) \end{aligned} \tag{3.19}$$

If the above example were altered at $x = L_1$ with an interface with one inlet and two outlets, as would be the case if a side branch were in the system, there would be three elements and three boundaries, so three continuity expressions result. It is fairly obvious from Equations 3.16 and 3.18 that the following system of equations results:

$$\begin{aligned} p_1(L,t) &= p_2(0,t) \\ p_1(L,t) &= p_3(0,t) \\ S_1 u_1(L,t) &= S_2 u_2(0,t) + S_3 u_3(0,t) \end{aligned} \tag{3.20}$$

where element 3 designates the second fluid outlet from the interface.

For most zero- or low-flow cases, the assumption of zero resistance and reactance at a minor area change is acceptable in order to simplify the unsteady Bernoulli's equation. However, when flow is present in a small constrictive area, one can no longer ignore dissipation of the fluid's kinetic energy. Viscous losses act on the fluid at discrete locations in the domain, necessitating a local resistance to be included in the model. An inductance may also exist if the restriction volume contains enough mass to be considered appreciable.

As with interfaces, boundaries are represented by impedances, which are governed by conservation laws. Because boundaries only require one equation to model their effects, a choice must be made to determine which conservation law may suitably describe the boundary in question, which is very much dependent on its physical nature. In most situations in

acoustics, the driver's dynamics are coupled with the fluid system. In order to allow coupling to exist, a mechanical impedance must be used, which is simply Newton's Second Law. The definition of the mechanical impedance is as follows:

$$Z_m = \frac{f(t)}{u(t)} \tag{3.21}$$

In the case of an actuator's input to the system, the equation of motion is written in terms of voltage input to the amplifier, the force generated, and the displacement. When differentiated with respect to time, an expression relating the total acoustic velocity and pressure at the actuator location and the input voltage results.

End conditions based on the unforced equation of motion, found in the same manner as with the input mechanical impedance. For a second order mass-spring-damper boundary, the impedance takes the form:

$$Z_m = c + j\left(m\omega - \frac{k}{\omega}\right) = R + jX \tag{3.22}$$

where R is termed the resistance and X is the reactance. The resistance and reactance terms are found by forming Bernoulli's equation at the boundary. The derivatives are replaced by their Laplace representations, yielding a dissipative term and a reactive term. Applying the relationship $Z = \frac{p(t)}{u(t)}$ will arrive at the form in Equation 3.22.

Forming the model of the system of Figure 3.2, with a piston at $x = 0$ with dynamics represented by Z_m with input voltage V_{in} and a boundary at $x = L_2$ represented by Z_2 yields the following matrix:

$$\begin{bmatrix} -S_1 + \frac{Z_m}{\rho c} & -S_1 - \frac{Z_m}{\rho c} & 0 & 0 \\ e^{-jkL_1} & e^{jkL_1} & -1 & -1 \\ S_1 & -S_1 & -S_2 & S_2 \\ 0 & 0 & -S_2 + \frac{Z_2}{\rho c} & -S_2 - \frac{Z_2}{\rho c} \end{bmatrix} \begin{bmatrix} A_1 \\ B_1 \\ A_2 \\ B_2 \end{bmatrix} = \begin{bmatrix} V_{in}G_a \\ 0 \\ 0 \\ 0 \end{bmatrix} \tag{3.23}$$

The factor G_a represents the product of the amplifier gain and piezoelectric constant, providing a relationship of the force generated to the voltage input. By setting up the matrix in

this way, each interface can be thought of as a locally reactive boundary condition. In most zero flow cases at small perturbation amplitudes no local resistances exist at low frequencies, i.e. $ka \ll 1$. In reality, dissipative effects due to the fluid's properties exist, necessitating absorption to be introduced with an imaginary-valued wavenumber:

$$k^2 = \frac{\omega^2}{c^2} + \frac{2j\omega}{c}\alpha \tag{3.24}$$

where a is the absorption coefficient due to classical viscothermal effects within the fluid and viscous effects due to the walls [34]. Localized resistances involving mean flow effects will be discussed in the following sections. Models formed for each system outlined in this chapter will be created in this fairly straightforward matrix formulation.

3.3 Characterizing Compressibility Effects

Compressibility was introduced in Chapter 2 as a contributing factor in the performance degradation of the piston/check valve assembly. It was therefore important to include an analysis of its effects so that unsteady flow models could be accurate to the real system. A fairly accurate method testing the hypothesis of air content within an atomizer was by placing the check valve assembly in-line with a short downstream tubing length. Assuming the dominant process is the compressibility dynamics, closing the valve with a step input to the stack would reveal the first-order decay transient of the bubble. Through a small amount of testing, it was clear that, by purging some air out of the fuel line, the transient decay time could be lessened, as shown in Figure 3.3 for the 0.4 atomizer. Using the relationship for atomizer FN, the bubble volume can be approximated by integrating the transient flow rate over time. This method resulted in the prediction of 82 cc of air for the baseline case and a volume of 0.5 cc for the well-bled case. Thus for subsequent experiments, the air would be minimized by pressurizing the system with the atomizer being oriented vertically and manual tapping along the fuel line. This bleeding procedure was repeated until a fairly consistent step response was obtained over the course of time. Because this final response could not be

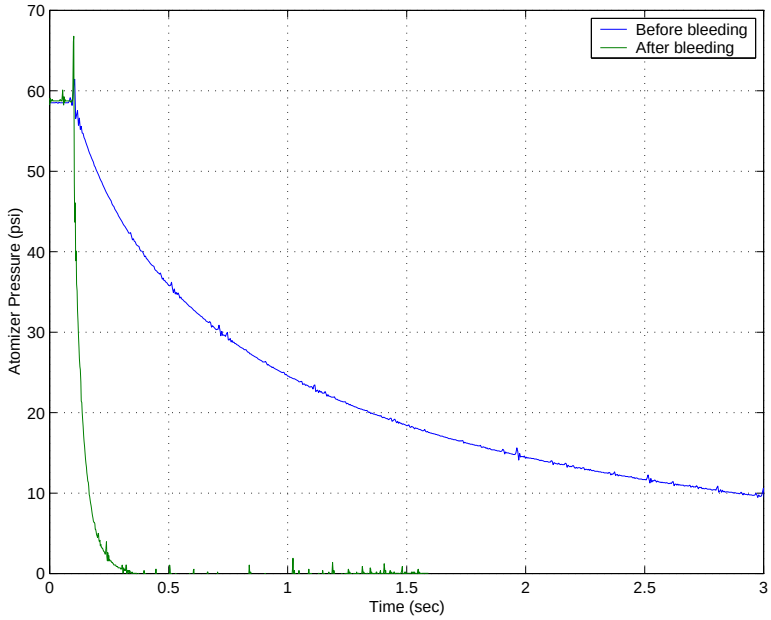

Figure 3.3: Valve closure step response for two air volumes with a 0.4 atomizer.

further improved, there exists the possibly of another compressibility mechanism within the line.

In order to understand the effects of that trapped air on the fuel injector's performance, an impedance must be derived by modeling the air bubble. First-order systems are characterized by a capacitance that represents the air bubble, and a resistance that describes the atomizer. Writing Bernoulli's Equation across the atomizer, the following relationship results:

$$\triangle p = p - p_{amb} = RQ^2 \tag{3.25}$$

where p is the pressure upstream of the atomizer and p_{amb} is the ambient pressure. The resistance may be substituted for the flow number using the relationship

$$R \equiv \frac{\rho}{FN^2} \tag{3.26}$$

Capacitance is defined as the change in volume with respect to a change in pressure, $C \equiv \frac{dV}{dp}$,

which results from an application of the chain rule to the volume flow rate:

$$Q = \frac{dV}{dt} = \frac{dV}{dp}\frac{dp}{dt} \tag{3.27}$$

Applying the definition to Equation 3.2 yields the following:

$$C \equiv \frac{dV}{dp} = a^{1/\gamma}\frac{d}{dp}\left(p^{-1/\gamma}\right) = -\frac{V}{\gamma p} \tag{3.28}$$

concisely stated as the fluid's volume divided by its bulk modulus. The capacitance varies with respect to instantaneous values of volume and pressure at any point in time, making it a nonlinear relationship.

The combination of Equations 3.25, 3.27, and 3.28 results in a nonlinear differential equation, given by

$$-RC^2\frac{d^2p^2}{dt^2} + p = p_{amb} \tag{3.29}$$

where p_{amb} is the input to the system. In order to numerically solve this equation, a SIMULINK model was developed given a step input to the pressure. In order to corroborate the model, the time decay of a known volume of air inside the system accumulator was determined. The accumulator's air content (30 in^3) was known based on the estimate provided by the manufacturer. When Equation 3.29 was simulated, the results showed that the model matched the experimental curve well for the first half of the pressure transient and then predicted a slope that was less than that of the air volume for the remainder of the transient, possibly because of a non-ideal effect within the accumulator. The two pressure decay transients from Figure 3.3 were simulated with the bubble volumes found from the integrated flow transient. The results, shown in Figure 3.4 (a) and (b), reveal that the bubble volume effects are appropriately modeled and that flow profile integration is an accurate measure of the compressibility.

In order to incorporate compressibility into the models a parallel branch in the transmission line system must be generated. At this branch, an impedance relation may be written using Equations 3.22 and 3.28, which takes the form:

$$Z = j\frac{k}{\omega} = j\frac{S\gamma p_0}{\omega V_0} \tag{3.30}$$

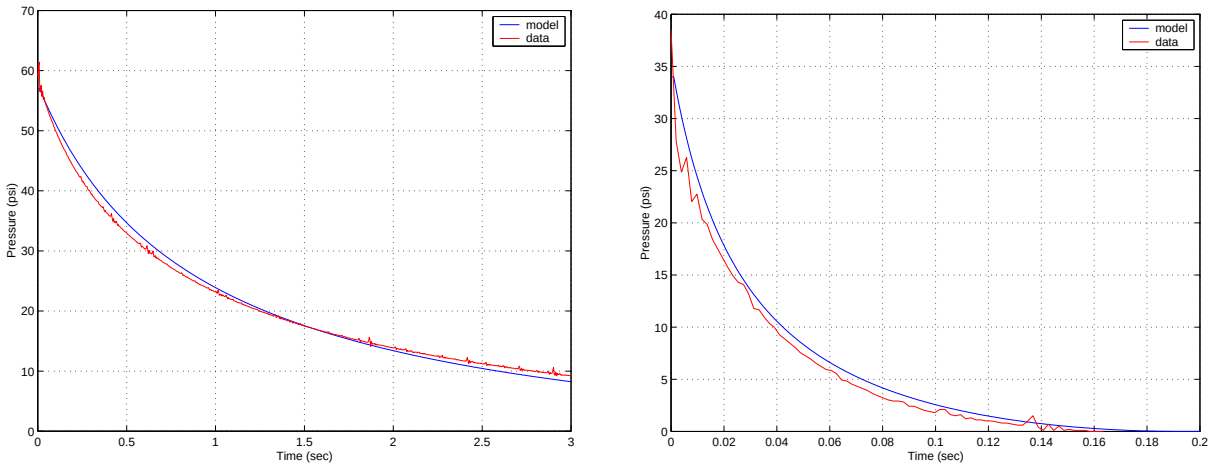

(a) **(b)**

Figure 3.4: Simulated pressure decay transient for air volumes of (a) 82 cc and (b) 0.5 cc.

again assuming the perturbation is small and that there is no inertance. Clearly, the exact bubble location must be known so, in the models developed later, this location would have to be assumed.

The extent to which compressibility affects actuator authority is quite dependent on the particular situation the designer is dealing with. For one, the fact that the ambient pressure in gas turbine combustors is several hundred psi, instead of atmospheric used here, the volume may be sufficiently small that it becomes inconsequential. Moreover, the decay time decreases as the atomizer's flow number increases due to the lower flow resistance, and more so if operating at a high pressure gradient across the atomizer. Thus, designers that are faced with these problems with bench top fuel injector validation may not be able to obtain the true performance capabilities that would exist in the end application.

3.4 Modeling Approach for Piston and Throttle Valve

Transmission line models for the two injector devices were constructed by first identifying discrete area changes within the fluid system. The models were nearly comprehensive in detail to avoid the possibility of incorrectly modeling parts of the system. As far as an acoustic source input to the system, the piston fuel injection system was the simpler of the two configurations to model and was therefore validated first. A closed system was the first scenario to be considered so that it could easily be identified which parts of the system were not modeled properly. This is facilitated by the fact that the boundaries are well known and the system would be uncomplicated by mean flow effects. A scenario with an orifice plate at the end of the tube was studied next. Here, the presence of flow effects must be given consideration as well as the addition of the upstream supply line. Transmission losses to the upstream section without the check valve in place could thus be addressed, in which realizations for an acceptable replacement component may be evaluated. Lastly, the model was validated with an atomizer at the end boundary. This will lead into evaluation of the scalability of the models at various operating conditions and actuation amplitudes.

For the throttle valve, an identical approach to the modeling scenarios will be performed. However, the orifice plate scenarios would not need to be conducted because accurate models of the atomizer would have already been created. For the closed-tube tests, the throttle valve's uncertainties were in its internal geometry, its source input characterization, and the effect of modeling a constant valve discharge area. When flow is introduced, it will be shown that an additional source term due to the pressure gradient becomes influential, and must be correctly modeled to determine the system's response. After this was performed, the viability of small-amplitude models in predicting large-amplitude response characteristics over a range of operating conditions will be presented.

Frequency response functions (FRFs) of the pressure at the two aforementioned locations versus the driving amplifier monitor output voltage were gathered and compared to the models' output. In generating FRFs with a monitor voltage reference, the amplifier's

Table 3.1: Dynamic parameters of the piston fuel injector system.

Stack Stiffness, k **(N/**μ**m)**	**Stack Effective Mass,** m **(g)**	**Amplifier Gain,** G_a **($\mathbf{V_{stack}/V_{in}}$)**	**Piezoelectric Constant,** G_p **($\mathbf{N/V_{stack}}$)**
202	17.2	30	8.26

dynamics would not need to be included, removing this potential source for error. For most of the tests, a 1-volt white noise signal was used as an input signal in order to obtain the best coherence possible and to minimize any nonlinearities that may exist with large amplitude signals. Because the pressure measurements cannot be taken at the nozzle exit when installed in a combustor, the location where we care to obtain the unsteady velocity, the modal response of the system is very important. At a location close to the prime mover within any bounded system, the measurement is termed collocated if a zero follows each pole. Close to the end boundary, i.e. the atomizer, these zeros occur at higher frequencies.

3.5 Piston Device Models and Experimentation

The piston designed in Chapter 2 was used in this set of experiments, with the PSt150/14/20 actuator as the driver because only small displacement amplitudes were required for these tests. The parameters of the 20-micron stack were included in the mechanical impedance term to represent the input to the system. Several empirically determined parameters of the actuator and prime mover are shown in Table 3.1. The mechanical impedance would be the input to the system, whose model is developed in the following section.

The system consisted of the metering valve that connected with the inlet of the piston device as shown in Figure 3.1. Downstream of the piston, a branch with a bleed line was installed, followed by an interchangeable tube coil, and the end adapter, which depends on whether or not the ball valve was open. The transmission line component diagram, broken

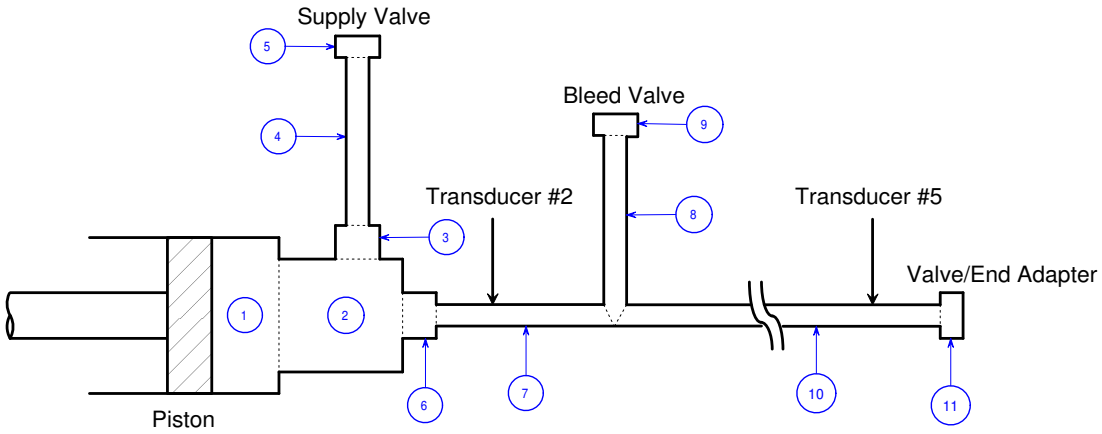

Figure 3.5: Transmission line component diagram of piston assembly with closed valves (not to scale).

into elements, is shown in Figure 3.5. Referring again to Figure 3.1, pressure transducer #2 was located in element 7 at a distance of seven inches from the piston outlet. Pressure transducer #5 was located after the coil tube, six inches upstream of the end ball valve in element 10.

In order to form accurate models of the system, it was first necessary to quantify the compressibility within the hardware. Because the check valve was not available to use due to failure of the PSt1000/10/150 actuator, the time decay method could not be used to find the air bubble volume. Another method would therefore be employed: compare the resonant frequencies between the model and data by iteratively varying the air bubble sizes. The system resonates when the reactance term goes to zero, or when $Im\{Z + Z_0\} = 0$, where Z designates the compressibility impedance (Equation 3.30) and the fluid impedance Z_0 may be written in terms of the eigenfunctions of the fuel injector system. This means that the frequencies of each mode lies at the intersection points of the two reactance curves. As the stiffness increases, the intersection of the two reactance curves increase in frequency and move closer to the zero-stiffness modes at higher frequencies, as seen in the example for a single closed tube in Figure 3.6. In the subsequent models, the bubble volume was

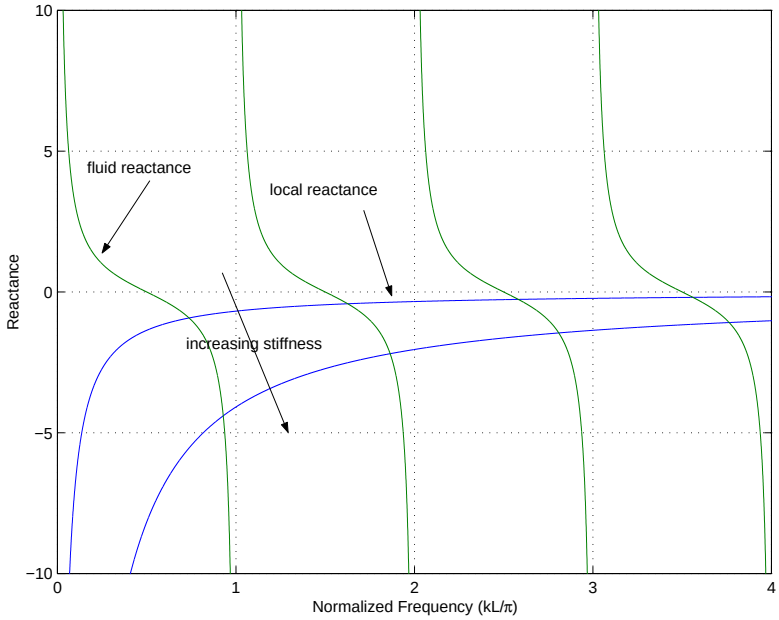

Figure 3.6: Intersection of local impedance, such as compressibility, and the fluid impedance for a straight, closed tube.

iteratively compared to the system's modes in this manner. Due to its dependence on mean pressure, this volume was obtained at a certain pressure and validated by matching the FRFs generated at various other pressures.

3.5.1 Closed Tube Validation and Elimination of Structural Vibrations

For the piston/closed tube experiments, the combined length of elements 7 and 10 was equal to seven feet. As an initial validation test for the models, the system was first tested with unpressurized air in the system. Microphones were placed at the two transducer locations to measure the pressure over the frequency range of zero to 800 Hz. FRFs at measurement location #5 revealed that highly damped half-wave modes existed within the system. The response showed no zeros within the frequency range, which is to be expected if the mea-

surement location is not collocated with the source. In contrast, the response at location #2 revealed that a zero followed each pole, which is indicative of a nearly collocated measurement. Additionally, the six-inch supply line and the four-inch bleed line, which act as bulk stiffnesses at low frequencies, did not significantly contribute to the dynamics. These air-based tests would later prove to be a good benchmark for the expected behavior with liquid media.

The water-based tests that followed were performed by first pressurizing the system with the water pump, then closing off ball valves #1 and #5 when the desired pressure was reached. Upon testing, it was immediately apparent that the data exhibited dynamics that were not present in the model. Zeros appeared at frequencies that were not explainable by measurement location. Moreover, the poles were too low in frequency and the overall amplitudes were well below those predicted, indicating a lower stiffness than expected from the model. It was noticed that, when the tubes were held fixed, the zeros still appeared in the response, but occurred at different frequencies. Also, the poles moved to higher frequencies, approaching those predicted by the models. A reasonable explanation was that, in the present setup, the bending mode resonances of several sections of stainless steel piping was within the measured frequency range and were excited by the actuator. These resonances would remove energy from the fluid system, creating antiresonances at those frequencies and thus reduce the low-frequency amplitudes.

The downstream fuel line was rigidly fixed at several locations so that it would not resonate within the frequency range of interest. Sure enough, this measure eliminated the un-modeled zeros in the data and improved the overall gain by 8 dB, showing that the system no longer lost energy to the vibrating pipes. From a design standpoint, the rigidity of the piping system is an important consideration in the authority potential of a fuel injector system.

Figure 3.7 shows the result of data gathered at various mean pressures, measured at transducer location #2. Note that the response is in units of SPL with a standard liquid

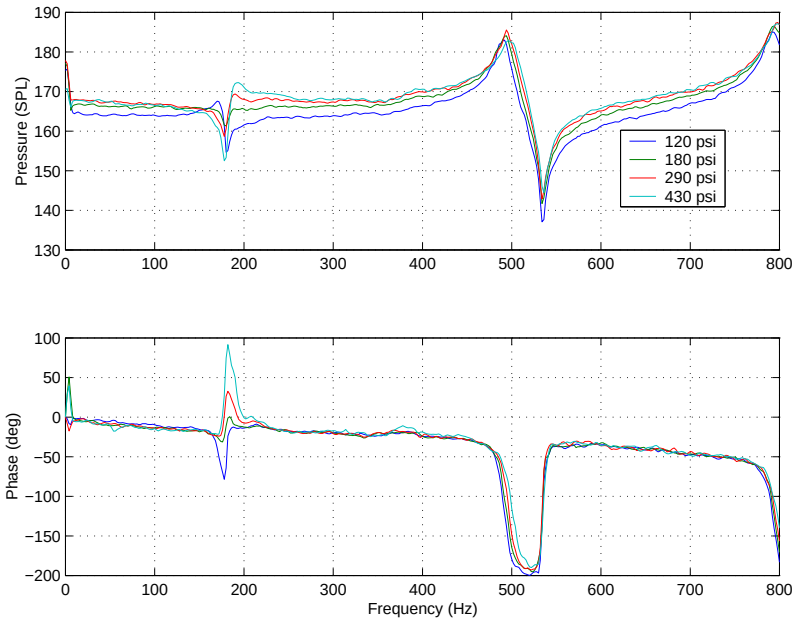

Figure 3.7: FRF of closed system driven by a piston at measurement location #2 at various mean pressures.

reference pressure of 1 μPa. The fact that the overall gain increases slightly and the low-frequency resonance shifts higher in frequency with increasing mean pressure is indicative of a pressure-dependent stiffness due to the compressed air.

As stated before, the bubble volume would found by iteratively comparing the model to the data at a certain pressure. This result of this was that the bubble volume matched well with the volumes consistently found using the time constant method, where a bubble volume of 0.4 cc was used. The only other uncertainty was the fact that the data amplitudes were still about 20 dB lower than those in the model. It was proposed that the reason for these losses were due to the actuator support brackets or piston stem strain, necessitating experimentation to be conducted to find the amount of displacement that was being lost. Displacement measurements were taken at the base of the stack at two static pressures: ambient and 200 psi. The displacement of the stack was then subtracted from the total displacement by measuring the stack's strain gage output. The results showed that the

bracket and stem deflected by about 150 microns, yielding a stiffness on the order of 10 N/μm, much lower than the stack's stiffness of 202 N/μm.

As with pipe losses, bracket deflection posed a problem with overall injector authority. Because the authority was reduced by more than 20 dB, or a factor of 10, compared with the complete-transmission cases in the models, the bracket assembly would have to be made more rigid. Referring to Figure 2.7, the bracket assembly consisted of one member at the base of the stack, two members along the top and bottom, and two clamping members supporting the piston. One alteration was to reduce the clamping members, which would require a few rough calculations. For a simply supported member of length L, elasticity E, and moment of inertia I with point loading, a stiffness of $48EI/L^3$ exists at the center of the member. By reducing the clamping member and the stack's base plate length by one-half, the deflection loss would ideally be reduced to $(1/2)^3$, or 1/8 of its original value. In addition, it was decided to make the top, bottom, and base plate brackets more rigid by using thicker members. The 3/8-inch brackets on the top and bottom were replaced with 1/2-inch members, while a 3/4-inch member replaced the 3/8-inch base plate.

The result of these alterations was an improvement in overall amplitude due to the higher stiffness of the new bracket assembly, as depicted in Figure 3.8. The results show a gain in amplitude between 10 and 13 dB overall. Based on static deflection, resulting in a known pressure change in a closed system, the new bracket stiffness was found to be 88 N/μm, still lower than the stack's stiffness, but an improvement nonetheless. Incorporating this stiffness into the model gave a much closer match to the data, as shown in Figure 3.9 (a) and (b). The pressure is slightly over-predicted at higher frequencies, apparently due to an un-modeled first order effect, which is also evident by the monotonic increase in phase lag.

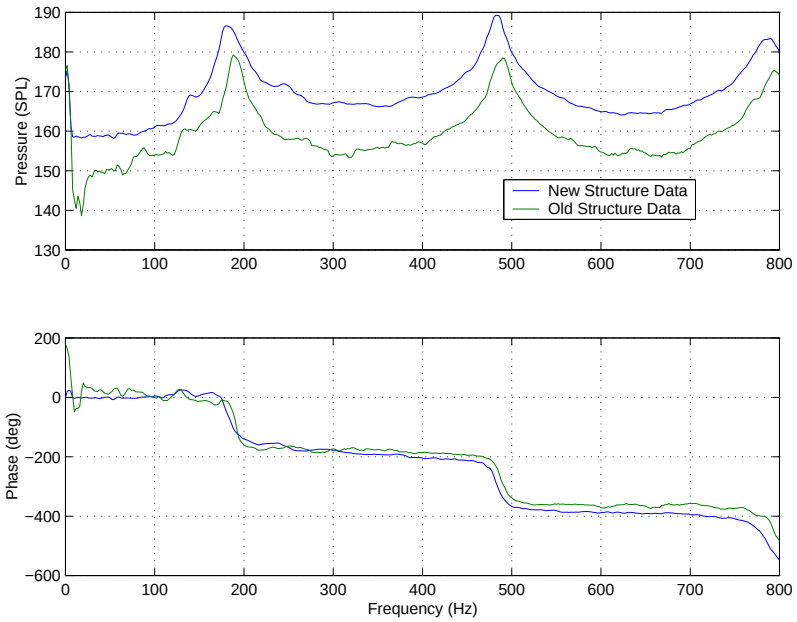

Figure 3.8: Comparison of FRFs at measurement location #5 with original and improved bracket assemblies at a mean pressure of 400 psi.

3.5.2 Orifice Plate Validation

The dynamic behavior of the system in the presence of flow was the next scenario to be treated. An orifice plate, placed in element 11, was the most logical choice for a boundary since the dynamics are well known through traditional models in several introductory acoustic texts, such as Pierce [34]. This orifice had a diameter of 1/32 inch and was installed in the piping by the threaded connection to the end adapter. A replacement for the check valve was also sought out by examining the effectiveness of a line constriction with a negligible pressure drop.

The orifice plate was characterized by a boundary with two impedances: one due to the mean flow rate and another due to formation of the fluid jet. A fluid jet is considered to have separated flow at the point where the fluid exits the orifice, where it experiences turbulent processes due to the shearing action of the air. If it is assumed that the jet

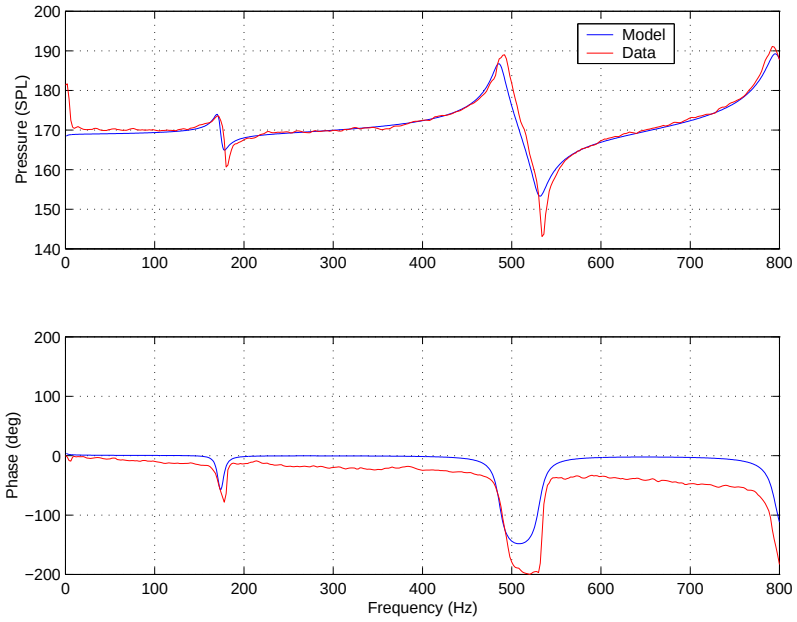

(a)

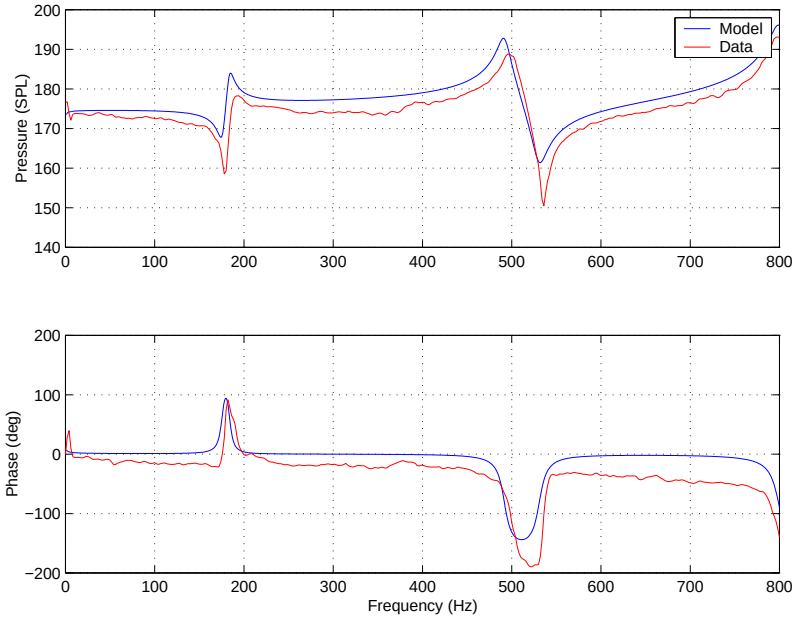

(b)

Figure 3.9: Models and data sets of closed tube at measurement location #2 at mean pressures of (a) 120 psi and (b) 430 psi.

does not reach a boundary before the onset of turbulence, the jet can be thought of as an energy dissipater, effectively a convective boundary. Investigators such as Bechert [4] made a similar argument, albeit from the standpoint of the jet and surroundings being of identical media. The jet element was thus modeled as a discrete area change of infinite length, or an impedance equal to the specific acoustic impedance ρc of the liquid. The mean flow resistance did not need to be modeled because the dissipative impedance is relatively large ($\rho c \ll Z_{f,orif}$).

The mean flow impedance through the upstream metering valve must be included in the model to determine the effect of a pressure gradient on the transmission loss. The impedance consists of a resistance that may be described by the nonlinear flow characteristics of the valve. These characteristics are often referenced by way of a flow coefficient, defined in terms of useful units:

$$C_v = \frac{Q}{(\triangle p/SG)^{1/2}} \tag{3.31}$$

Often this coefficient is based on empirical data provided by the manufacturer and is related to valve position. Linearization may be possible if small perturbation levels exist about some mean resistance value:

$$u_0^2 = (\bar{u} + u(t))^2 = \bar{u}^2 + 2\bar{u}u(t) + u^2(t) \tag{3.32}$$

where u_0 is the absolute particle velocity. To first order approximation, the last term is dropped before substituting into Equation 3.31. The first term represents an inertial end correction due to the acceleration of the fluid [31], often expressed as a characteristic length. In actuality, this end correction is small enough to ignore, resulting in a mean gradient impedance:

$$Z = \frac{2\bar{u}S_o^2}{C_v^2} = \frac{2\bar{Q}S_o}{C_v^2} \tag{3.33}$$

The existence of such an impedance has been proven experimentally by investigators such as Washio et al. [41], which is actually a sum of the turbulent and kinetic losses along with an inertial component. As expected, at high mean flow rates, the kinetic effects become small in comparison with the turbulent effects.

From Kinsler and Frey [24], the transmitted acoustic power across an orifice is given as:

$$T = \frac{4}{4 + \left(\frac{S_p}{S_o} - \frac{S_o}{S_p}\right)^2 \sin^2 kL_o} \tag{3.34}$$

where subscript p designates quantities associated with the pipe, and o designates those associated with the orifice. The equation represents the low-pass filter properties due to the inertance of the metering valve. Given the valve's dimensions, the corner frequency of the transmitted power can be found, which is the frequency at which losses to the upstream line become small.

Data collected from the test apparatus is revealed in Figure 3.10, again at location #2 to obtain nearly collocated FRFs. For the tests conducted here, the metering valve was set to a C_v of 0.0085, which induced a pressure drop of 4 psi at a flow rate of 1 gph. At this setting, Equation 3.34 yields a corner frequency of 40 Hz. For comparison, a closed tube case of the same length is shown on the plot. The low frequency content below 150 Hz is 30-Hz harmonic pump noise. Clearly, the system's modes are about the same in both cases, but the damping in the orifice case is much larger, which is expected with a semi-dissipative boundary. Also evident in the data, the metering valve was effective in impeding upstream-directed flow at low frequencies, even though the pressure drop across it was quite small.

In forming the models, the air content was iterated upon to match the experimental and model-generated FRFs at various mean pressures. The result of modeling this particular case is shown in Figure 3.11, where the same bubble volume that was used in modeling the closed tube, 0.4 cc, provided for the best match. From the plots, the stated assumptions regarding the orifice boundary and of the metering valve are validated. In particular, the jet model appeared to be correct, since the damping over the measured frequency range was similar to the data. The 4-psi pressure drop across the metering valve is too small to create a mean gradient impedance, therefore its inertance alone is responsible for lowering the transmission loss. Investigating the transmission loss further revealed that a 5 dB gain

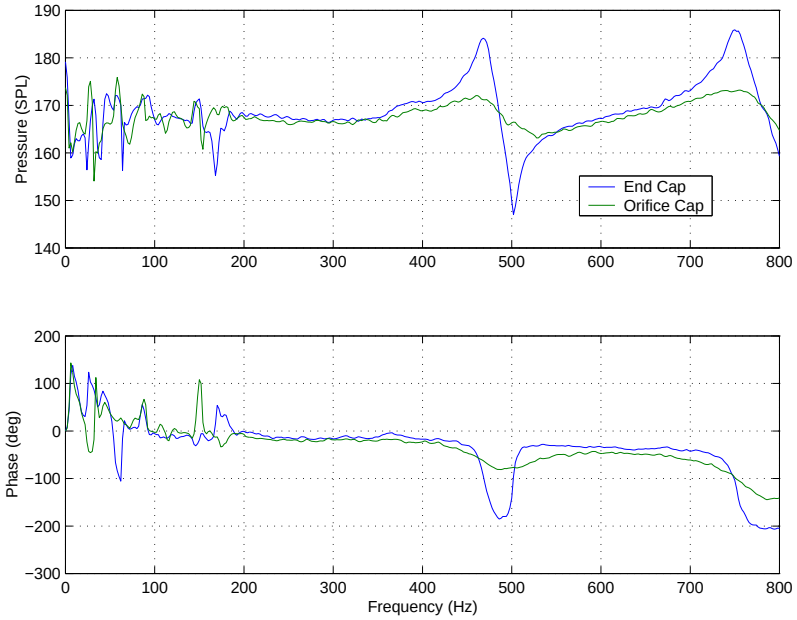

Figure 3.10: Comparison between data sets at measurement location #2 for end cap and orifice plate scenarios at a mean pressure of 230 psi.

in SPL resulted with the valve's orifice in place compared with a tube with no orifice, almost half of the incident sound pressure.

3.5.3 Atomizer Validation

The pressure-swirl, or simplex, atomizer was modeled using the same transmission line approach as the fluid delivery system: identifying the constrictions and expansions in the streamwise direction. The internal atomizer flow includes hydrodynamic effects that are highly complex, therefore the fluid behaves quite different than for the orifice plate. Typical simplex atomizers allow swirl to be imparted by way of several small channels that are directed tangentially into a swirl chamber. This swirl chamber is located directly before the orifice, and if the swirling liquid is moving at a sufficient velocity, the dynamic pressure inside the chamber is great enough to allow the total pressure to create a vacuum, drawing

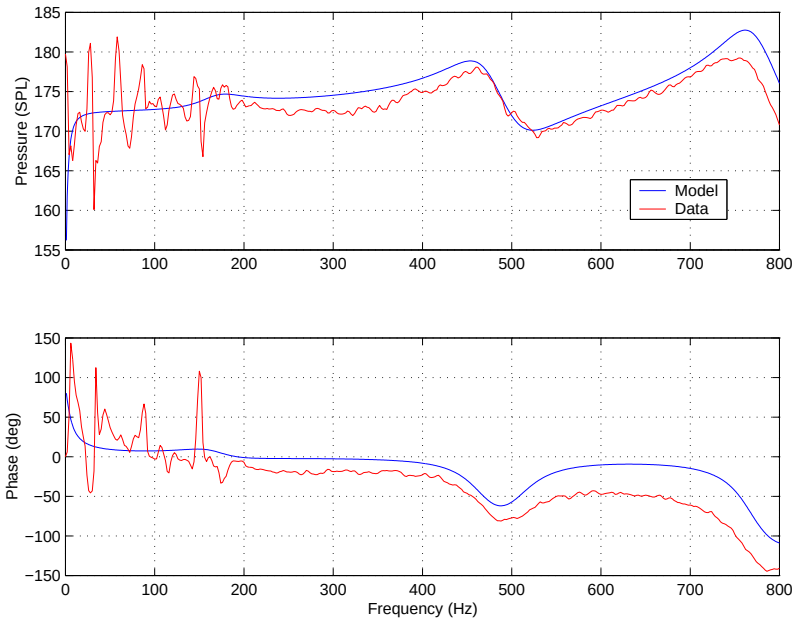

Figure 3.11: Models and data sets of orifice end condition driven by a piston at measurement location #2 at a mean pressure of 230 psi.

ambient air in with a swirling motion. An air core is generated, forcing the liquid to exit the orifice in a conical sheet. This axial component is created because the viscous effects at the walls allow sufficient energy loss so that the fluid cannot overcome the radial pressure gradient, thus moving towards the orifice as it moves towards the air core [27]. The sheet is subjected to turbulent effects, causing it to rapidly disintegrate into droplets. Figure 3.12 schematically shows the flow characteristics of a typical simplex atomizer.

It is necessary to know what dimensions are needed to model an atomizer acoustically. Lefebvre [27] has suggested that the thickness of the conical sheet plays a major factor in the breakup location and mean droplet sizes created by the atomizer. Researchers have developed an equation that takes into account viscous effects within the swirl chamber, showing a weak dependence on the supply pressure:

$$t^2 = 1560 \frac{FN\mu}{\rho_0 d_o \sqrt{\triangle p}} \frac{1+\alpha}{(1-\alpha)^2} \tag{3.35}$$

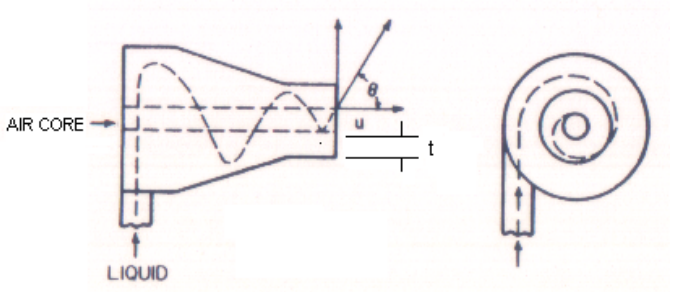

Figure 3.12: Illustration of the flow path through a simplex atomizer [27].

which is expressed in terms of the flow number as defined in Equation 2.1 and the area ratio of the film sheet to the air core a equal to $(d_o - 2t)^2/d_o^2$. With the assumption that $\frac{t}{d_o} \ll 1$, this implicit equation can be reduced to:

$$t = 2.7 \left(\frac{d_o F N \mu}{\rho_0 \sqrt{\triangle p}} \right)^{1/4} \tag{3.36}$$

The equation implies a weak dependence of the film thickness on supply pressure.

The formation of droplets is due to a shear layer instability mechanism that is basically a shedding of vortices at the edge of the orifice. Dombrowski and Johns [9] formulated an expression for the ligament diameter by applying conservation laws to the film sheet:

$$d_L = 2 \left(\frac{t}{k_{max}} \right)^{1/2} \tag{3.37}$$

where k_{max} is the wavenumber corresponding to the maximum growth rate of shear layer instabilities, usually on the order of several kilohertz. The droplet diameter can be estimated by an empirical formula developed by Lefebvre:

$$d = 1.89 d_L \tag{3.38}$$

High-frequency fuel pulsation is sometimes used to excite these instabilities to promote droplet breakup for finer atomization, performed by researchers such as Anderson, et al. [3].

The droplet breakup location is a contributor to the boundary that exists at the atomizer exit plane. Conical sheet breakup occurs rapidly if the supply pressure is high

enough to achieve an adequate air core area. If vorticity dissipation effects are ignored, the boundary type depends solely on if the breakup location is within much less than a wavelength from the atomizer exit. Because droplet formation is known to occur within a few millimeters of the orifice exit, $ka \ll 1$, and a discrete pressure release (pressure node) boundary may be used. Bechert [4] proved this simplified model to be valid over a low frequency range.

Because vorticity effects are by no means nonexistent, they may play a role in influencing the boundary condition. As is often seen in cases where sound is superimposed on flow through a nozzle, vorticity shedding occurs which has a strong influence on the transmission and dissipation on the incoming wave, as shown by Munt [32] and Howe [19]. In the studies done by Howe, it was shown that the sound absorption was an exclusive result of the fluctuating vorticity at the nozzle's edge, at which a Kutta condition exists. Because of this, a closed-form model of such effects is very complicated, and one may therefore conclude that the most reliable method is to determine the unsteady flow and far-field directivity patterns by way of post-atomizer diagnostics.

A transmission line model was created for the atomizer, in effort to include the dynamics of each of the serpentine passages upstream of the orifice. The area of the orifice section, element N6, was determined from the film thickness relationship, Equation 3.35. It should be noted that the model for this element is not truly correct, since the flow is separated because of the air core. This complete one-dimensional model is illustrated in Figure 3.13, along with an internal drawing of an atomizer. Namely, element N1 represents the expansion due to the coupler between the pipe and the atomizer, N2 the effective area of the porous sintered filter, and N3 the area expansion downstream of the filter. Further downstream, N4 represents the cumulative cross-sectional area of the four swirl channels, N5 the swirl chamber, and N6 the cylindrical liquid sheet within the orifice. Note that the schematic in Figure 3.12 is represented by elements N4 through N6.

Due to the large area changes within the atomizer, several junction impedances were

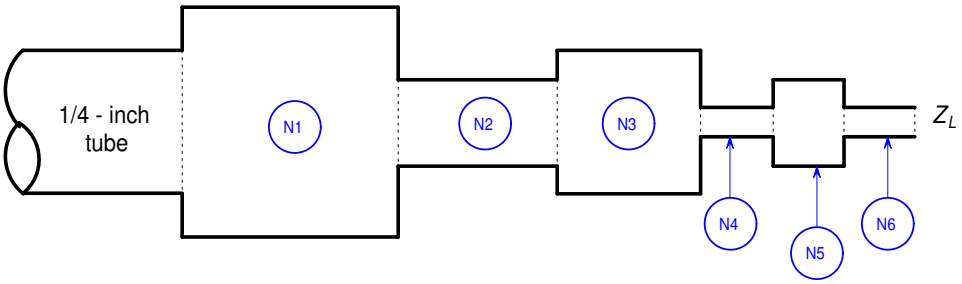

(a)

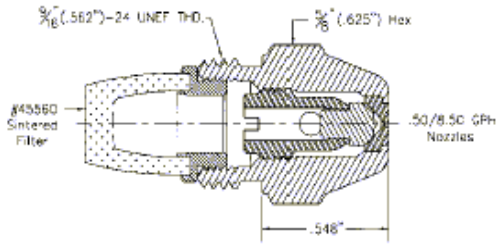

(b)

Figure 3.13: (a) Transmission line atomizer model (not to scale) and (b) internal features of a typical Delevan atomizer.

added to each constrictive element, which is simply an inertance associated with an orifice whose dimensions are much less than a wavelength. As the length and the ratio of the areas go to zero, the impedance becomes the imaginary part of the radiation impedance. Several derivations of junction impedance examples are found in Morse and Ingard [31] and Pierce [34], which reduce to the usable form:

$$Z_j = -j\omega \frac{8\rho}{3\pi^2 b}\left(1 - \frac{b}{a}\right) \tag{3.39}$$

where a and b are the radii of the circular channels with $b < a$. As with the orifice plate, the atomizer must have a resistance in order to justify the mean velocity due to the nozzle FN. The resistance is found in Equation 3.26, written in terms of the flow number instead of the flow coefficient. Neither the exact location of this impedance nor if it was a distributed effect was known, so models were generated for each of the probable locations of the impedance.

Based on these models, the tube pressure and the post-atomizer velocity responses showed that the location of the resistance is entirely arbitrary within the atomizer. This is because the relative scale of the atomizer dimensions to the acoustic wavelength is quite small.

When modeled, the resulting FRF at location #2 did not match up well with data taken with an operating pressure of 230 psi with the 1.0 atomizer, as shown in Figure 3.14 (a). In fact, the atomizer model appeared to produce the same result as with the orifice. Because the end impedances are much different for the two cases, one possessing an infinite condition with a relatively large orifice diameter, the other a pressure release condition with a much smaller orifice, the large area change is the dominating factor in determining the boundary type. Somewhat surprising is the existence of a low-frequency resonance in the data that does not correspond to any realizable modes of the system. Given the system's dimensions, the first quarter wave mode in the system would occur at 105 Hz and the first half-wave mode would occur at 211 Hz. It was thought that the existence of this 86-Hz peak was due to an un-modeled bulk mode, however there was no evidence based on simple Helmholtz calculations of such a mode to exist. The possibility of air content changing the system's bulk stiffness was next explored.

Based on rough Helmholtz calculations, a volume of approximately 0.6 cc of air would move the bulk mode of approximately 77 Hz. With this value entered into the model, the fundamental peak remained at 180 Hz. In the models developed thus far, air was assumed to occur locally only within the piston chamber, but with the addition of the atomizer, it is possible for air content to reside within the atomizer due to its serpentine passages. Unfortunately, only the total amount of air could be determined by practical experimental methods, so the local air content was again found by iteration on the model-generated FRFs. With two-fifths of the air content residing within the atomizer, the FRF resembled the data quite well as seen in Figure 3.14 (b) for a 230-psi mean pressure. The local air content is validated by the fact that models follow the data quite well with changes in mean pressure. At 150 psi, the fundamental peak moved to 68 Hz, while at 100 psi, it moved to 54 Hz.

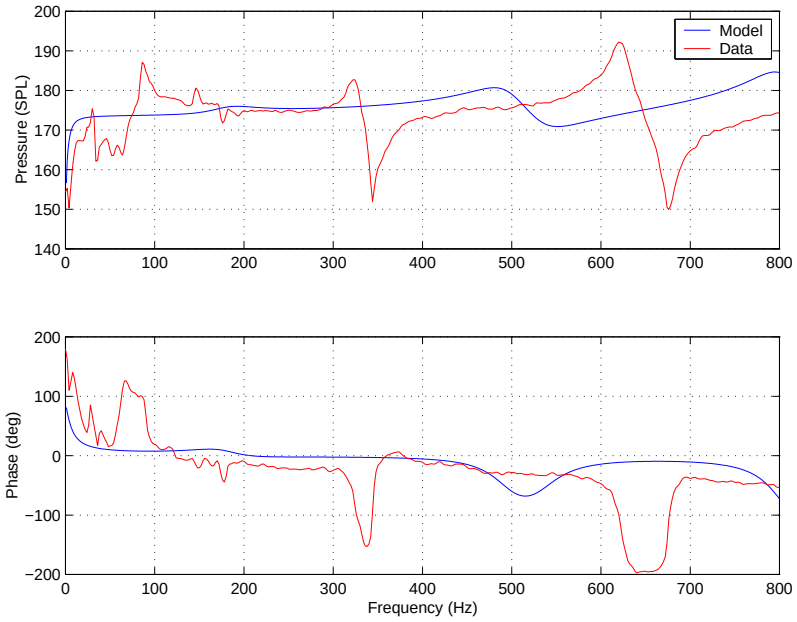

(a)

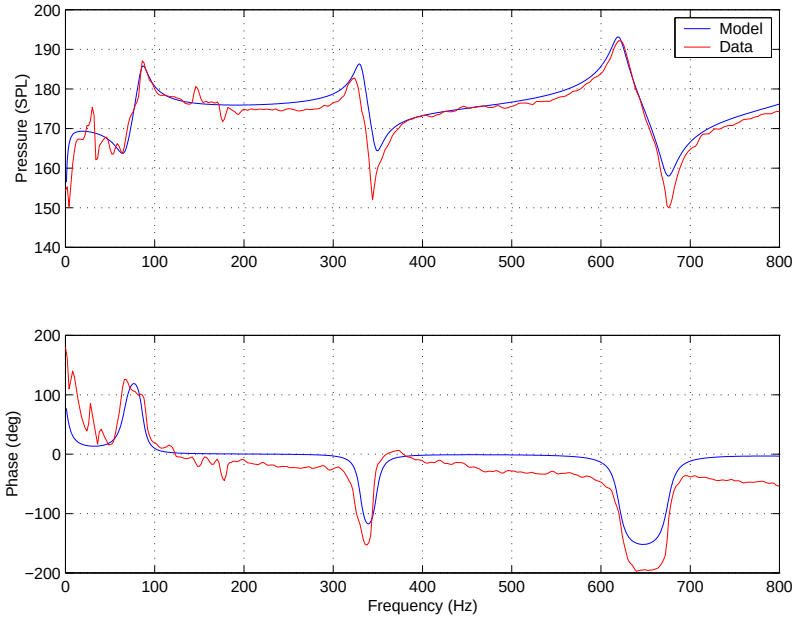

(b)

Figure 3.14: Models and data sets of piston-driven system with 1.0 atomizer boundary: (a) preliminary model and (b) corrected model at a mean pressure of 230 psi.

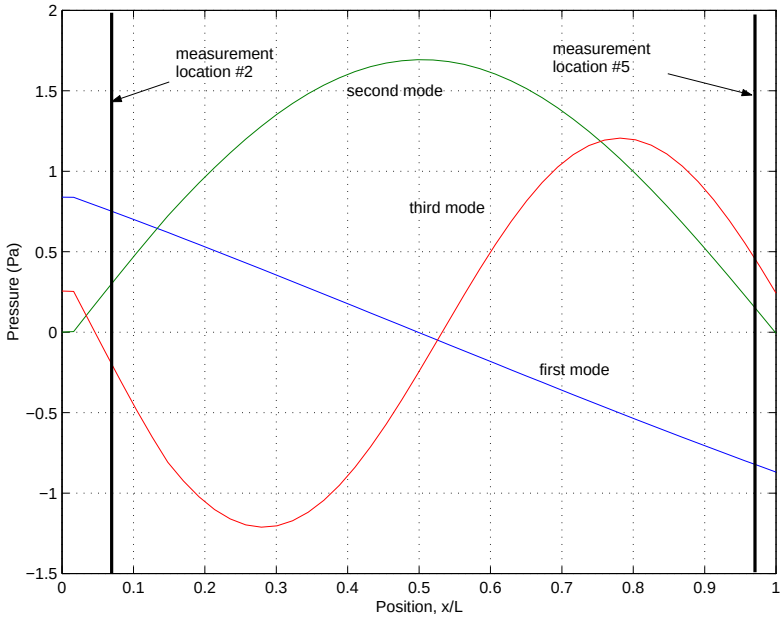

Figure 3.15: First three mode shapes of a piston driving a system with a 1.0 atomizer. Position $x = 0$ is the location of the piston driver, $x = L$ is the inlet to the atomizer.

The system's mode shapes are shown in Figure 3.15 for the first three resonant conditions. The locations of the two pressure taps in the fuel line are also shown for reference. The first mode is identified as a bulk mode, because the monotonic gradient produces a nearly constant velocity over the domain. The remaining modes represent half-waves set up within the tube, in contrast to the quarter-waves evident in the closed and orifice plate systems. This is because pressure nodes exist at both ends: one due to the piston's close resemblance to a velocity source and the other due to the low air bubble stiffness. The pressure release condition has little effect compared with the air content because the cross sectional area of the air content is much larger than that of the orifice. Because of Euler's equation, one can expect the acoustic velocity to be maximum at pressure nodes, located at the prime mover and atomizer locations. The accuracy of using the pressure gradient within the tube to determine atomizer velocity will be discussed next.

3.5.4 Acoustic Flow Estimation and Resonant Tuning

The ultimate flow amplitude at the orifice dictates the authority of the fuel injector, so the next step in the modeling process was to evaluate the post-atomizer flow response to the input voltage. In particular, the acoustic flow at the end of element N6 was modeled, corresponding to the atomizer orifice exit plane. In generating these FRFs, it was observed that significant changes to the exit plane impedance caused the post-atomizer flow response to vary greatly without being detected in the pressure upstream of the atomizer. Therefore, there is a greater sensitivity of the atomizer fluid jet impedance on the flow's response than the measurable response. The reason for this is that the atomizer's mean gradient impedance dominates certain characteristics of the pre-atomizer response.

To better understand the effect of the boundary condition assumption on the acoustic flow, a model was generated of the other extreme impedance case: an anechoic boundary, which would be the limiting case if vorticity effects completely dominated the flow. The results were compared to the other extreme case, a pressure release boundary, and plotted, as seen in Figure 3.16 (a) and (b). Figure 3.16 (a) shows the velocity normalized to input voltage and Figure 3.16 (b) shows the pressure FRF at location #5 with the measured response shown. These plots reveal that, while the tube pressure FRFs remain relatively similar for both cases, the broadband velocity amplitudes differ by about 40 dB. The result seems to follow intuition, since the pressure release boundary offers the best velocity transmission. The only evidence that points to the pressure release assumption is that the magnitude of the response at the first zero and pole in the pressure spectrum fits the data slightly better. Additionally, observations in experimental single-phase flow through an orifice [4] suggest that, in all but a few geometrical and driving frequency conditions, the flow experiences little attenuation due to vorticity. For the remainder of this study, exit plane velocity amplitudes will be based on a pressure release assumption, which is not completely certain without the aid of post-atomizer measurements such as laser Doppler velocimetry (LDV) or phase Doppler particle analysis (PDPA).

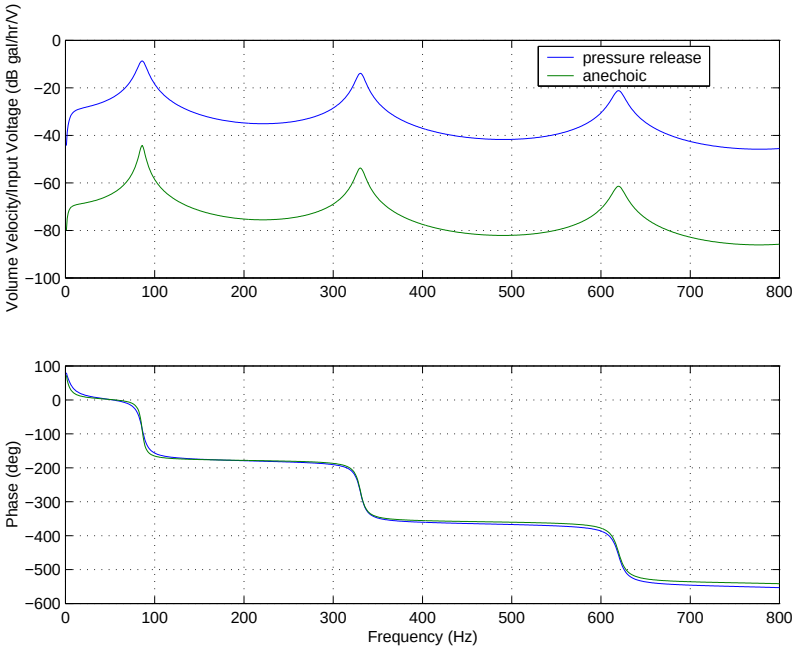

(a)

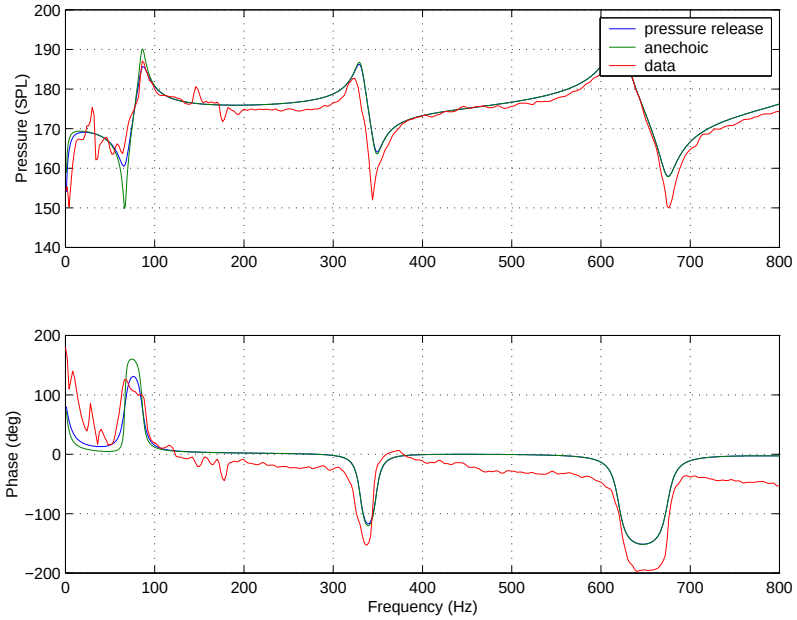

(b)

Figure 3.16: Comparison between two boundary cases at a mean pressure of 230 psi evaluated for (a) atomizer exit plane flow at measurement location #5 and (b) acoustic pressure at measurement location #2.

Figure 3.17 shows a comparison between the modeled normalized velocity to that predicted with commonly used measurement techniques for the same system as above. Evaluating the velocity based on the acoustic pressure at location #5 by the pressure release assumption, i.e. by invoking Equation 2.1, provides results that are valid at low frequencies but in error at high frequencies. This error results because the pressure difference across the mean gradient impedance location is not the same as the acoustic pressure within the tube. In particular, a zero exists in the pressure spectrum at 240 Hz, which is because of the measurement location. Also, the roll-off at high frequencies due to the low-pass effect of the atomizer is not captured in the pressure spectrum. A second commonly used method, known as the two-microphone technique, uses two narrowly spaced transducers to approximate the gradient, in which the velocity is calculated from Euler's Equation. If this technique is used to determine the velocity at location #5, the velocity it predicts is in error, as is shown in the figure. Obviously, the volume velocity near the end of the tube is not the same as that transmitted past the orifice.

Because in-tube acoustics produce erroneous exit plane velocities, the next step in the modeling process is to correlate model-generated velocities to those downstream of the atomizer. Using post-atomizer diagnostics, the correct exit plane impedance can be determined from both cold flow and reacting flow environments. These studies are outside the scope and time constraints of the present research, so it will be left to future VACCG efforts to focus on post-atomizer spray diagnostics. For the remainder of the thesis, the acoustic pressure will be assumed to be at a low enough frequency such that discrepancies in Figure 3.17 are negligible and thus Equation 2.1 can be used to determine the velocity.

The FRFs from Figure 3.17 show that steady-state fuel injector authority is maximum at the modes of the system. By changing the length of tubing between the injector and the combustor, the first mode may be tuned to the instability frequency. Of course, the repeatability of the modulation authority at a given frequency is dependent on adequate bleeding of the atomizer to a repeatable air content condition. A bubble volume of 0.5 cc was achieved on several occasions of testing, so it was the condition used henceforth. The

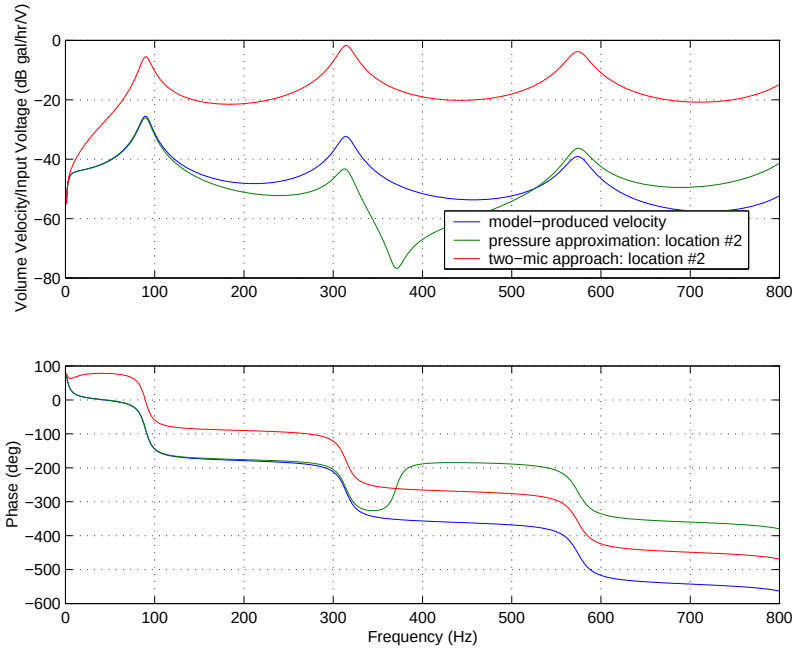

Figure 3.17: Transfer function representation of the atomizer's flow rate to the reference voltage with comparison between traditional measurement techniques for a pressure release boundary.

VACCG laboratory combustor's instability limit cycles at about 105 Hz, with about an 8 Hz deviation depending on the operating conditions. Adjustment of the density and sound speed for kerosene in the models showed that a total line length of 10' 1" between the piston and the atomizer is required.

3.6 Throttle Valve Models and Experimentation

Simply stated, the principle of operation of the throttle valve is that a change in orifice area allows a pressurized fluid system on the upstream side of the orifice to couple with the downstream side. When modulating, the orifice area changes proportionally, thus imparting a modulated pressure on the downstream side of the valve. For a sinusoidal input, this action

is effectively characterized by a monopole of certain strength on the downstream side of the valve. Moreover, since the valve's face has a significantly large area, its motion creates a velocity source on the fluid, somewhat similar to the piston source effect. In order to capture all of the dynamics involved with the valve, it would be necessary to create a two-dimensional finite difference model to account for the time dependence of the area. However, in order to maintain a stationary system, i.e. a system whose response does not vary nonlinearly with amplitude, the area must be assumed fixed about its mean position.

Based on the internal drawings of the throttle valve body and stem, shown in Figure 2.23, a transmission line model was formed as illustrated in Figure 3.18. Specifically, elements 2 and 9 represent the inlet and outlet valve chambers, respectively. The piston separating elements 6 and 7 represents the respective upstream and downstream sides of the valve face. Because the area is unequal on either side of the face, the respective upstream and downstream areas are represented by the diameters applied to elements 6 and 7. The lengths of these elements hold no geometric significance to the actual geometry, so they are both zero length. Element 8 represents the constant-area annular constriction around the valve face, or $S_8 = Px\cos\theta$, where P is the valve's perimeter, x is the offset provided by the stack, and θ is the trim angle, equal to 45 degrees for this design. For the no-flow case, this model for the valve would be necessary and sufficient to be entered into the model of the remaining upstream and downstream systems. For the following experiments the upstream length (element 1) was equal to 9 inches and a total downstream length (elements 12 and 15) of 11 feet was used.

The actuator used for these tests was the PSt1000/16/500 piezoelectric stack whose specifications are found in Table 2.7. The necessary dynamic parameters used in the model are presented in Table 3.2. The actuator's dynamics were included in the source representation based on a mechanical impedance term, which will be elaborated upon in the upcoming sections. As with the piston models, the amplifier dynamics were not modeled in the throttle valve system. Experimentation was first performed in a closed tube situation, then on the more complicated atomizer condition.

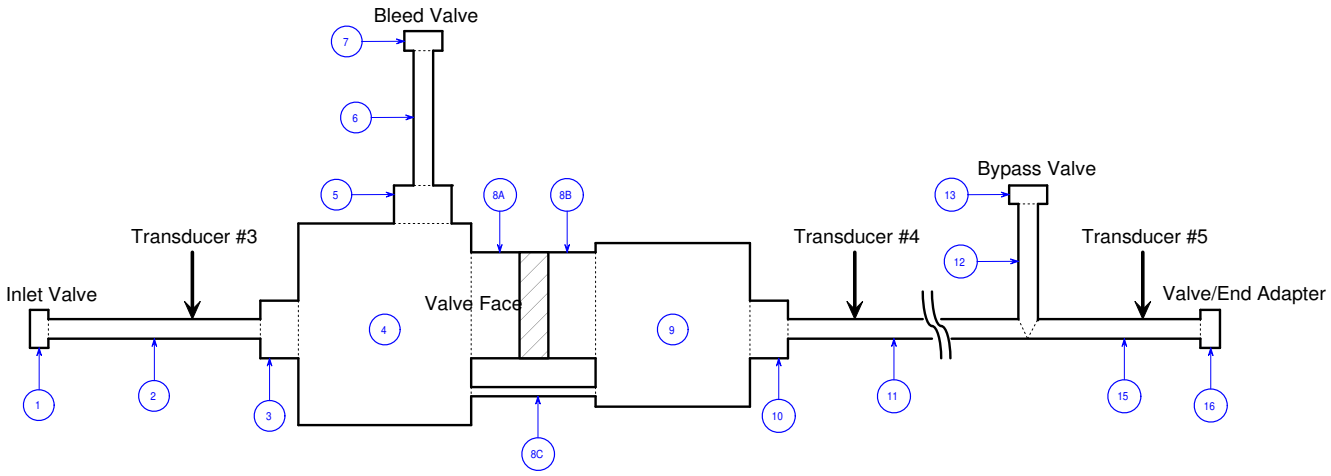

Figure 3.18: Transmission line model of throttle valve assembly with closed valves (not to scale).

Table 3.2: Dynamic parameters of the throttle valve system.

Stack Stiffness, k **(N/**μ**m)**	**Stack Effective Mass,** m **(g)**	**Amplifier Gain,** G_a **($\mathbf{V_{stack}/V_{in}}$)**	**Piezoelectric Constant,** G_p **($\mathbf{N/V_{stack}}$)**
17	149	200	8.5

3.6.1 Closed Tube Validation

This scenario allows for an easy assessment on the validity of the system's geometry as well as rapid identification of system losses, including those to the brackets. In addition to this, the source only includes the effect of the piston source without the modulating pressure gradient because there is zero mean flow. This provides an opportunity for the piston source to be isolated to ensure that it is correctly modeled. Also, the effect of the valve offset on the degree of coupling between the upstream and downstream systems may be examined.

The frequency response of the valve in the closed system is shown in Figure 3.19, conducted at a mean pressure of 350 psi. With a DC sensitivity of 0.5 microns/volt, the

range in offsets in the plot would be between 50 and 450 microns. Clearly, the response stays close to one another for small valve offset conditions, then deviates in magnitude and phase as the offset increases past 400 V, or 200 microns, whose steady-state value was approximated from the voltage supplied to the stack. Clearly, this offset is the point at which the upstream and downstream sections begin to couple acoustically. Since the stack voltage should be proportional to valve offset, it is possible that the junction impedance at that location becomes sufficiently large at 400 V and below to allow decoupling to occur. When the valve is nearly closed, the valve face can be thought of as a source acting on two separate systems: the fuel line upstream of the valve, and that downstream of the valve. As the valve is opened, the upstream system begins to interfere with the downstream system. Of course, the exact offset in which this coupling becomes significant is likely to be obscured by the impedance value at the valve face. However, one may identify when this coupling exists by observing when the phase of the FRF approaches 180 degrees with respect to the fully decoupled situation. This result is expected because the zero at the origin, representing the fact that an open valve cannot hold DC pressure, is eliminated.

To better understand the dynamics within both the upstream and downstream systems, the responses were modeled and compared to data taken at those locations. Frequency responses were examined at measurement location #3 upstream of the valve and at #4 downstream of the valve. Coupling due to a junction impedance was examined by entering it into the model. The results revealed that the system began to couple at a DC offset of about 100 microns, instead of the expected 300 microns. The hypothesis for this behavior was that the pre-load springs were set to a force high enough that the valve face remained on the seat until 400 V was reached. With this measure in place, the model produced results that were more true to the data, confirming that the springs were set to a pre-load force higher than expected, nearly 764 lbf.

Although the models exhibited the correct dynamics, the gain was about 32 dB lower than what was predicted. The brackets were not to blame, because the FRF would exhibit a second-order response superimposed on the acoustic response, which is not at all apparent

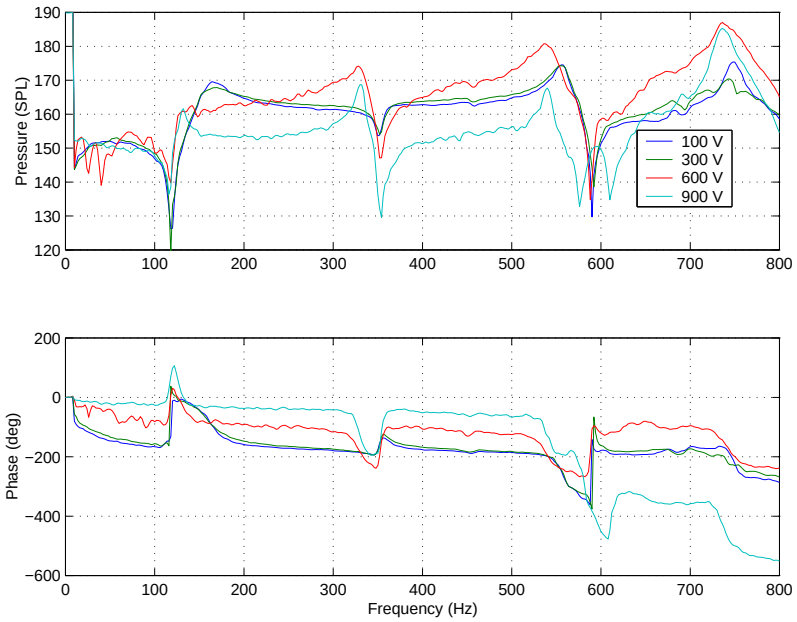

Figure 3.19: FRFs of throttle valve driving a closed tube at a mean pressure of 350 psi and various offset voltages.

in the data. It is well known that, in many acoustic dipole problems where a piston vibrates in an unbaffled wall, the radiative area is reduced somewhat to account for the loss in power at low frequencies [34]. In order to obtain the correct amplitudes, the valve area was reduced by 95%, a much larger reduction than one would think. Plots of the corrected model are shown in Figure 3.20 for the upstream and downstream measurements at two extremes in offset values. Clearly, the amplitudes match up well for DC biases of 500 V (50 microns) and 900 V (250 microns), but still are about 10 dB in error for the zero offset case. More than likely, this is because the stack cannot actuate with the pre-load stiffness keeping the valve on the seat. Also, note that this case is modeled with a 35-micron offset, which is probably due to the fact that the stem is not perfectly symmetric with respect to the seat.

The conclusion that can be made from this scenario indicate that especially at low valve offsets, the valve's clearance cannot be assumed to be constant for the closed tube case, so for high amplitude modulation, the system would be expected to be nonstationary and

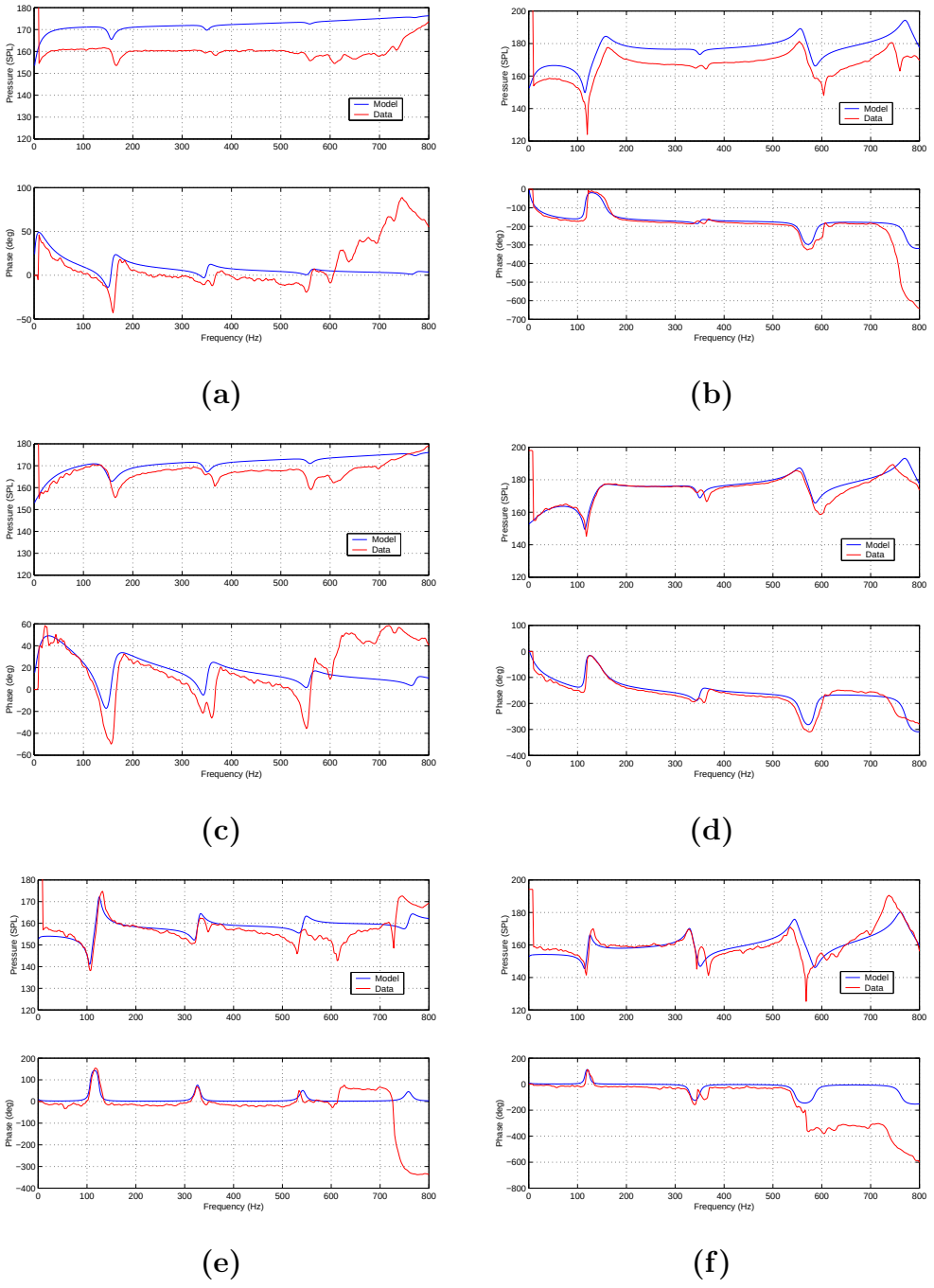

Figure 3.20: Models and data sets of valve driving a closed tube at offsets of 1 micron with measurements (a) upstream and (b) downstream; 50 microns with measurements (c) upstream and (d) downstream; and 250 microns and measurements (e) upstream and (f) downstream.

the models may fail. However, at 100 microns and above, the FRFs change very little with respect to mean offset. The throttle valve was used for primary modulation, which means that the valve's area will be modulated about a relatively large offset value, which would likely ensure a quasi-stationary system. Nevertheless, it is very likely that the presence of mean flow will create a different coupling scenario altogether because there will be a mean gradient impedance across the valve. These mean flow effects will be evaluated in the following section, along with the effect of the modulating pressure gradient source.

3.6.2 Atomizer Validation

Since the atomizer model development has already been performed in the piston validation experiments, the dynamics of that component will not be treated here per se. As was mentioned earlier, the flow scenario complicates the valve's behavior drastically because of the additional pressure gradient source and mean gradient impedance at the valve. Here, it was assumed that this pressure gradient acts as a piston, which oscillates about the mean pressure provided by the mean controller. An instantaneous opening of the valve results in a compression of the fluid immediately in front of the orifice, and an instantaneous closure results in rarefaction. The sensitivity of the displacement on the pressure is directly related to the upstream pressure and the valve's resistance. As such, the source strength goes to zero as the downstream impedance goes to infinity, as in the case with no mean flow.

The results from Section 2.7.2 showed that the pressure gradient source cannot be described by a transfer function due to the nonstationary system. However, in an attempt to explore how the bandlimited pressure gradient source affects the system's FRF, the step responses from Figure 2.28 were approximated with a first-order transfer function. The empirical transfer function relating pressure to the input voltage to the stack is as follows:

$$G(s) = \frac{15.3}{s + 0.5} \qquad [\text{psi}/\text{V}_{\text{ref}}] \tag{3.40}$$

with a corner frequency of 0.5 Hz. Of course, this only applies to a single condition, as

the data was taken with a 1.0 atomizer at a downstream pressure of 40 psi. The pressure monopole was located in the system immediately downstream of the orifice in element 9, with reference to Figure 3.18. To account for the fact the pressure gradient in the valve reaches its peak value one-quarter of a cycle before the peak velocity of the valve face, a phase lead of 90 degrees was imposed. The valve's mean flow coefficient allows formulation of the mean gradient impedance, which is appropriately placed at a location in the orifice upstream of the monopole source in element 8.

The result of the models with a 1.0 atomizer and an 11-foot downstream tube at 200 psi is shown in Figure 3.21 (a) at location #4. The resonances match up well, but there is some disagreement in the locations of several of the zeros, indicating some incorrectly modeled dynamics. The FRF taken at the pre-atomizer location, shown in Figure 3.21 (b), matches up with the data well at low frequencies. At high frequencies, zeros that are in the measured response are not apparent in the models. As the atomizer size increases, the damping in the modeled system increases if the mean pressure is held fixed because of the lower mean gradient impedance and greater orifice size. The experimental FRFs show that this damping trend exists in addition to an increase in broadband amplitudes, not captured in the models. One possible reason is that the hydrodynamic transient changes the corner frequency of the first order response, thereby increasing the source gain.

In order to reduce the response time and thus increase the high frequency gain, a bypass valve was inserted in the fuel line to increase the total downstream flow number, as outlined in Section 2.7.2. Adding this component to the model revealed that the FRF behaves the same as if the atomizer had the same flow number, damping the resonant peaks and increasing the overall gain as the orifice setting is increased. Figure 3.22 shows the effect of bypass setting (expressed in terms of number of turns open, with zero being fully closed) on the FRF of the pre-atomizer location. The plots reveal that, at best, a 7 dB increase in amplitude results from moving from three to 4-3/4 turns open. The damping mechanism of the bypass valve is also present, as shown in the reductions in each resonance relative to the trough values. Obviously, a higher bypass valve setting will provide better modulation, given

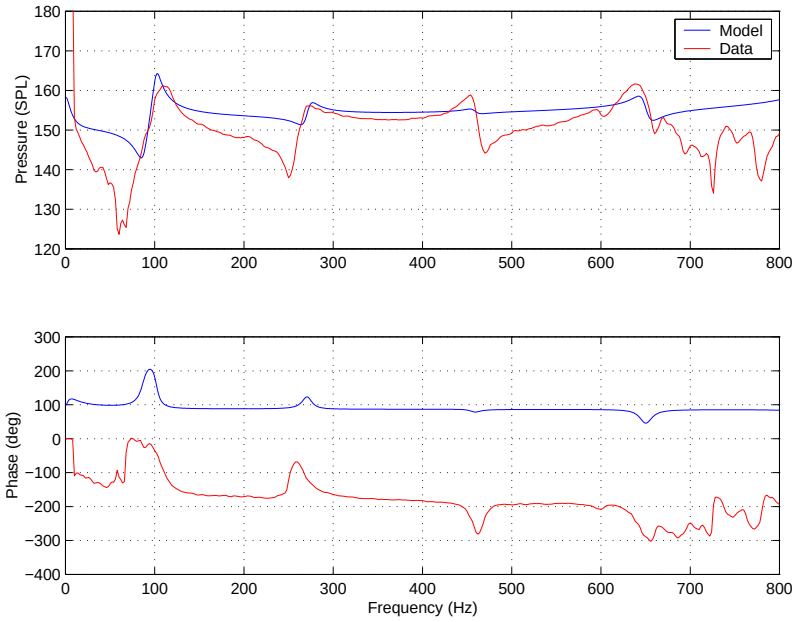

(a)

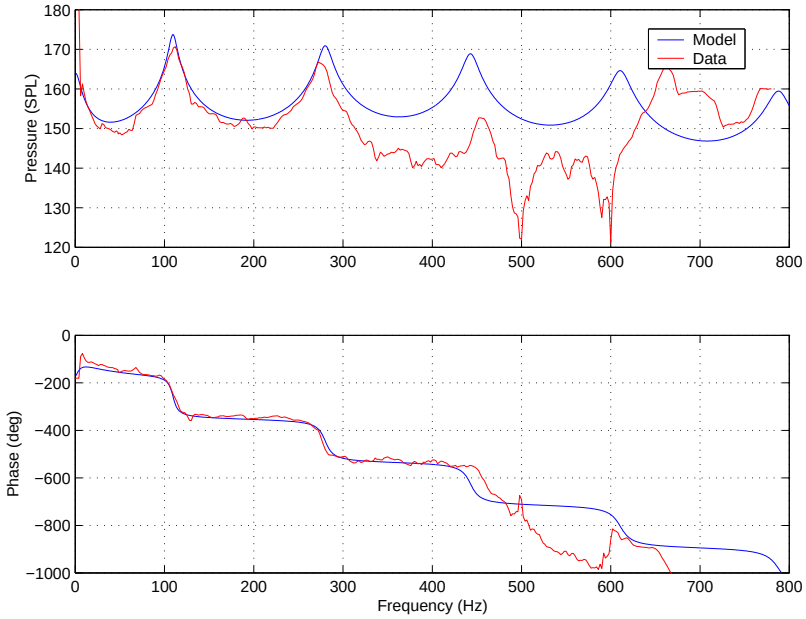

(b)

Figure 3.21: Models and data sets of valve system with a 1.0 atomizer at 100 psi at a) measurement location #4 and b) measurement location #5.

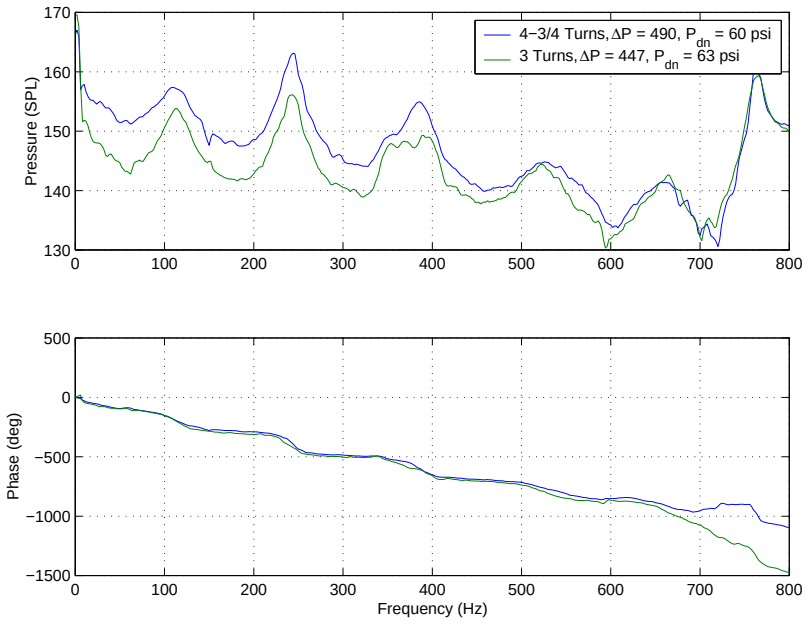

Figure 3.22: Comparison of FRFs with different bypass valve flow settings. Measurements taken at location #5.

the present laboratory combustor, however large-scale combustors will not need a bypass valve, since they are outfitted with large atomizers. Upon further exploration, the location of this valve apparently had little effect on the resulting FRFs, but care would be taken to place this valve at a consistent location as close to the combustor inlet as possible. Design strategies for the best bypass setting at certain conditions will be presented in Chapter 4.

Figure 3.23 contains the mode shapes of the valve system, which indicates dominantly quarter waves that move towards a half wave regime as the frequency increases. As the downstream flow number increases, half waves develop at lower frequencies. The delivery line length should be tuned to the instability frequency in order to maximize the achievable modulation energy at the atomizer. Coincidentally, the 11-foot downstream length used for these tests was appropriately tuned to the 105-Hz instability frequency with adjustment of the sound speed and density for kerosene.

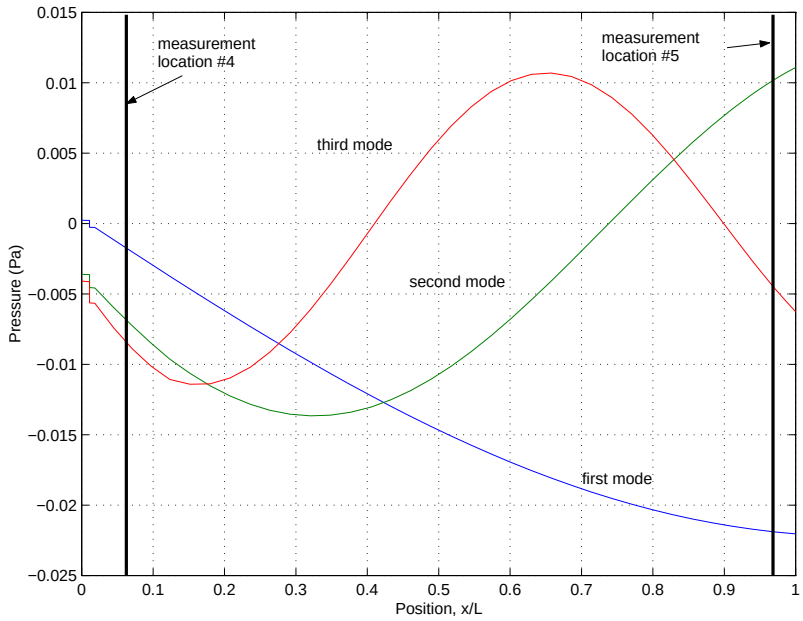

Figure 3.23: First three mode shapes of the valve system with a 1.0 atomizer and no bypass valve. Position $x = 0$ is the location of the valve stem and $x = L$ is the atomizer inlet.

Clearly, with the problems in correctly modeling the source effect with mean flow lead to erroneous FRFs at the nearly collocated measurement position. However, FRFs taken at the pre-atomizer location showed that the resonances were captured well. A decision on whether or not to pursue a correct source model is dependent on if the low-amplitude FRFs adequately describes the valve behavior at high amplitudes. The results of this will be performed in Chapter 4.

3.7 Chapter Summary

The development of these acoustic models is useful because it provides adequate tools in facilitating the design of new modulating fuel injection configurations. Identifying unwanted losses to the piping, brackets, and air compressibility allow designers to make appropriate changes to the system to improve authority. For the injector hardware used in the present

work, these design alterations included:

- Minimizing vibrations in sections of piping downstream of the prime mover assemblies by rigidly fixing the pipes.
- Strengthening the stack's base plate bracket assemblies to eliminate dissipation of actuator authority.
- Minimizing air content within the system, especially that within the atomizer in order to increase the overall gain of the system. Complete air elimination was not possible, however a repeatable trapped air volume was found, which enabled identification of the true authority for the two devices.

Identification of the above provisions will be helpful in the selection of future actuator and prime mover components, because they can be chosen optimally. To maximize the fuel modulation, the downstream line lengths were tuned to achieve a resonant condition at the 105-Hz instability frequency, which results in a 10- to 20-dB increase in acoustic response at best compared to the un-tuned system.

It was also shown that the modeled flow rate through the atomizer is significantly affected by the boundary condition assumed at the orifice. Namely, the pressure release assumption demonstrates amplitudes that are 40 dB higher than for a theoretically anechoic boundary. Thus, validation experiments with spray diagnostics downstream of the atomizer are necessary in order to gain the actual exit plane impedance and thus correlation of the output of the models to the expected fuel injector system authority. Even if the boundary is known, pressure measurements taken near the atomizer may lead to an erroneous velocity prediction at high frequencies due to, among other things, the low-pass nature of the atomizer. In order to ensure an accurate velocity response at the frequency of interest, fuel injector system models are a necessity.

To investigate the fidelity of the models to predict authority at actual working conditions, the present models were validated at a variety of operating conditions, as will be

discussed in Chapter 4. It will also be shown that understanding this authority will be important in identifying limitations in achieving combustion control.

Chapter 4

A Study on Fuel Injector Control Authority

The goal of this chapter was to study the performance of the piston and throttle valve fuel injection systems with respect to their ability to control an unstable thermoacoustic system. Investigating the pre-atomizer flow rates of the two fuel injection devices over a variety of operating conditions allowed the authority of the systems to be benchmarked. Because dissipative processes downstream of the atomizer inevitably cause fuel pulse attenuation, it will be shown that these benchmarks were useful in qualitatively assessing the results of combustion control experiments. It is hoped that the outcomes of this study would be useful as a basis for future active combustion control efforts to examine specific dissipative effects that will lead to a better understanding of fuel injector authority in a variety of combustion platforms.

This chapter begins with an overview of the VACCG laboratory combustor, including its physical specifications and a characterization of the thermoacoustic instability. This is followed by comparisons between low- and high-amplitude open-loop experiments on the fuel modulation systems, with analogy to the acoustic models developed for each system. The

results of combustion control experiments will then be presented, as will a discussion on the physical mechanisms that underlie attenuation of the fuel flow rate.

4.1 Atomization Remarks

In order to identify the specific fuel injector's ability to modulate heat release, it is necessary to observe the performance in a thermoacoustically-unstable test combustor. Because combustor plants are highly complex, influenced by a number of variables, it is not possible to describe ACC authority in a general context. Even in the context of a single combustor, the plant's characteristics are non-stationary due to the ever-changing operating conditions. Thus, the authority of the present fuel injection systems will be discussed in the form of achievable flow modulation. The specific ACC authority of the fuel injector hardware will be limited in scope to the VACCG laboratory combustor in hopes of assessing how combustor chamber processes affect the fuel pulse.

As was briefly described in Section 3.5.3, atomization and turbulent dynamics are a cause for attenuation of the fuel pulse. An atomizing spray can be described as a stochastic process in which droplet sizes are normally distributed about some mean value in time and in space. Based on the simplified d-square law of droplet burning rate, the vaporization time is a function of droplet diameter and air velocity in accordance with the following equation:

$$\tau_{vap} = \frac{d_i^2 C_{p,g} \rho_l}{8 \lambda_g \ln(1+B)} \tag{4.1}$$

where B is a constant containing fluid properties. The vaporization time τ_{vap} is proportional to the square of the initial droplet diameter d_i and inversely proportional to the thermal conductivity of the gas λ_g. It is clear that temporally- and spatially-distributed droplet sizes would be attenuated between the atomizer and the combustion region because the burning rate is also distributed.

Another factor in pulse attenuation is due to turbulent swirling and recirculation of

the hot gases. In particular, small droplets have a rather large proclivity to being affected by vortical structures and are largely undesirable for control, while those that are large are characterized by a wider distribution and convect further downstream before being fully vaporized. Yu et al. [42] suggested a dimensionless parameter for the characteristics of droplets amenable for combustion control. The Stokes number St, which is the ratio of the time scale of particle interaction with flow to the time scale of the flow dynamics, needs to be close to unity to achieve an optimal balance between distribution effects and turbulence. This theory holds true, however, only if the fuel delivery line remains unaffected by the atomization processes, which is likely not the case based on the acoustic analysis presented thus far.

The acoustics of the combustion chamber may also have an effect on the fuel delivery. For example, an interaction between droplets and the oscillatory acoustic field may work against the modulated flow. It has been suggested by Heister et al. [16, 38] that transverse and longitudinal waves have a significant effect on the liquid jet issuing from the injector. At high frequencies that are common in screech instabilities, the natural frequencies of the fluid jet are excited. However, the change in specific acoustic impedance ρc between the liquid fuel and the chamber gases as well as the mean gradient impedance will act to discourage coupling between the chamber processes and the fuel delivery system.

4.2 Combustor Specifications and Characterization

Necessary to the implementation of any novel active control scheme is an understanding of the plant in which the control scheme will be validated. In order to map the fuel injections in the future, it is necessary to know the exact specifications of the present combustor rig. The liquid-fuel, turbulent VACCG laboratory combustor for which the two fuel injection systems were designed was, at the time of this work, in a transitional state to becoming a higher power, pressurized LDI test rig. Several specifications of this configuration are shown

Table 4.1: Specifications of the VACCG laboratory combustor.

Criterion	Unit
Working Fuel	Kerosene
Chimney Length	48 in
Chimney Diameter	8 in
Max Air Flow Rate	70 scfm
Max Fuel Flow Rate	2 gph
Max Thermal Power	40 kW
Atomizer Flow Numbers	0.4 - 2 in^2
Air Swirl Vane Angles	30, 45, & 60 degrees

in Table 4.1.

At the time of this work, the combustor's configuration consisted of a multi-view port combustion chamber to allow for visual assessment of the flame, which would eventually be used for laser diagnostics. A 48-inch chimney was used to allow longitudinal modes to be set up in the chamber. Air swirl vanes were implemented to stabilize the flame at higher flows. The rig was outfitted with a SenSym SX01 diaphragm pressure transducer, with a range up to 1 psi, at the midpoint of the chimney to gather instability spectra. On the air side, a 100 psi compressor unit supplied outside air to the experiment, which had a maximum flow capability of about 70 scfm. An Eldridge Products mass flow meter was used to measure the flow to the combustor, whose D/A processing was performed by a National Instruments card on a dedicated LABVIEW computer. Flow was adjusted manually by way of a metering valve on the combustor control panel. Figure 4.1 shows a photo of the VACCG laboratory rig.

The fuel supply line was as shown in Figure 3.1. A pressure tap could not be installed at location #5 due to proximity to the air flow, so the taps downstream of the fuel injectors were used. Pump #1 was the Suntec gear pump and pump #2 was the HydraCell piston pump used in the water test bay, both of which were supplied by a 20-gallon fuel tank. Two

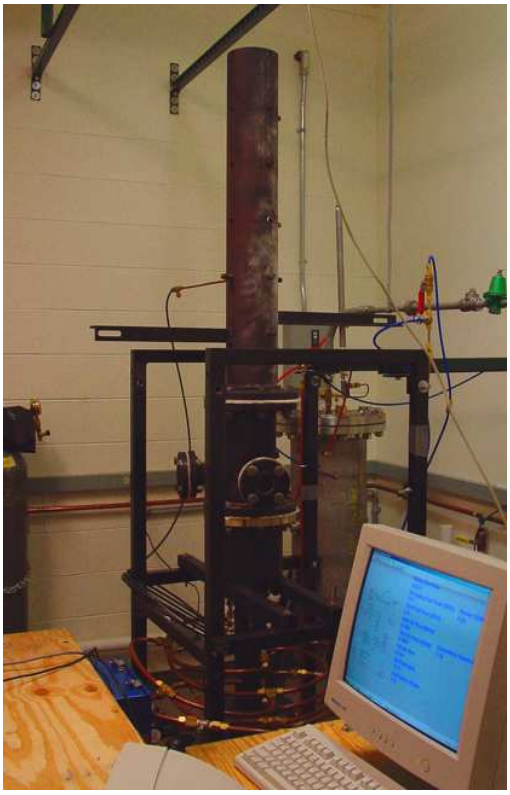

Figure 4.1: Photo of VACCG laboratory combustor setup.

gear-type flow meters were placed in the two supply lines to monitor the mean flow entering the combustor and to assess the flow characteristics of the fuel nozzle over time. The fuel flow was monitored on the LABVIEW GUI, which also calculated the air/fuel and equivalence ratios.

In previous VACCG work, the combustor was only capable of a limited supply pressure and the working fuel was ethanol. For example, in Lagimoniere [25], the resulting instability spectrum resembled that of a lightly damped, stable system as described by the author. It was hypothesized that the combustor's power was not great enough to drive the system unstable. The lower heating value of kerosene is roughly double that of ethanol, so the additional power would generate enough energy to drive the thermoacoustic poles toward the unstable region. In order to drive the system toward an unstable regime, the heat release

must be increased, requiring higher flow rates or a greater heat release density.

Figure 4.2 shows the instability spectrum present at various thermal powers taken in December 2001. One indicator with which one may conclude that limit cycle behavior exists would be if strong harmonic content exists. Clearly, as the thermal power increases, the broadband energy, harmonic content, and instability amplitudes tend to increase as well. In particular, between 9.1 kW and 22 kW, the fundamental peak increases in amplitude by nearly 22 dB. It is suggested that quarter-wave modes exist within the tube because of the strong odd harmonic content, although Eisenhower [11] showed that an asymmetric nonlinearity may also cause this effect. At thermal powers of 15.4 kW and greater, even harmonic content begins to show up, possibly a result of limit cycle behavior. At this transition point, it was observed that the lean, blue flame changes to one that is more yellow and diffuse. Further evidence of the existence of a limit cycle is the time trace of the instability, which has an amplitude that is relatively constant over time as shown in Figure 4.3. A system that is dominantly a result of combustion noise, i.e. no thermoacoustic feedback, would be characterized by random fluctuations in the amplitude over time.

The combustor was not expected to behave as a closed-open tube and set up quarter-wave modes within the tube. The area changes within the tube are not enough to cause the inlet side to be truly "closed". However, the flame sits at the bottom of the tube, which may impose enough acoustic impedance to make the inlet end acoustically closed. Along with the area change, the impedance may be a result of a combination of effects: a steep temperature gradient, the unburned fuel, and the combustion products. In the coming sections, the baseline spectral characteristics of the unstable plant will be important in assessing the authority of the ACC systems.

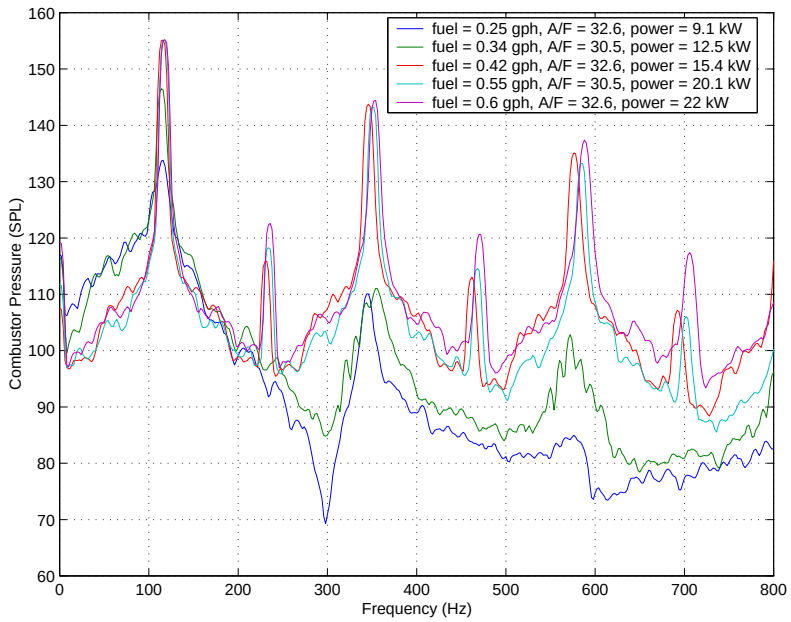

Figure 4.2: Instability spectrum at various thermal powers taken in December 2001.

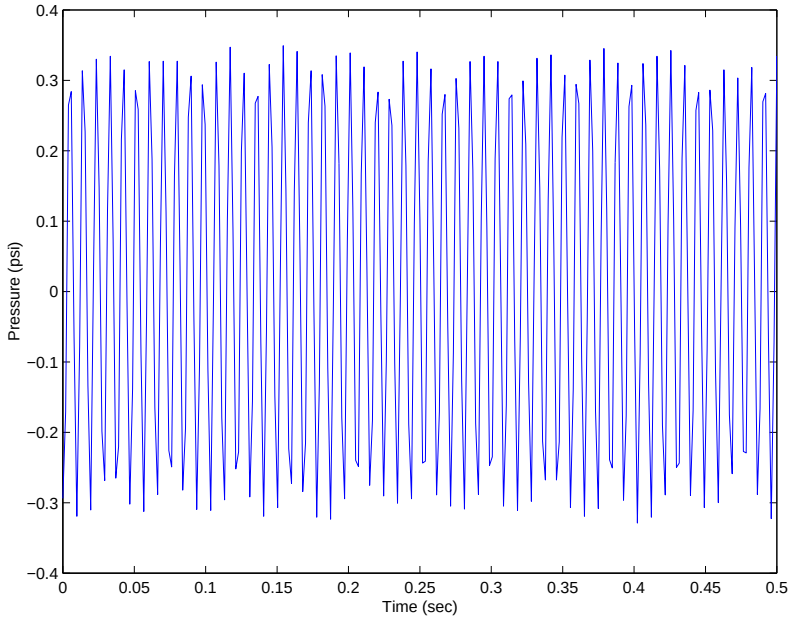

Figure 4.3: Time trace of unstable combustor.

4.3 High-Amplitude Mapping of Fuel Injector Performance

Acoustic characterization of the piston and throttle valve fuel injector devices in Chapter 3 was exclusively performed on a small-scale basis in order to maintain quasi-linearity. However, acoustic assumptions that have aided in validating the models, such as constant density and linearized atomizer flow number, are no longer valid at pressure amplitudes greater than a few percent of the mean. Additionally, air compressibility acts as a nonlinear stiffness, which was expected to cause further discrepancies between models and data at high forcing amplitudes. This section presents the work done to characterize the authority of the two devices across a variety of operating conditions and compare the results to the quasi-linear authority.

The experimental setup for the remainder of this research work was identical to that described in Section 3.1, but with kerosene as the working fluid. Since the fuel delivery line lengths were tuned to the 105-Hz limit cycle frequency of the VACCG combustor, authority assessment was limited to that particular frequency. It should be noted that the flow modulation levels presented herein were estimated based on the pressure release exit plane boundary assumption. The theoretical velocity was determined from the pressure tap immediately upstream of the atomizer. According to the observations from Section 3.5.4, this procedure is valid if the 105-Hz driving frequency is assumed to be sufficiently lower than the atomizer's low-pass corner frequency.

4.3.1 Characterization of Piston Device

The low-amplitude authority of the piston device was mapped at various atomizer flow numbers and mean pressure settings. Three atomizer sizes were tested: a 0.5, a 1.5, and a 3.0, corresponding to flow numbers of 0.32, 0.96, and 1.93 $\mathrm{lb/hr/\sqrt{psi}}$. With each atomizer

the inlet pressure was varied between 50 and 300 psi in 50-psi increments and FRFs were taken at the transducer location #5. The reference forcing amplitude was 0.125 V, or about 0.5 microns. Results at 50 and 300 psi for the 0.5 and 3.0 atomizers are shown in Figure 4.4. It is clear that, as the mean pressure is increased, the response increases in amplitude for both cases and the first resonance increases in frequency. This is due to the fact that the air content stiffens with the mean pressure. The resonance moves from about 103 psi at 50 psi and to 118 Hz at 300 psi, which is slightly above the 105 Hz target from the tuning, because the air content has varied between the present and the previous experiments used to tune the line. It is apparent from the figure that the models' ability to predict the system gain was more problematic at low-pressures, especially with the larger atomizer, possibly due to an over-estimation of the nozzle's resistance at the low pressures.

Figure 4.5 (a) shows the theoretical flow rate normalized to reference voltage predicted by the models, along with data points at 50 and 300 psi. As expected from Figure 4.4 (d), the models had indeed over-predicted the flow rates at several low-pressure, high-flow number conditions. However, the high-pressure cases for each atomizer condition agreed well with the models. The downward trend in amplitude with mean pressure seen in the figure is a result of the resonant peak moving to frequencies higher than 105 Hz due to compressibility. As the atomizer flow number increases, it is observed that the amplitude increases because more flow may be transmitted as resistance decreases. Figure 4.5 (b) shows the same data and models presented as percent modulation extrapolated to full-scale (10-micron) forcing amplitude. At high pressures and flow numbers, the percent modulation remains flat with respect to flow number, reaching a minimum value of about 14% modulation. To theoretically achieve 40% modulation at these settings, the required amplitude must be increased to 29 microns. However, this requirement would definitely decrease if the fuel line were tuned to better match the 105-Hz peak at those mean pressures.

The response of the piston device to a pure-tone input was obtained at several forcing amplitudes up to full scale (10 microns) to examine the nonlinear character of the system. Time domain plots of the pressure are shown in Figure 4.6 (a) and (b) for two different

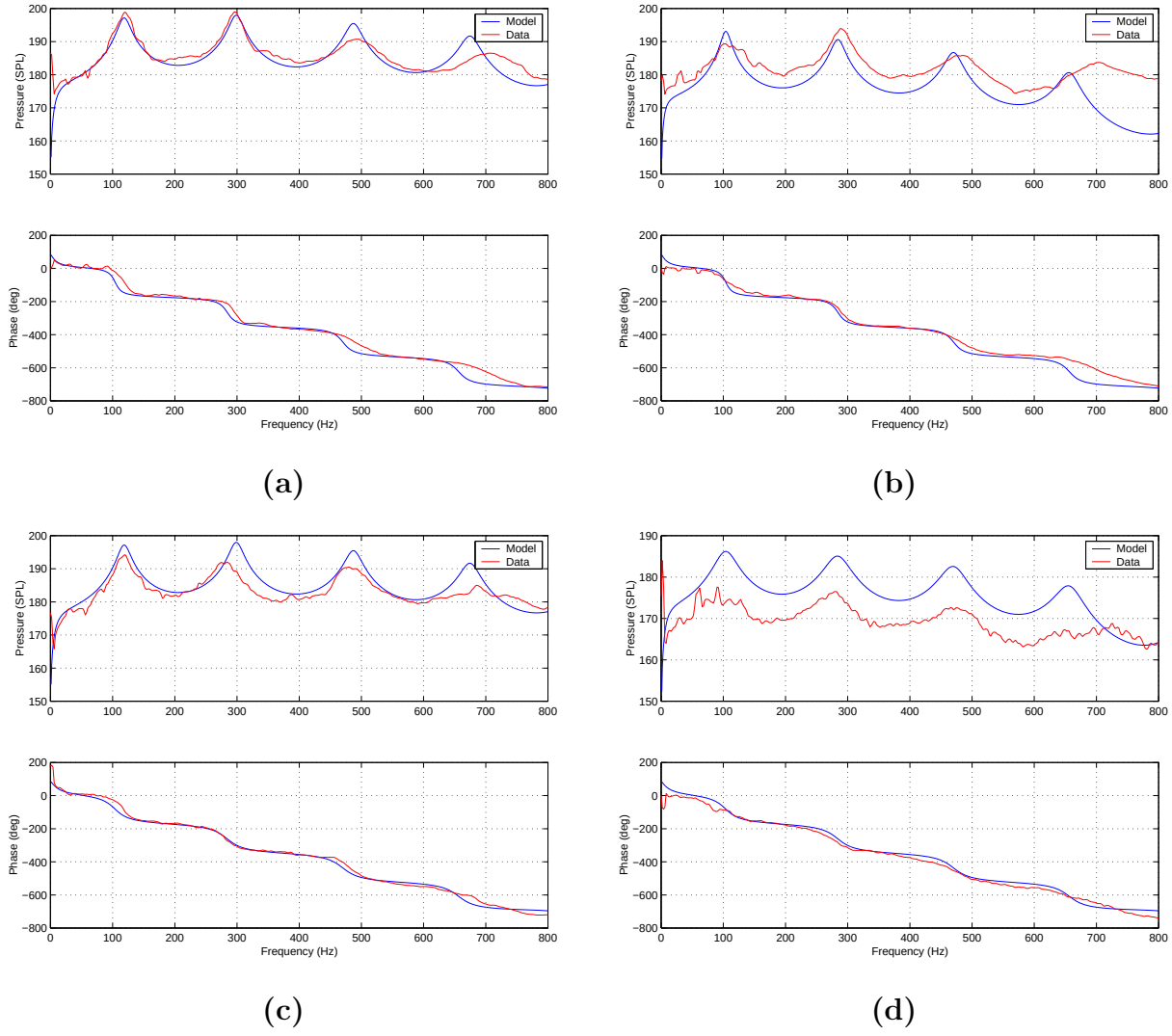

Figure 4.4: Comparison of piston-generated FRFs at measurement location #5 at four operating conditions: (a) 0.5 atomizer at 300 psi, (b) 0.5 atomizer at 50 psi, (c) 3.0 atomizer at 300 psi, and (d) 3.0 atomizer at 50 psi.

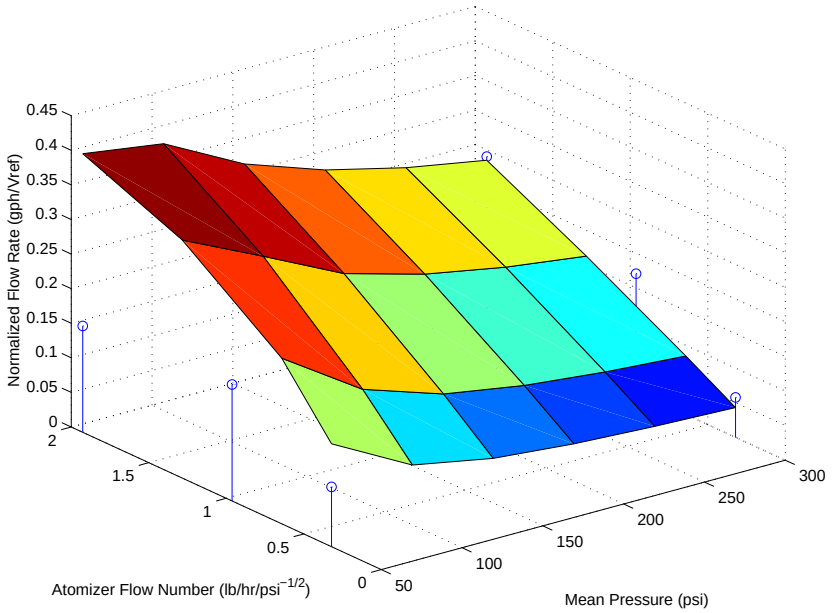

(a)

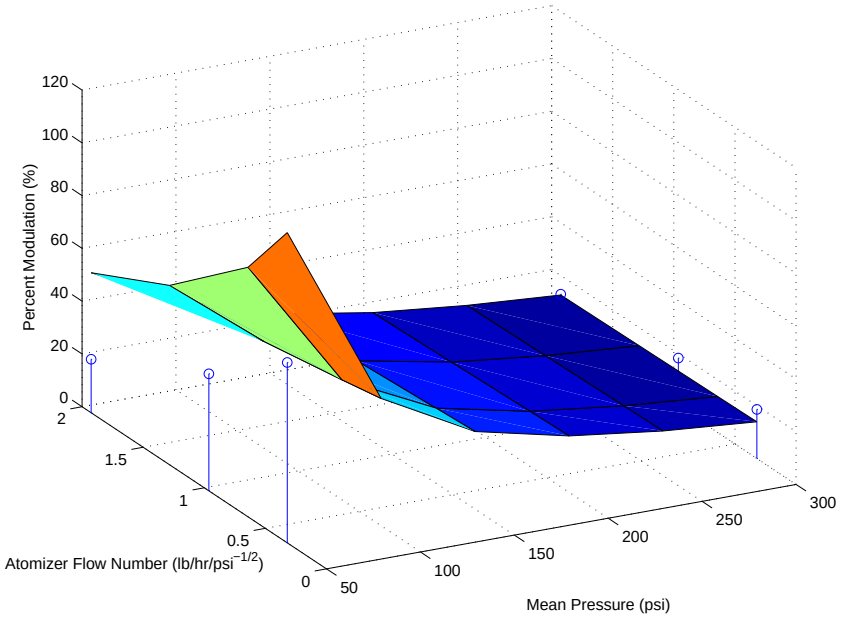

(b)

Figure 4.5: (a) Normalized flow rate and (b) percent modulation predicted by models and compared with FRF data at a forcing amplitude of 0.5 microns. Model results are shown as the surface plot and experimental data is shown as blue stems.

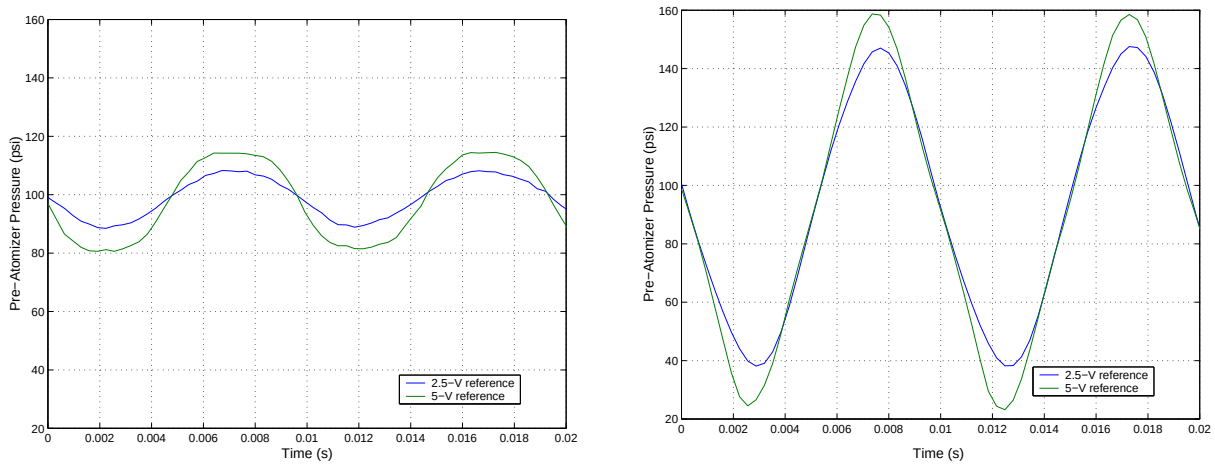

Figure 4.6: Pressure time trace of piston device forcing a 105-Hz sine wave at 5 and 10 microns for (a) 3.0 atomizer and (b) 0.5 atomizer.

source amplitudes and atomizers, both at a mean pressure of 100 psi. These plots show that the pressure waveforms are nonlinear, especially that of the 0.5 atomizer. Examining the linear spectra of the waveforms revealed strong harmonic content, which is due to modal amplification of the harmonics that result from the system's nonlinear nature. With reference to Figure 4.4, the second acoustic resonance is larger for the 0.5 atomizer than for the 3.0 atomizer, which is a likely cause of the amplification of that harmonic. Because the fundamental peak is in fact proportional to the input amplitude, the piston models are likely to scale with minimal error.

The response of the fundamental frequency obtained from linear spectra for each operating condition was plotted against atomizer flow number and mean pressure at full-scale modulation. The 105-Hz responses are presented in terms of normalized volume velocity perturbation and percent modulation, and are shown in Figure 4.7 (a) and (b). The errors between the experimental linear percent modulation from Figure 4.5 (b) and the actual percent modulation from Figure 4.7 (b) are shown in Table 4.2 at the four extremes in operating conditions. When compared with the low-amplitude cases, the scaled results show

Table 4.2: Error between percent modulations based on measured, quasi-linear data and data at 10 microns at four piston device operating conditions.

Mean Pressure (psi)	**Flow Number (lb/hr/$\sqrt{\text{psi}}$)**	**Linear** PM **(%)**	**Actual** PM **(%)**	**Error Between Linear and Actual** PM **(%)**
50	0.32	68.36	52.4	23
	1.9	20.25	9.21	55
300	0.32	18.6	17.56	5.9
	1.9	12.91	13.85	−6.8

good agreement for all but the high-flow number, low-pressure cases. At low pressures, i.e. 50 and 100 psi, the percent modulation was 52% at a FN equal to 0.32, reducing to about 9% as the FN was increased to 1.9. At mean pressures of 300 psi, the modulation reached 18% and 14% at low and high FNs, respectively, only about 6% in error compared with the low-amplitude data. This error is most likely a result of air compressibility nonlinearities being more prominent at low pressures, since the normalized oscillatory-to-mean pressure becomes larger. This trend is further evidenced by the system's harmonics being more prominent at low flow numbers and low pressures.

Because there is only about 6% error between the linear and actual modulation levels at a mean pressure of 300 psi, the models are well suited to estimate the performance of the piston device at high pressures. Based on Figure 4.7 (b), the piston system clearly becomes limited in providing the percent modulation as the flow number increases, which is a problem for scaling this device to meet the needs of typical end applications. Testing of the throttle valve will lead to different results, as will be shown in the next section.

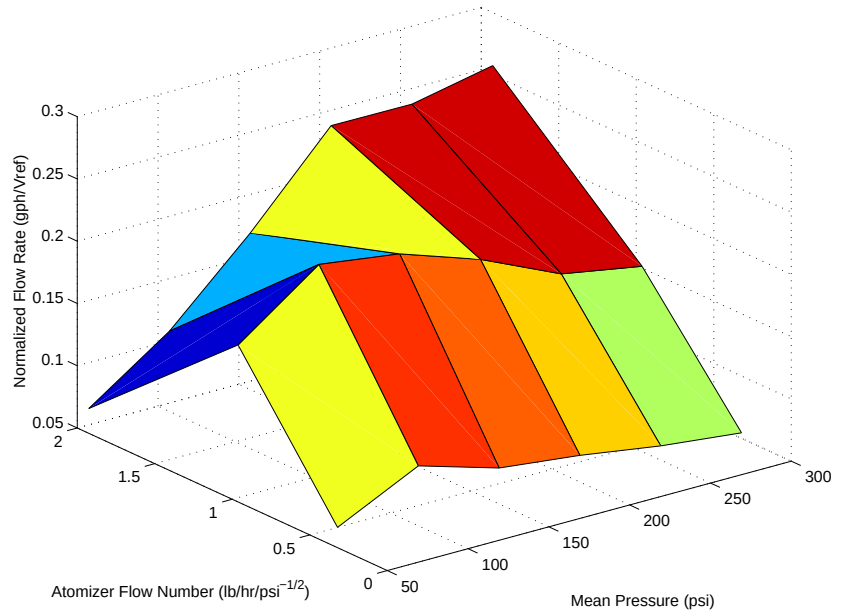

(a)

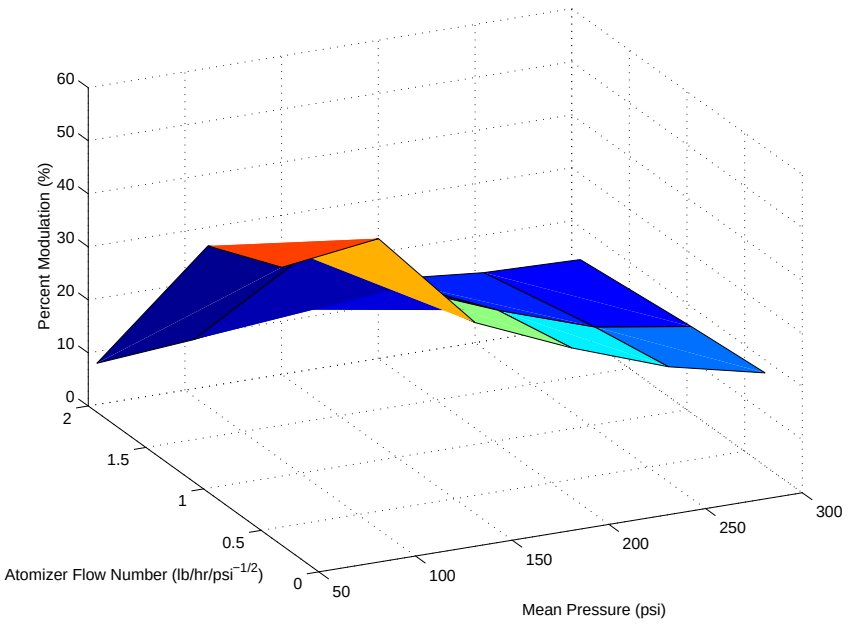

(b)

Figure 4.7: (a) Normalized flow rate and (b) percent modulation based experimental data at a forcing amplitude of 10 microns.

4.3.2 Characterization of Throttle Valve Device

Because of the piezoelectric actuator's low hysteresis, the piston fuel injector system exhibited nearly linear velocity source characteristics. The throttle valve, however, was found not to behave ideally due to hydrodynamic factors. For these reasons, the exact behavior of the valve as a source input to the system is not known. However, if the model-generated amplitudes cannot be scaled proportionally, it is debatable whether formulation of the correct source term is a prudent course of action. It is important to determine if the low-amplitude responses used in generating the FRFs may be scaled to amplitudes useful for combustion control.

Frequency responses were generated immediately upstream of the atomizer, at various operating conditions. At upstream supply pressures of 300 and 400 psi, the bypass valve settings were varied between two and six turns, which corresponded to flow numbers between 2.1 and 8.3 lb/hr/$\sqrt{\text{psi}}$. The pressure was varied between 40 and 180 psi. The result of this characterization is shown in Figure 4.8 (a) and (b), where the velocity amplitudes are expressed in terms of percent modulation. The reference voltage for this data was scaled by a factor of 16 to 2 volts. Clearly, percent modulation increases as the bypass setting increases, but decreases with mean downstream pressure. Also apparent is the decrease in the authority as the upstream supply pressure is increased, which is because the valve's offset must be lower as the supply is increased in order to maintain a constant downstream pressure. The valve's flow admittance is less sensitive to voltage at smaller offset values, hindering modulation. It is interesting to see that linear extrapolation predicts a modulation level reaching 100% for the 8.3 flow number cases at a 300-psi upstream pressure.

In order to explore the effect of higher-amplitude control signals, the valve was operated with a reference sine wave amplitude close to 2 volts, or 80% of the full scale of the 500-micron stack. For these tests, the mean position controller described in Section 2.7.2 was used to maintain the mean downstream pressure at 50 psi. Plots of the time traces can be seen in Figure 4.9 (a) and (b) at two upstream supply pressures and for various forcing

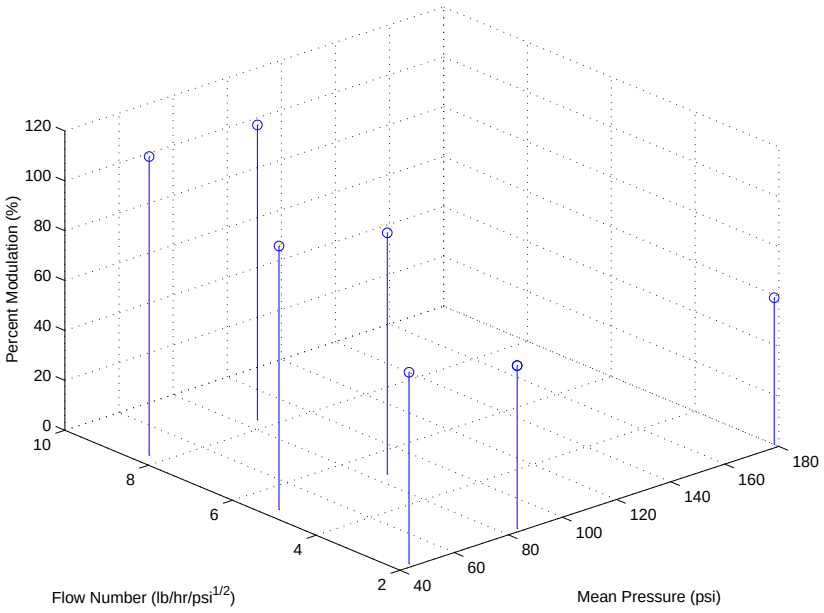

(a)

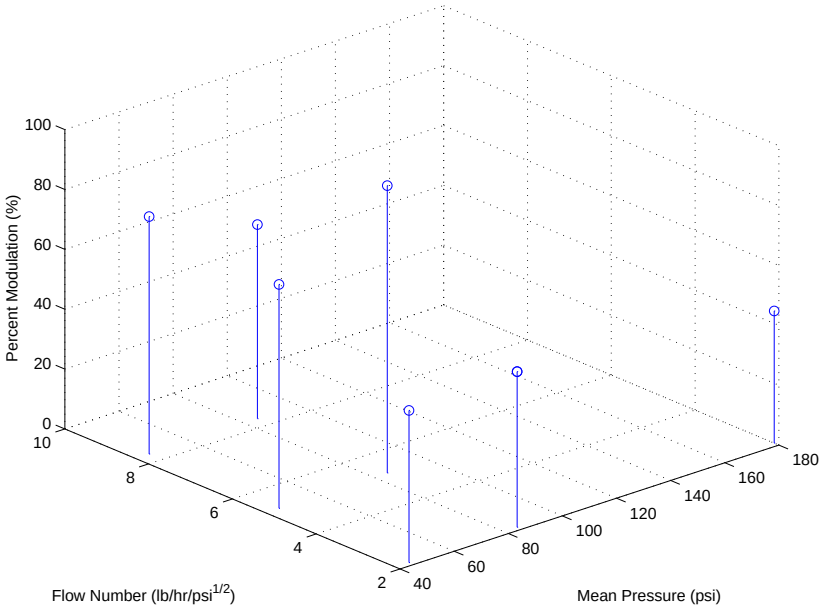

(b)

Figure 4.8: Percent modulation based on FRF data at forcing amplitudes of 0.125 V for upstream pressures of (a) 300 psi and (b) 400 psi.

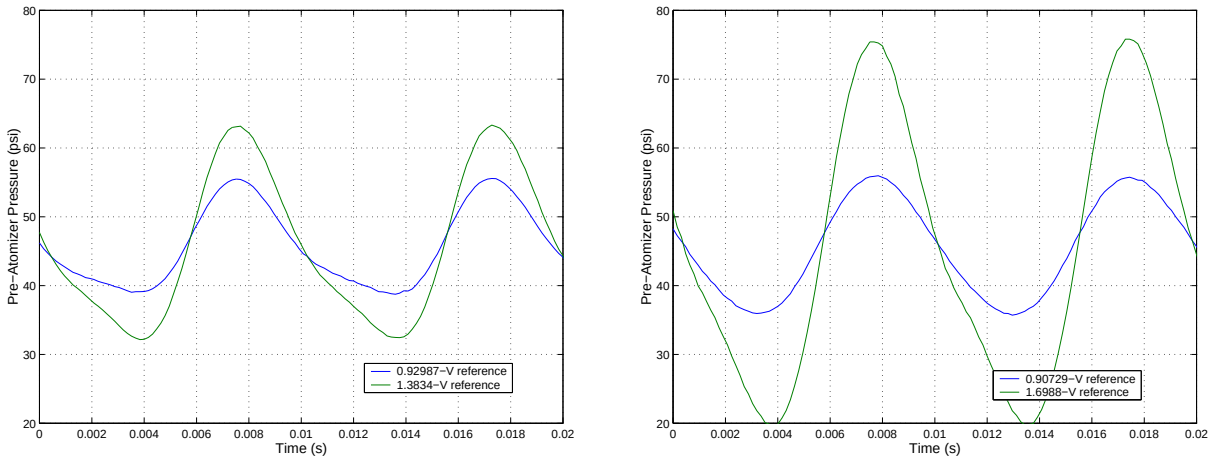

(a) **(b)**

Figure 4.9: Pressure time trace of throttle valve device forcing a 105-Hz sine wave at two amplitudes at a bypass setting of 6 turns and downstream pressure of 45 psi for upstream pressures of (a) 300 psi and (b) 400 psi.

amplitudes. As shown in the plots, the responses demonstrate nonlinear waveforms, especially at the higher reference voltages. From the linear spectrum of the two plots in Figure 4.9 (a), for example, it can be seen that the forcing amplitude increases by 40%, but the fundamental peak increases by nearly 80%. The fundamental peaks cannot be assumed to be proportional, thus the models will likely fail as the forcing amplitude grows large.

Once again, for the high-amplitude tests, the response of the fundamental peak was mapped at various operating conditions. The operating conditions used in the linear results were used in the present experiments. Percent modulation data from this set of experiments may be found in Figure 4.10 (a) and (b). These results show the same trends as in Figure 4.8, but the amplitudes are clearly in error. From the tabulated errors between linear and actual modulation levels in Tables 4.3 and 4.4, one can see the overall modulation levels are more than a factor of two lower than those from the previous tests. One source for disagreement is because the constant valve clearance assumption that was valid for the low-amplitude experiments does not apply for large forcing amplitudes. Also of interest are the several

Table 4.3: Error between percent modulations based on measured, quasi-linear data and data at high amplitude forcing of the throttle valve device for an upstream pressure of 400 psi at three operating conditions.

Mean Pressure (psi)	**Flow Number (lb/hr/$\sqrt{\text{psi}}$)**	**Linear** PM **(%)**	**Actual** PM **(%)**	**Error Between Linear and Actual** PM **(%)**
40	2.1	76.87	20.2	74
	8.3	119.8	23.89	80
180	2.1	58.82	18.39	69

Table 4.4: Error between percent modulations based on measured, quasi-linear data and data at high amplitude forcing of the throttle valve device for an upstream pressure of 300 psi at three operating conditions.

Mean Pressure (psi)	**Flow Number (lb/hr/$\sqrt{\text{psi}}$)**	**Linear** PM **(%)**	**Actual** PM **(%)**	**Error Between Linear and Actual** PM **(%)**
40	2.1	50.87	17.73	65
	8.3	79.38	62.4	21
180	2.1	44.18	14.52	67

conditions where modulation was not possible due to the mean position controller becoming unstable.

Based on the data, it can be seen that linear acoustic models would likely fail in correctly predicting the amplitude of the flow modulation. The nonlinearities associated with the valve source mechanisms, namely the pressure gradient source and the non-stationary valve discharge area make the linear throttle valve models invalid at high amplitudes. Even if the correct source term could be resolved, it would probably not lead to a greater understanding of the system's behavior than is presently known. A blend of the analytical with experimental work would be necessary to characterize this type of valve in different regimes.

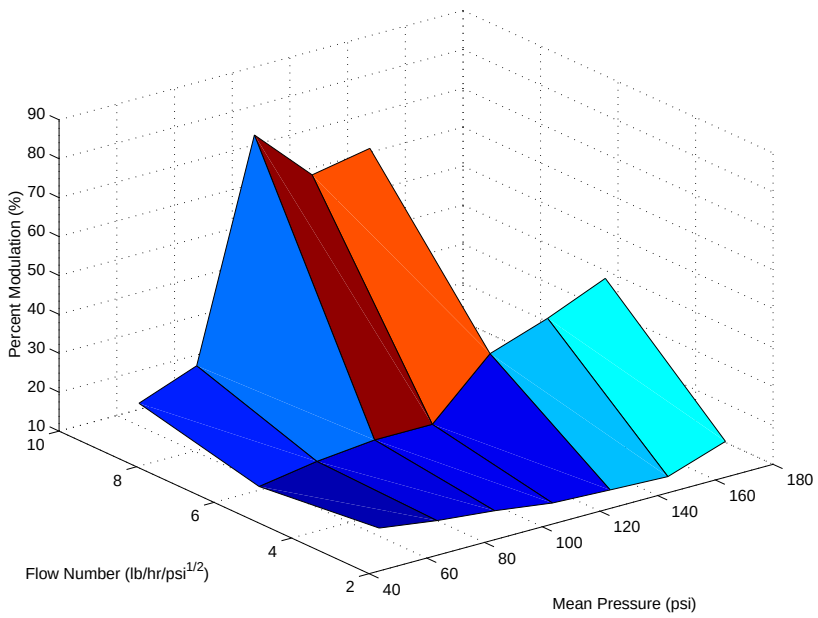

(a)

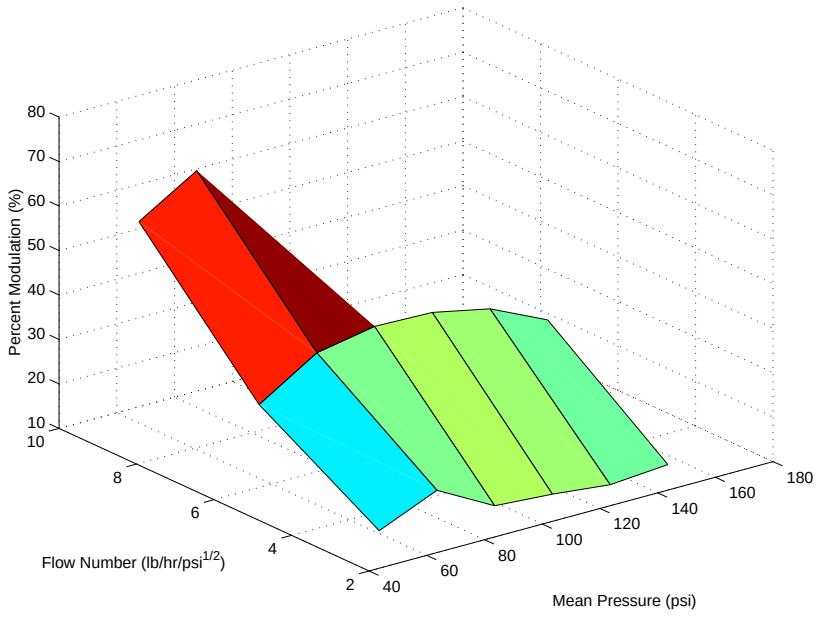

(b)

Figure 4.10: Percent modulation based on experimental data at forcing amplitudes of 2 V for upstream pressures of (a) 300 psi and (b) 400 psi.

In classifying the two fuel injector systems, the piston assembly can best be described as a configuration that is limited by its *component design*. As stated at the outset, the actuator's displacement and the piston diameter are contributors to the ability of the piston actuator to modulate a certain percent of the mean flow. This is confirmed by the trends seen in Figure 4.7, where 40% modulation at a flow number of 0.3 cannot be achieved above a mean pressure of about 150 psi, corresponding to a flow rate of 0.44 gph. In contrast, the throttle valve design developed in this research has performance characteristics that are more dependent upon the *operating conditions*, namely the downstream flow number and the supply pressure. Based on the results in Figure 4.10, as the flow number increases, the modulation authority increases. At a flow number of 8.3, and a supply pressure of 300 psi, 40% modulation can be achieved by operating above a downstream mean pressure of 90 psi or higher. Given the fact that the usable displacement is only about 200 microns, as the flow numbers approach that used in actual gas turbine applications, smaller actuators may be used to drive the valve effectively, given that they are still able to generate high forces. However, at these lower flow rates, the saturation limits in both mean position control stability and amplifier's minimum voltage become important factors. Several of those effects that were encountered in these experiments are described in the following section.

4.3.3 Mean Controller Stability and Saturation Limits

It was realized that, under normal operation of the valve, several adverse effects occurred in the mean pressure controller on the dSPACE computer. For one, when operating at high bypass settings, the mean position began to oscillate without being perturbed, sometimes leading to instability. Several observational assessments were made to determine the root cause of the problem, which are as follows. The stability problem was a function of mean pressure setting; that is, when the combustor controller was inactive, there was a certain pressure at which the instability occurred. It was also found that this instability occurred at reduced pressures when the combustor controller was active, and at further reduced pressures

as the combustor control gain was increased. As a whole, these effects are symptomatic of a loop instability problem common in classical control theory. The cause of this oscillation was due to the 30-Hz harmonic content from the piston pump.

The immediate course of action that was taken was to reduce the gain on the mean controller from 1.5 to 1.0. This effectively increased the stabilized pressure somewhat, improving the range of operation. The plots in Figure 4.10 were generated with this measure in place. As is evident in the plots, the pressure could not be operated greater than 180 psi without a stability problem, which was found to occur at lower pressures the more the bypass valve was opened. Modulation improves with the bypass valve setting, so this problem would severely limit the mean pressure range of the valve. In order to avoid this problem during combustor control experimentation, the decision was made to operate no higher than a flow number of 8.3 and a mean pressure of 100 psi.

The problem with operating with a limited supply pressure is that the atomizer becomes limited in its operating range. As the pressure drops, atomization quality becomes poor and a large Stokes number results, which is an unfavorable characteristic for combustion control. If the modulation levels were large, it would seem that the problem would increase in severity, compromising control authority. As a guide, Appendix A shows the lower limits of the operating pressures for many Delevan atomizers as reported by the manufacturer. With the exception of the 4.0 atomizer, each one has a bound at 75 psi. Control will be attempted at pressures both lower and higher than 75 psi to compare authority results.

Another problem with saturation occurred with the increase in combustor control gain. What was observed in the experiments was that the mean voltage position would drop as a function of amplitude. This had the effect of saturating the stack at zero volts, thus limiting the achievable amplitudes. If left unperturbed, the valve's motion follows the slow transient seen in Figure 2.29. When modulation is present, the mean valve position tends to be higher because this drift does not occur, which causes the mean position controller to reduce the mean voltage. Thus the valve's modulation was not limited by the amplifier's

limitations, but the zero-volt saturation. Future throttle valve designs that use a separate actuator to control the mean position would have a larger displacement potential, most likely eliminating this problem.

4.4 Combustion Control Testing

Based on the facts described in the preceding sections, there are numerous variables to consider when operating at particular settings on the combustor when making judgment on the control authority of the fuel injector. When the settings change, it is important to visualize control authority trends in order to relate trends to plausible hypotheses. This requires documentation of the fuel injection system performance in the form of a control performance map. Included in this map are several independent variables including: fuel flow rate, air flow rate, nozzle flow number, modulation amplitude, and both controlled and uncontrolled combustor pressure.

In this section, preliminary testing of the piston device will be presented, outlining its ability to control the combustor. Next, the throttle valve assembly, with its greater potential for modulation, was tested over a greater operating range. A control authority map was developed in order to visualize the trends with respect to the operating points. Given the known performance characteristics of the fuel injector, it will be shown that several theories can be attributed to the behavior of the combustor.

4.4.1 Hardware Setup

As outlined in Chapter 2, a phase shift controller was developed on the dSPACE control software platform for both the piston and the throttle valve. The valve's controller included the addition of the mean position controller, which was incorporated into the same GUI as the combustion controller. This GUI is shown in detail in Appendix D.

For both devices, the combustor pressure signal from the pressure transducer signal was fed into a HP FFT analyzer as well as a band pass filter before entering the dSPACE A/D board. The incoming reference signal was band-pass filtered between 80 and 125 Hz to provide the phase shifter with only the limit cycle frequency. The controller output was smoothed with a low-pass filter set to 500 Hz, which would also remove any transients created by the valve's mean controller that might cause damage to the stack. A schematic diagram of the electrical system is found in Figure 4.11, showing the signal conditioners, dSPACE controller, and other data acquisition devices. In order to gain control, a GUI interface would be used to adjust the gain and phase. The strategy used in the following experiments was to first increment the gain then adjust the phase to a value where a global minimum was found. The procedure would be repeated until the best reduction in the limit cycle amplitude was achieved.

The fluid delivery system consisted of a pressure regulation system and pressure gages, which were accessed from the fuel supply control panel. Stainless steel tubing was used to interface the valve and the combustor, which was secured in several locations so that vibrations would not extract energy from the acoustics. A copper tube coil was used for the tuning length to make the total downstream length equal to 11' for the valve assembly and 10' 1" for the piston assembly. Because the bypass characteristics are based on the pressure gradient across it, the bypass valve was emptied into a five gallon tank to ensure there would be no gravity head that may cause error in the resistance value. The assembled system is shown in Figure 4.12.

For these tests, a 0.5 atomizer with flow number equal to 0.32 $\mathrm{lb/hr/\sqrt{psi}}$ was used to impart control; a higher nozzle number created problems with attaining an unstable condition with the chimney. This atomizer size was chosen because clogging of the atomizer occurred quicker as the atomizer size was increased. Thus, it would be likely that some tests could be performed after the combustor reached steady-state conditions. Control was performed at a specific mean pressure while varying the equivalence ratio, and the results were recorded. Testing commenced after a 15-minute warm-up period to reach steady-state

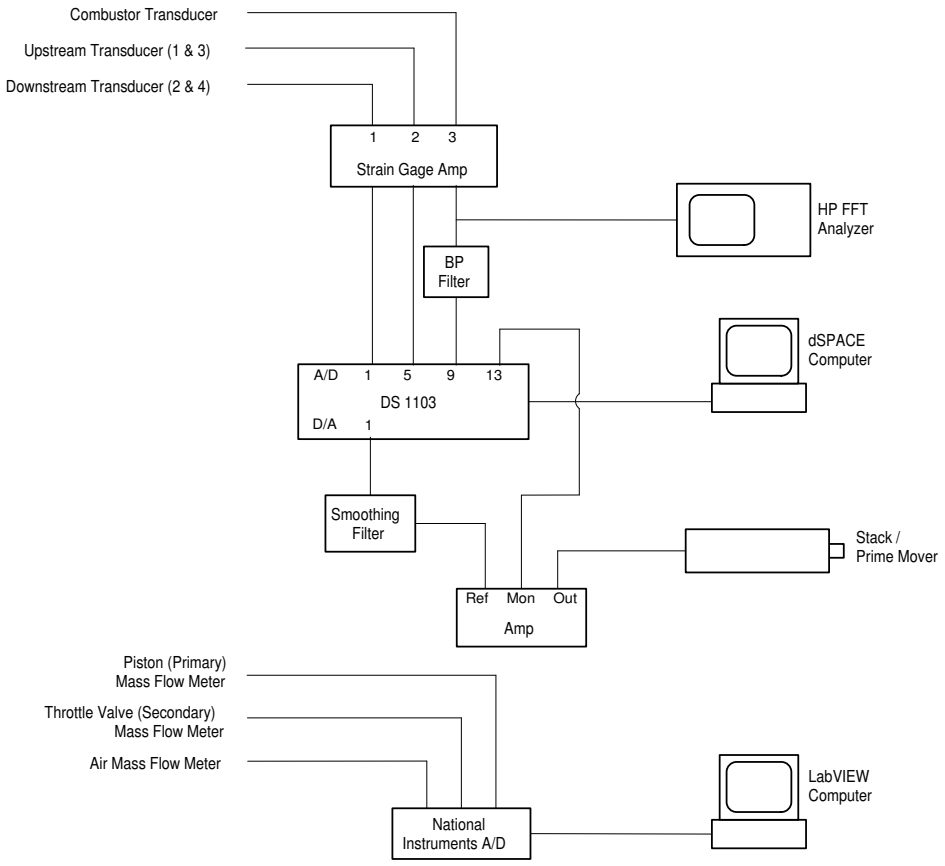

Figure 4.11: Schematic wiring diagram for combustion control.

temperatures. The bias uncertainty for all mean pressure values is ±2 psi.

4.4.2 Preliminary Piston-Based Control Experiments

Because of its implementation simplicity, the piston was tested first, with the intent of identifying its ability to achieve control of the system as well as demonstrate the control system developed was in working order. It is worthy to note that this testing was performed in December 2001, before the addition of swirl vanes in the combustor. The combustor was run at a power of 11 kW, with an equivalence ratio of 0.44, and a mean fuel pressure of 60 psi. The equivalence ratio f is defined simply as $\phi = \frac{A/F}{(A/F)_{stoic}}$.

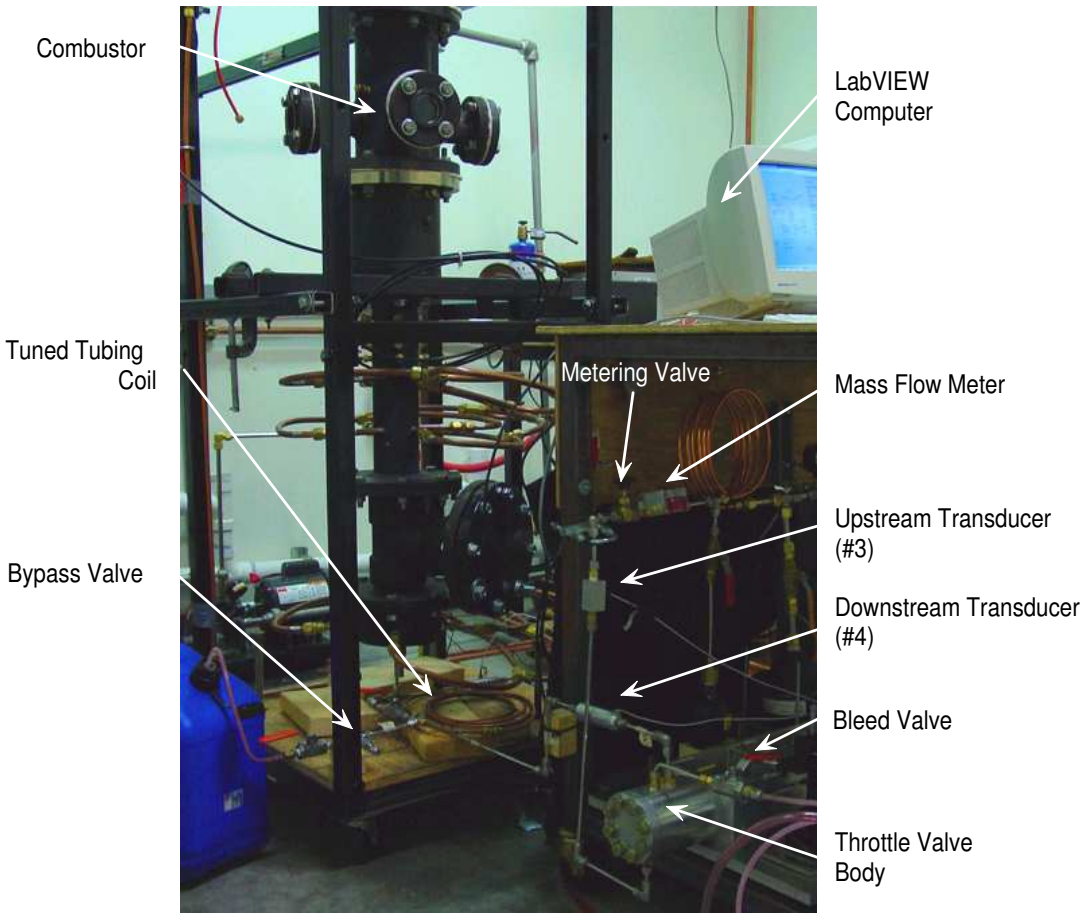

Figure 4.12: Photo of assembled ACC system hardware in the VACCG combustor.

The results of combustor control can be seen in the power spectra in Figure 4.13 and show that a reduction in the limit cycle frequency of about 23 dB resulted with a modulation level of 20%. Clearly the broadband energy decreased as well, reducing by about 17.1 dB as a result of control. The even harmonics disappear, which is one indicator that a limit cycle no longer exists. Upon close inspection, it can be seen that the fundamental peak is split slightly into two sidebands, indicating an inherent limitation of the phase shift controller. Investigation of the effect of phase on the reduction of the combustor pressure is revealed in Figure 4.14. For these experiments, the line pressure was 80 psi, the equivalence ratio was 0.48, and the percent modulation was roughly 20%. Clearly best control was obtained with

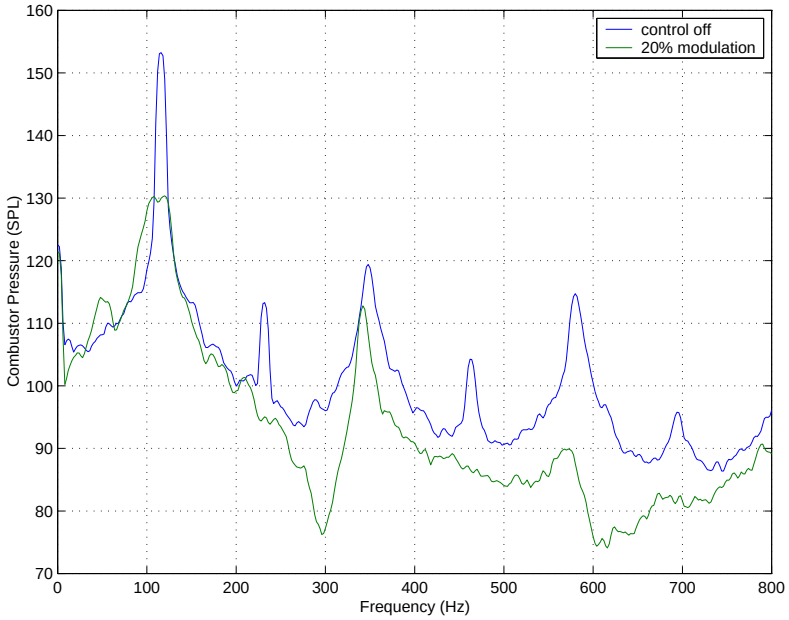

Figure 4.13: Comparison of uncontrolled and controlled spectra at 20% modulation at a 60-psi mean fuel pressure and $\phi = 0.44$.

a phase of 216 degrees, where 15 dB of reduction was achieved. The amplitude reduction approaches a minimum at a phase angles less than 144 degrees, which result in limit cycle amplitudes that are higher than the uncontrolled amplitudes. The main outcome of these experiments was a confirmation that the piston and phase shifter developed in this research are capable of obtaining combustion control.

4.4.3 Throttle Valve-Based Control Experiments

The throttle valve's modulation authority was tested in November 2002, with the addition of 60-degree swirl vanes to the rig. Because modulation levels above 40% could be achieved for many operating conditions, this device was used to create the combustion control map. The valve achieved best modulation at low pressures and high bypass settings, so testing occurred at a mean downstream pressure of 45 psi, a bypass flow number of 8.3, and an

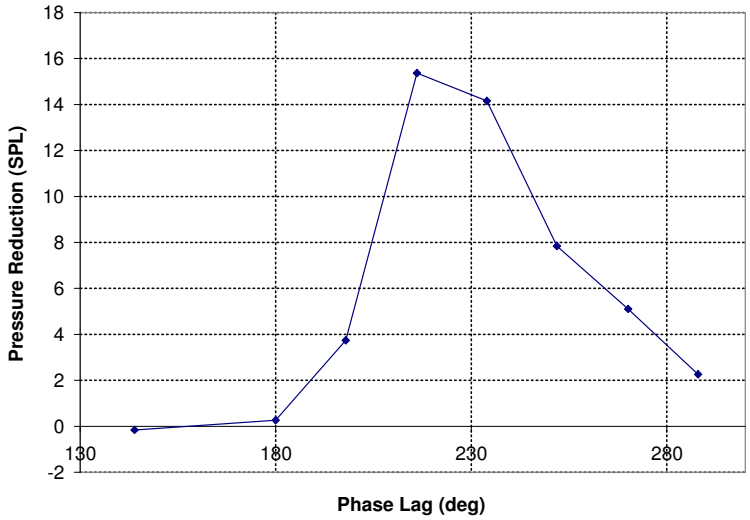

Figure 4.14: Limit cycle amplitude reduction versus phase at an 80-psi mean fuel pressure, $\phi = 0.48$, and $PM \approx 20\%$.

upstream pressure of 400 psi.

The best result of the control experiments is shown in the power spectrum in Figure 4.15. Clearly, a 26 dB reduction in the limit cycle amplitude was achieved at an equivalence ratio of 0.29 and a modulation level of 12% of the mean flow. The broadband reduction is apparent in the elimination of the even harmonic content and reduction of the noise floor. A typical characteristic of a non-limit cycling system is the existence of random pulsing in the time history. As shown in Figure 4.16, this appears to be the case, since the trace is much more erratic than the trace in Figure 4.3.

It was soon discovered, however, that this condition could not be reproduced at a later time. Mapping the 45-psi control performance with varying equivalence ratios revealed two different situations at two experimentation sessions, as shown in Figure 4.17. The solid blue line indicates testing performed during the course of one session, while the solid green line indicates testing at a later session. Both sessions used the exact same atomizer and

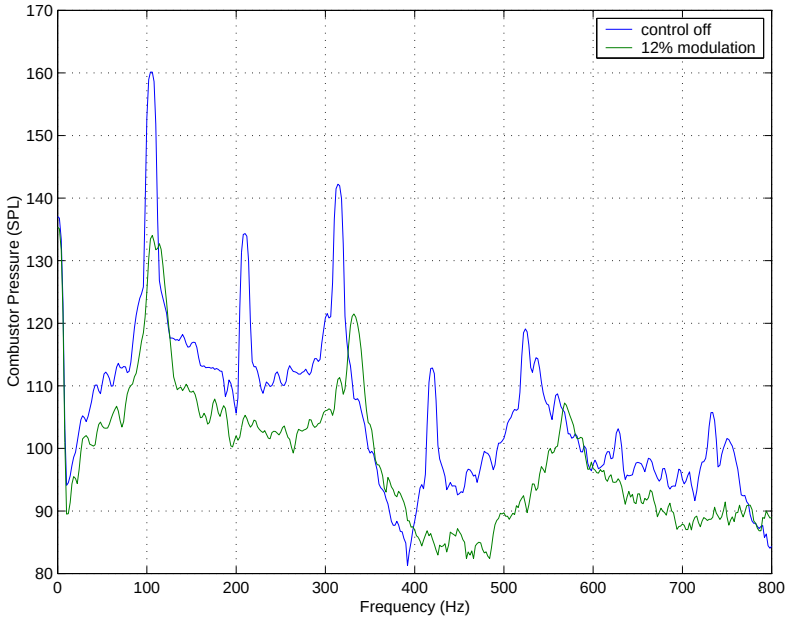

Figure 4.15: Comparison of uncontrolled and controlled spectra at 12% modulation at a 45-psi mean fuel pressure and $\phi = 0.29$.

testing began after approximately the same warm-up times. The only remarkable difference was that data collected in session #2 was performed approximately 1-1/2 hours after session #1. The dashed lines indicate the lean stability regions for the respective data sets. What is surprising from these results is how the control map changes with time, which is obviously a result of a time-varying plant. This is confirmed by the fact that the stability region moves along with the pressure reduction trends. This phenomenon also has an effect on the limit cycle amplitudes, as shown in Figure 4.18, which indicates that the instability becomes smaller the longer the combustor is operating.

The results seem to suggest that the atomizer becomes clogged during normal operation of the combustor. This is further supported by the fact that the mean flow diminishes during the course of the experiments by about 0.08 gph. Because the combustor is mounted vertically, unburned fuel that follows the recirculating air may collect at the atomizer surface. Intuitively, this problem would be exacerbated if the droplet sizes were to increase, such as

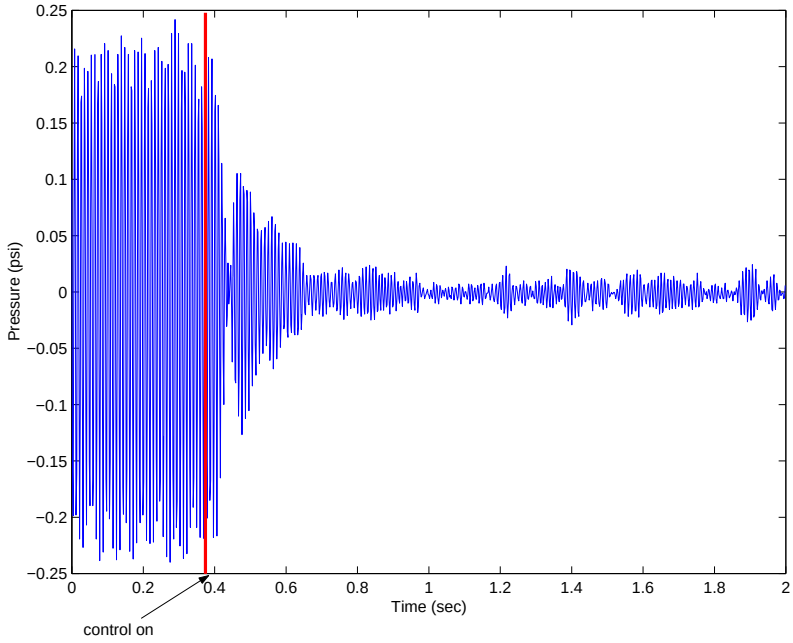

Figure 4.16: Time history of the instability with control at a 45-psi mean fuel pressure and $\phi = 0.29$.

using a larger atomizer or decreasing the mean pressure. The tests were performed again at 100 psi, well within the reported 75-psi operating range, and the problem continued to persist. Thus in future experiments, care was taken not to operate the atomizer for longer than 1-1/2 hours. The limit cycle amplitude would be observed on a periodic basis to ensure it is relatively constant with respect to data already taken. If there were to be any remarkable change, this would be an indicator that the atomizer must be changed out.

The existence of the stability region occurs because when the air flow increases, the flame becomes less compact. As the flame becomes more diffuse, the modal input strength gets weaker, which suppresses the instability. It is expected that the reason that the stable equivalence ratio moves toward a leaner regime is simply because the mean flow rate decreases. As equivalence ratio is decreased further into this stable region, the flammability limit is reached, causing the flame to blow off. The blow-off region was also observed to

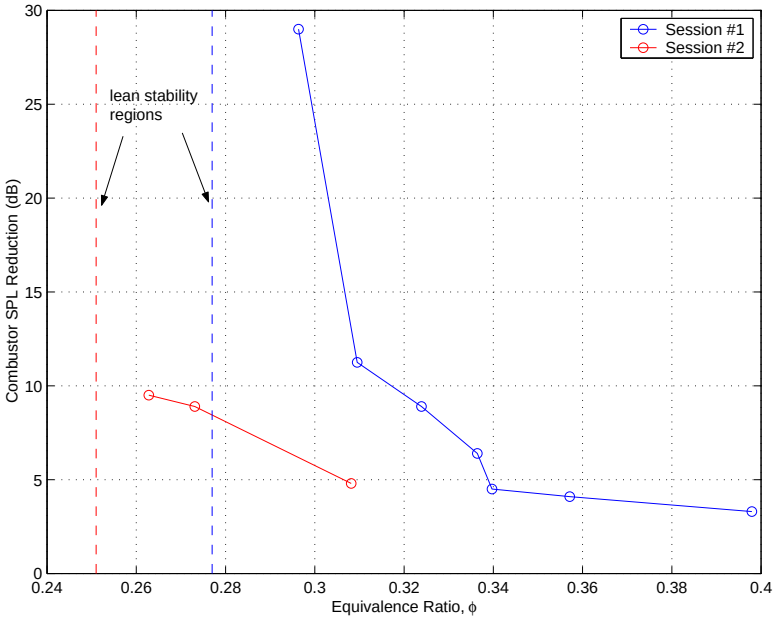

Figure 4.17: Limit cycle amplitude reduction as a function of equivalence ratio at two combustor conditions. The dashed lines indicate the stabilizing regions.

change with time as a result of this mean flow reduction.

Results from the testing at various equivalence ratios and pressures between 45 and 100 psi are provided in Figure 4.19. The lean stability region is overlaid on the plot for reference. The exhaustive set of data gathered from these experiments is presented in Appendix E. It is obvious that the best control occurs at equivalence ratios close to the stability region. As the equivalence ratio is increased further, the control authority drops off rapidly, then reaches a "pedestal" control regime, that exhibits only a few SPL reduction in the amplitudes. It is interesting to observe the inverse behavior of the instability amplitudes with amplitude reduction when comparing Figures 4.19 and 4.20. The amplitudes do not change significantly with equivalence ratio, so stabilizing gain is not likely to be the problem with obtaining control. It is thought that the instability amplitude reductions in the 100 psi data set was slightly in error, since it was the last set to be taken and began to exhibit characteristics of a clogged atomizer.

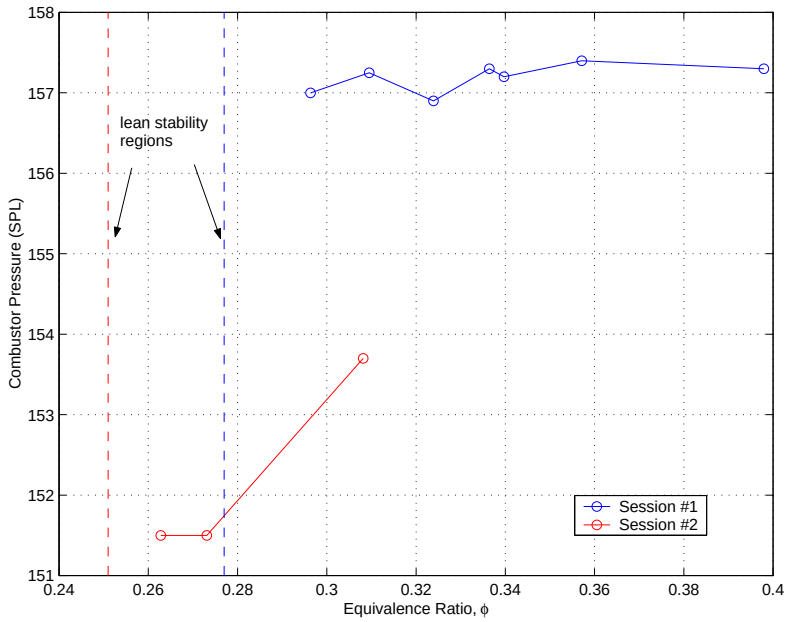

Figure 4.18: Limit cycle amplitudes as a function of equivalence ratio at two combustor conditions.

At best control, the instability often beats randomly, which is due to the phase not being stationary with time. The likely cause of this observation is likely due to the limitations of the phase shifting controller. As pointed out in [42], the phase shifter loses its effectiveness as the frequency shifts while obtaining control. Of course, small changes in frequency over time create changes in the control phase angle, which cannot be tracked if the user is unable to detect these subtle changes. Figure 4.21 shows the gain required to control the instability versus the same operating conditions as before. Here, it is noticed that the gain required to control the instability becomes less as the stability region is approached from rich equivalence ratios. However, it is interesting to note that in the best control cases, if too much gain is imparted, the system becomes unstable again. It is possible that the frequency shifts a significant amount so that the phase relations are time dependent, and thus uncontrollable by the linear phase shifter. Observing the control gains that offer the best control at conditions close to the lean stability region, it is observed that the theoretical

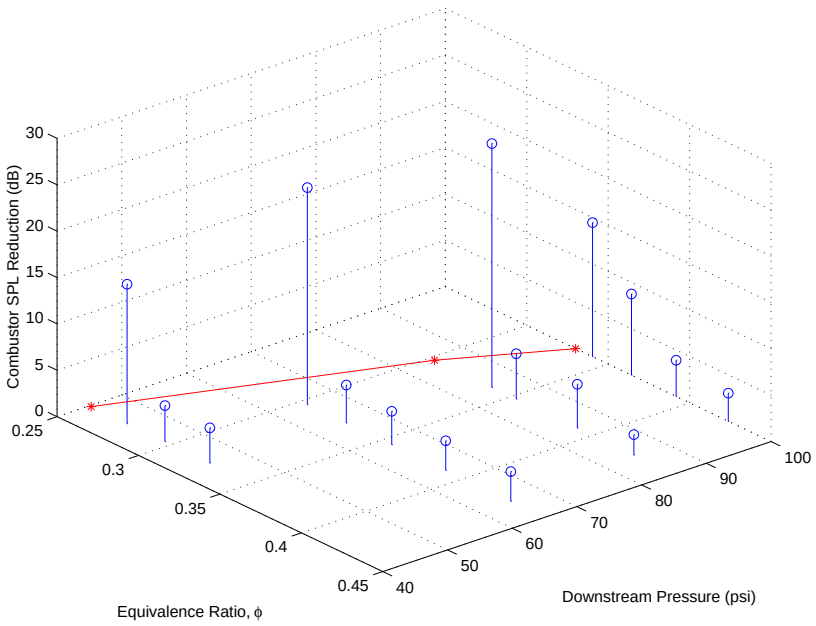

Figure 4.19: Limit cycle amplitude reduction versus equivalence ratio and mean fuel pressure. The lean stability region is shown in red.

percent modulation is only 11% at 45 psi. This seems to suggest that the pressure release exit plane boundary assumption is close to valid because the modulation levels required for control are quite small.

The data obtained at best control for each mean pressure setting is shown in Table 4.5. Because the thermoacoustic plant requires more control gain as the mean pressure increases, it is not completely conclusive whether or not droplet sizes are a major influence on authority. However, if the mean pressure is decreased below the atomizer's lower pressure bound of 75 psi, it would be plausible to expect a substantial degradation in control authority if the percent modulation remains constant. This was not the case, so it is likely that other effects are responsible for the lack of control. The sharp decrease in controllability as ϕ increases depicted in Figure 4.21 suggests a nonlinear trend, possibly due to the spray interaction with vortical structures. This has been known to cause clipping of the acoustic waveform due to the development of shear layer waves and mostly happens when the Stokes number is less

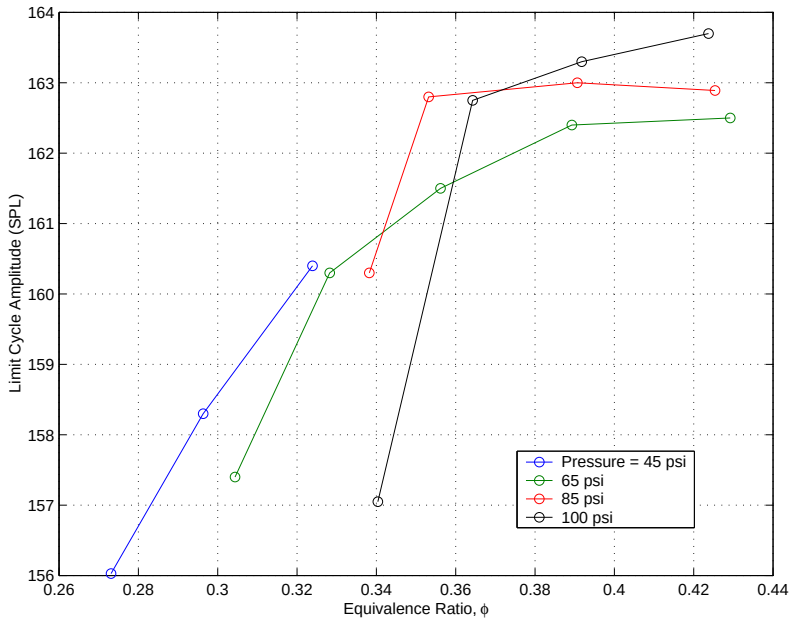

Figure 4.20: Uncontrolled limit cycle amplitude versus equivalence ratio and mean fuel pressure.

Table 4.5: Error between percent modulations based on measured, quasi-linear data and data at high amplitude forcing of the throttle valve device for an upstream pressure of 300 psi at three operating conditions.

Downstream Pressure (psi)	**Air Flow Rate (scfm)**	**Thermal Power (kW)**	**Equivalence Ratio ϕ**	**Percent Modulation (%)**	**Limit Cycle Amplitude (SPL)**	**Amplitude Reduction (dB)**
45	25.5	11.1	0.27	12	156	15
65	27.5	13.3	0.30	12	157.4	23.4
85	28.3	15.3	0.34	16	160.3	26.3
100	30.3	16.5	0.34	37	157	14.5

than unity (the droplets are small) further downplaying the assessment of the existence of large droplets. As the forcing amplitude increases, the droplets undergo a large variation in Stokes number during each period of oscillation. This may also lead to the inability to achieve control with increasing ϕ.

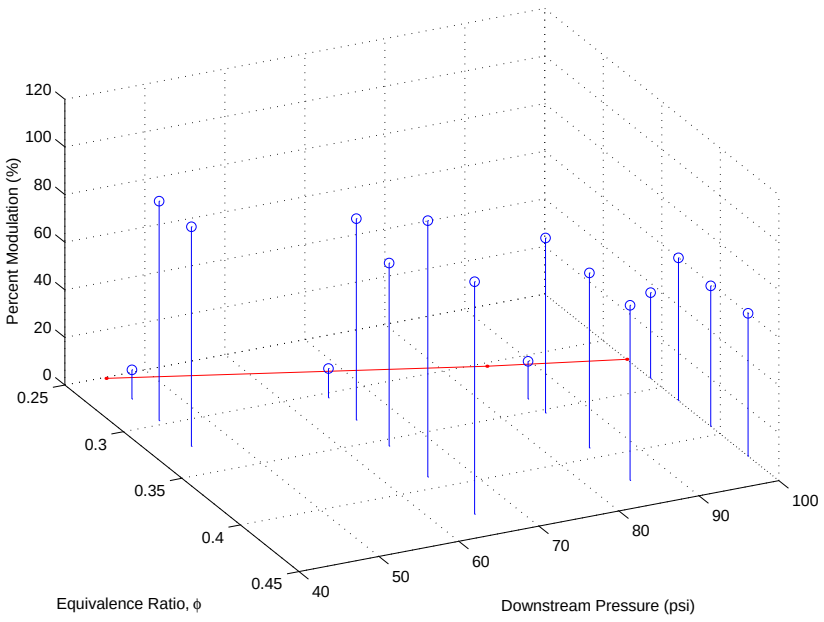

Figure 4.21: Stabilizing gain versus equivalence ratio and mean fuel pressure. The lean stability region is shown in red.

The conclusions that can be made of these combustor control experiments showed that several factors are likely to have contributed to the failure of the fuel pulse to control the unstable combustor at all settings and the extent to which each play a role can only be qualitatively assessed. First, shear layer effects acting on the flow at the atomizer were expected to change the exit plane boundary relative to the pressure release assumption is no longer valid. This may have the effect of altering the actual modulation levels by several dB. Second, the turbulent interaction of the droplets with the air flow may cause the pulse to be attenuated, primarily if the Stokes number is less than unity. The trends observed in the data do not suggest attenuation due to a large average droplet size, but large variation of the droplets within one cycle of oscillation may lead to such attenuation.

4.5 Chapter Summary

The applicability of the models to a variety of settings had mixed success. It was found that scaled amplitudes generated by the piston models matched up exceptionally well with actual data at those levels at several high-mean-pressure cases. Thus, the fidelity of the acoustic models is reasonable enough to predict the amplitudes without the need for experimentation. This is an asset to the development of future piston fuel injection devices, which are limited on the basis of the hardware components.

Although not modeled, low-amplitude data taken of the throttle valve did not match up well with the high-amplitude data. At many operating points, the high-amplitude data was lower than that extrapolated from low-amplitude tests by at least a factor of two. However, throttle valve modulation is quite dependent on the operating conditions, so design of the actuator is not as critical to the overall authority potential of the system. Thus, it is not completely necessary to have accurate models to observe its performance a priori to development. The models may still be useful in determining the performance at end-application conditions not practically achievable in the laboratory, such as high ambient pressure, higher flow rates, etc.

When tested in the combustor, both fuel injector devices were able to attain control, although only at limited operating points. At an equivalence ratio of 0.29 and a mean fuel pressure of 45 psi, a 26 dB reduction was achieved with 12% theoretical modulation. Control was achievable because this setting was close to the lean stability region of the combustor. As the settings moved towards more rich conditions, control authority was drastically reduced. Several hypotheses for this reduction were formulated:

- Vortex formation may cause significant alteration of the acoustic boundary at the atomizer exit, which may significantly impact the velocity modulation on the supply side.
- The same vortical effects cause shear layer waves and may lead to nonlinear effects on

the transmitted waveform.

- Large droplet sizes during modulation at low mean pressures are unfavorable for combustion control due to droplet convection.
- Large temporal variation in droplet size over a period of oscillation.

The extent to which each of these properties affect the transmission of the fuel pulse to the flame location is not completely certain, however the data provided some information on which factors are most likely to attenuate the fuel pulse. It is theorized that the nonlinear clipping due to vortex generation and large cyclical droplet size variations were the largest contributors.

The combustion control tests performed herein were intended as a preliminary evaluation of ACC authority because the combustor plant and the turbulent effects are likely to be substantially different between various combustor systems. LDI configurations are expected to present a further challenge because, in general, the mean droplet size is much smaller than for lean premixed combustors. Nonlinear effects due to fluctuating vorticity at the atomizer exit will likely be more prevalent, causing the heat release waveform to be clipped.

Chapter 5

Conclusions

Thermoacoustic instabilities are a major problem in gas turbine combustors. As a means for control, high-bandwidth fuel injection has been proven to be viable for instability suppression in small-scale rigs, but the technology has not yet progressed to the point where implementation can be realized in actual-sized combustors. The present research has focused on finding methodologies that eliminate the need for trial and error approaches necessary in developing fuel injection systems for large-scale applications. As outlined in Section 1.3, the specific objectives for this research were as follows:

Design and build fuel injector configurations using piezoelectric actuation to fulfill 700-Hz bandwidth and 40% modulation criteria representative of industrial and governmental needs. Focus was placed on two modulation configurations: a piston/check valve and a throttle valve configuration, with the piston device suited for modulation of the primary fuel entering the combustor and the throttle valve applicable to either the primary or secondary fuel lines.

Develop methodologies and analytical tools to facilitate fuel injector design by minimizing the number of experiments required to validate their performance. It was desired that these models be simple to generate so that they can be used as a design

tool. Moreover, they must be robust enough to accommodate a wide range of operating conditions and have a high fidelity to prediction of the behavior at high forcing amplitudes.

Evaluate the authority of the fuel injectors in their ability to modulate heat release. Assessment of the heat release was accomplished by determining the effectiveness of these devices in achieving control of an unstable laboratory-scale turbulent combustor rig. To study the performance of the injector hardware, control was imparted by using a linear phase shifter. By observing the control authority, attempts were made at arriving at qualitative conclusions on the limiting factors affecting control performance.

In the design, piezoelectric actuators were selected for their inherently high-bandwidth, high force capabilities. The fact that piezoelectric stacks are only capable of a small amount of displacement requires careful selection of actuators and prime movers in order to maximize the energy transmitted to the fluid. Following construction of the two injector devices, preliminary testing in Chapter 2 showed that authority was diminished because of both mechanical and fluidic compliances acting on the fluid. Thus, efforts were made to improve the stiffnesses of the mounting brackets and fluid piping and eliminate the air content before optimizing the actuator and prime mover sizes to provide the desired modulation levels. However, prediction of the modulation levels was problematic due to a lack of accurate dynamic models of the complete fuel delivery system.

To better understand the dynamic effects, a physics-based approach to modeling the liquid fuel system was developed in Chapter 3 by forming one dimensional transmission line models of the fuel injectors and delivery system. Acoustic models for the two injection schemes were validated with model-based experimentation. Upon performing the unsteady flow analysis, it was realized that the low forcing amplitude FRFs matched up well between the model and data for a variety of operating conditions. The dissipative effects could be characterized, which is useful in identifying the problem points to the injector's authority. In an effort to amplify the steady-state amplitudes at the instability frequency, the fuel line length was tuned such that the pipe's first resonance corresponded to the limit cycle

frequency. At certain operating conditions, particularly at low flow numbers, this had the effect of increasing the gain by as much as 20 dB between resonance and off-resonance driving frequencies. Because the exit plane boundary condition is relatively insensitive to the upstream FRFs, the atomizer velocity cannot be determined with full confidence. An upper-bound estimate of the velocity can be deduced if a pressure release boundary is assumed. With further research, velocity measurements may be correlated to the model-generated velocities to gain a more accurate prediction of the exit plane boundary. In characterizing the fidelity of the acoustic models, it was found that the models scaled linearly for the piston assembly, but nonlinearly for the throttle valve. Overall, the piston assembly's performance can be classified as design limited, while the throttle valve is operating condition limited.

Combustor tests performed in Chapter 4 revealed that reductions by as much as 26 dB in the limit cycle amplitude and 23 dB in the broadband energy could be achieved under limited operating conditions. However, control was extremely sensitive to the operating conditions, such as equivalence ratio and mean fuel flow settings. Generally, best limit cycle amplitude reductions were achieved close to the combustor's lean stability region. As expected, along the ridge of best control, the required percent modulation increased with an increase in combustor power. As operating conditions move away from the stability region, reductions in the limit cycle decreased significantly, even as the estimated modulation approached 100%. The likely cause of this is because, as more gain is needed to stabilize the thermoacoustic poles, the interaction between the atomized droplets and the turbulent effects in the combustion region cause a nonlinear attenuation of the heat release rate waveform. Variations in droplet distribution, vorticity of the gases, and the combustor's acoustic field are all expected to play a role in these losses.

5.1 Future Work

Several issues remain to be addressed in order to complete fulfillment of the goals established at the outset. For one, it is shown that combustor chamber dissipation mechanisms limit

the control authority. It is crucial to study these chamber effects in order to determine if primary-injection ACC is realizable for different combustion systems, such as LDI configurations. For another, the internal hydrodynamic behavior of the throttle valve dominates its behavior at both steady state and at high frequencies. In future designs, it is important to characterize the complex nonlinear dynamics in order to understand and simulate the valve's operation. Lastly, the acoustic models developed herein need to be made more robust and, at the same time, streamlined for developers to use. After these effects can be understood, the analytical models may be altered to incorporate these effects to gain a more accurate correlation between the measurable pressures, exit plane velocities, and heat release authority. These three items are outlined in depth below.

1. **Study the effect of fuel modulation on heat release authority by first exploring the effects of atomization as well as convective and turbulent effects.**

The dynamics downstream of the atomizer can be thought of a series of "black boxes" that consist of acoustic two-ports. These "black boxes" contain dynamics associated with jet formation, atomization, convection, and turbulence that ultimately affect the velocity and droplet distribution at the flame. Each of these components must be understood fully before an accurate prediction of the heat release authority can be made. These processes will be characterized through empirical studies, which will eventually be used in forming complete models of these subsystems.

In the transmission line models developed in Chapter 3, a simplified approach was used to estimate the liquid velocity at the atomizer exit plane by assuming a pressure release boundary. In actuality, turbulent flow and shear layer instabilities cause nonlinear phenomena that have an effect on the flow at the atomizer and dissipation of energy after the atomizer, which were not treated in the models. It is suggested for future research that the most reliable way of determining post-atomizer flow characteristics be determined with diagnostics such as LDV and PDPA. The models can thus be correlated to the actual flow at the atomizer, allowing an empirically determined impedance to be found.

Atomization processes are shown in the literature to be impacted by oscillating chamber pressure, which may be a cause for concern for authority. Primarily, past studies [3] have been focused on coupling between the acoustics and the behavior of a liquid jet. Studies involving an imposed acoustic field are necessary to explore the impact of these pressure oscillations on the separated liquid flow and droplet behavior as it convects towards the flame.

A correlation between perturbed fuel levels and heat release rate requires accurate knowledge of the heat release transfer function. In many turbulent, bluff body- and swirl-stabilized flames has not been generated for the particular setup of the VACCG combustor. The benefit of this research would allow for correlation of injector authority to heat release. Heat release authority under stable combustion conditions can be gathered using OH* chemiluminescence measurements by varying the equivalence ratio by means of modulating fuel flow. Using this technique, along with PDPA diagnostic capability within the combustor, the cold-flow dynamic fluid behavior can be compared to reacting flow behavior.

Combustor control experiments conducted on the VACCG rig in Chapter 4 should be regarded as an initial effort to characterize fuel injector authority due to fundamental problems with the rig itself. The atomizer pyrolysis problem is indicative of the atomizer experiencing excessive thermal loading possibly because of an increased recirculation of the hot gases. It was observed that the flame resembled a diffusion flame at settings that resulted in a thermoacoustic instability, which would promote a longer flame that would follow the recirculation paths. Further evidence that points to a diffusion flame is that equivalence ratios of 0.25 are normally not attainable for swirl-stabilized combustors, which was the case at a fuel pressure of 45 psi. Before further reacting flow assessments are made, it is advised that a solution to the combustion problem be implemented so that the flame more closely resembles lean premixed behavior.

2. **Development of a next-generation throttle valve design based on knowledge and design strategies described in this research.**

Because of its promise in the ability to maintain high authority under high mean flow conditions, studies on new throttle valve arrangements should be explored. This will be accomplished by designing a new valve configuration that will allow for optimization of the actuator and prime mover components based on the methodologies presented in this work.

The present design was not optimized for primary-line actuation because it required the stack's mean position to be controlled in order to maintain a constant pressure. In order to effectively implement mean pressure control, the modulating components should be decoupled from the mean pressure actuation. In so doing, the displacement will not be removed from the modulating actuator, maximizing its useable displacement range and thus minimizing valuable displacement and actuator power requirements. In addition, the improved design can aid in the understanding of the hydrodynamic effects and how they improve the valve's performance at high flow numbers. Decoupling of the components may be done in one of two ways: arrange the actuators in series and use one throttle valve device to perform both actions, or use two throttle valve devices with the actuators working in parallel. The second option requires more components, but offers much more flexibility in matching the individual actuators to respective prime movers. The second option would benefit actuators that are only capable of providing low forces, such as voice coils.

A redesign of the throttle valve requires selection of new actuators for high-bandwidth modulation. The robustness of piezoelectric technology must be thoroughly re-assessed if it is to be used for this application. One contributing factor to the failure of the stack was likely because of the mechanical impact forces present during normal valve operation. Upon redesigning the throttle valve, it should be considered how to safeguard the stack from conditions in which it may be placed under tensile loading. One measure that might be worth considering is to design the stem and seat such that flow may stop without the valve actually reaching a hard stop. Another contributor may have been the fact that high voltages applied to the stack for long periods of time tend to degrade the ceramic material. In future designs, bi-polar stacks would minimize the degradation because they are able to modulate about a zero mean voltage.

Voice coils may be used, but would be best suited with the mean pressure and modulating actuator operating in parallel with separate prime movers. The advantage of using this type of actuator is that the valve can be designed with high displacements in mind, which means that the valve stem area can be reduced. Neglecting the hydrodynamic forces acting on the valve for the moment, a small stem surface area generally results in very low oscillatory pressure gradient forces that the actuator has to overcome. The valve's geometry may closely resemble that of a needle valve, which have a relatively small surface area but require large displacements to modulate the orifice.

3. **Advance progress on the acoustic models to allow a more comprehensive assessment of fuel injector performance and make this design tool more powerful.**

Streamlining these acoustic models to ease model formation would definitely be beneficial to fuel injection system designers. Namely, because the length of the nozzle is much less than a single wavelength over the frequency range studied, the geometrical area changes and localized impedances may be replaced by an effective impedance. The validity of this impedance would be easily validated by the empirical impedance that would be determined from post-atomizer velocity measurements.

Much experimentation needs to be done before an understanding of exact source term in the throttle valve assembly is to be determined with confidence. Indeed it is shown in Chapter 2 that the pressure gradient source roughly resembles band-pass filter behavior, whose characteristics change nonlinearly with operating conditions. The nonlinear nature of the source term leads to an inability to model the valve completely, so it is suggested that this source term be identified to enable this source term to be accurately captured in the models. It is highly unlikely that the hydrodynamic processes could be effectively contrived without the use of finite element methods on the deflection mechanics of the valve. Modeling the fluid dynamics and the mechanical deflection may lead to successful characterization of the valve. Perhaps a more practical method is to use system identification techniques to

generate transfer functions of the source at various operating settings. A new throttle valve design with a small surface area may not exhibit these hydrodynamic effects, so it is possible that the task of modeling the new valve would be simplified.

Some question has been left as to the validity of the piston assembly models over all operating conditions, in particular, the low-pressure cases. The reasons for this may be attributed to the fact that the air bubble models or the nonlinear mean gradient impedances tend to be in error at these conditions. It is suggested that further validation testing should be focused on low-pressure situations to gain a better match between the model and experimental FRFs. Also, because the piston models show good fidelity up to forcing amplitudes of 10 microns, experimentation should be made at higher amplitudes to aid in development of a piston fuel injector capable of 40% modulation at high flow numbers. Once this is accomplished, it is urged that a next-generation piston fuel injector device should be designed by taking advantage of several of the design methodologies presented in this work. As with the throttle valve redesign, focus should be placed on trade off studies with other actuation methods, such as voice coil technologies.

Because of the significant change in specific acoustic impedance ρc at the atomizer exit plane, it is reasonable to assume that the dynamics upstream of the atomizer are decoupled from combustor chamber processes. This is important if these transmission line models are used as a forcing term into CFD models that would capture the combustor's dynamics. This would certainly be instrumental in determining the control authority of certain fuel injector systems in a particular combustor system as a more comprehensive design tool.

Bibliography

[1] Abdel-Wahab, S., Bier, A., Brar, J., Cordivari, M., Early, P., Sides,J., *Development of a Pulsed Fuel Injection System for Active Combustion Control,* ME 4015/4016 Senior Design Report, 2002.

[2] Allen, J., Al-Nakhi, M., Brown, R., DeCastro, J., Desrosiers, J., Henke, D., Herbaugh, M., Jones, H., Knight, S., Lollis, M., Mauck, S., McLaughlin, D., Miller, O., Maloney, C., Wills, M., *Active Combustion Control Device - Final Report,* ME 4015/4016 Senior Design Report, 2001.

[3] Anderson, W.E., Miller, K.L., Ryan, H.M., Pal, S., Santoro, R.J., *Effects of Periodic Atomization of Combustion Instability in Liquid-Fueled Propulsion Systems,* Journal of Propulsion and Power, Vol. 14 No. 15, 1998.

[4] Bechert, D.W., *Sound Absorption Caused by Vorticity Shedding, Demonstrated with a Jet Flow,* Journal of Sound and Vibration, Vol. 70 No. 3, pp. 389-405, 1980.

[5] Bloxidge, G.J., Dowling, A.P., Hooper, N., Langhorne, P.J., *Active Control of Reheat Buzz,* AIAA Journal, Vol. 26 No. 7, pp. 783-790, 1988.

[6] Carson, J.M., *Subharmonic and Non-Subharmonic Pulsed Control of Thermoacoustic Instabilities: Analysis and Experiment,* Master's Thesis, Virginia Polytechnic Institute and State University, December 2001.

[7] Cooper, C.S., Laurendeau, N.M, *Laser-Induced Fluorescence Measurements In Lean Direct-Injection Spray Flames: Technique Development and Application,* Measurement Science and Technology, Vol. 11, pp. 902-911, 2000.

[8] Culick, F.E., Yang, V., *Prediction of the Stability of Unsteady Motions in Solid-Propellant Rocket Motors,* Nonsteady Burning and Combustion Stability of Solid Propellants, Progress in Astronautics and Aeronautics, Vol. 143, pp. 719-780, 1992.

[9] Dombrowski, N., Johns, W.R., *The Aerodynamic Instability and Disintegration of Viscous Liquid Sheets,* Chemical Engineering Science, Vol. 18, pp. 203-214, 1962.

[10] Dressler, J.L., *Characterization of a Velocity-Modulation Atomizer,* Review of Scientific Instruments, Vol. 65 No. 11, pp. 3563-3569, 1994.

[11] Eisenhower, B.A., *Identification of Thermoacoustic Dynamics Exhibiting Limit Cycle Behavior,* Master's Thesis, Virginia Polytechnic Institute and State University, May 2000.

[12] Greenwood, A., *Implementation of Adaptive Filter Algorithms for the Suppression of Thermoacoustic Instabilities,* Master's Thesis, Virginia Polytechnic Institute and State University, February 2003.

[13] Gysling, D.L., *Combustion System Damping Augmentation with Helmholtz Resonators,* ASME 98-GT-268. Stockholm, Sweden, 1998.

[14] Haile, E., Laç as, F., Desrayaud, C., Veynante, D., Durox, D., *Characterization of a Liquid Fuel Injector Under Continuous Modulated Flow Conditions,* CNRS et de l'Ecole Centrale Paris, Grande Voie des Vignes, 1998.

[15] Hantschk, C., Hermann, J., Vortimeyer, D., *Active Instability Control With Direct-Drive Servo Valves In Liquid-Fueled Combustion Systems,* 26th International Symposium on Combustion, pp. 2835-2481, 1996.

[16] Heister, S.D., Rutz, M.W., Hilbing, J.H., *Effect of Acoustic Perturbations on Liquid Jet Atomization,* Journal of Propulsion and Power, Vol. 13 No. 1, pp. 82-88, 1997.

[17] Heising, R., Lubarsky, E., Neumaier, M., Neumeier, Y., Zinn, B.T., *Periodic Liquid Fuel Sprays Combustion Processes and their Damping of Combustion Instabilities,* 38th Aerospace Sciences Meeting and Exhibit, AIAA 2000-1024.

[18] Hermann, J., Gleis, S., Vortmeyer, D., *Active Instability Control of Spray Combustors by Modulation of the Liquid Fuel Flow Rate,* Combustion and Science, Vol. 118 pp 1-25.

[19] Howe, M.S., *Attenuation of Sound in a Low Mach Number Nozzle Flow,* Journal of Fluid Mechanics, Vol. 91, pp. 209-229, 1979.

[20] Ingebo, R.D., *Atomization of Ethanol Jets in a Combustor with Oscillatory Combustion-Gas Flow,* NASA TN D-3513, 1966.

[21] Kiel, B.V., *Review of Advances in Combustion Control, Actuation, Sensing, Modeling and Related Technologies for Air Breathing Gas Turbines,* 39th Aerospace Sciences Meeting and Exhibit, AIAA 01-0481.

[22] Khanna, V.L., *A Study of the Dynamics of Laminar and Turbulent Fully and Partially Premixed Flames,* Ph.D. Dissertation, Virginia Polytechnic Institute and State University, 2001.

[23] Khanna, V.L., Vandsburger, U., Saunders, W.R., Baumann, W.T., *Dynamic Analysis of Burner-Stabilized Flames, Part I: Laminar Premixed Flame,* Proceedings of the Americal Flame Research Committee International Symposium, Newport Beach, CA, Sept. 2000.

[24] Kinsler, L., Frey, A., Coppens, A., Sanders, J., *Fundamentals of Acoustics,* John Wiley and Sons, 3rd ed., 1997.

[25] Lagimoniere, E.E., *The Design and Construction of a High-Bandwidth Proportional Fuel Injector for Liquid Fuel Active Combustion Control,* Master's Thesis, Virginia Polytechnic Institute and State University, August 2001.

[26] Langhorne, P.J., Dowling, A.P., Hooper, N., *Practical Active Combustion Control System for Combustion Oscillations,* Journal of Propulsion and Power, Vol. 6 No 3, pp. 324-333, 1990.

[27] Lefebvre, A.H., *Atomization and Sprays,* New York: Hemisphere Pub. Corp., 1989.

[28] Liao, Y., Sakman, A.T., Jeng, S.M., Jog, M.A., Benjamin, M.A., *A Comprehensive Model to Predict Simplex Atomizer Performance,* Journal of Engineering for Gas Turbines and Power, Vol. 121, pp. 285-294, 1999.

[29] Lyons, J.L., *Lyons' Valve Designer's Handbook,* New York: Van Nostrand Reinhold Co., 1982.

[30] McManus, K.R., *The Effects of Controlling Vortex Formation on the Performance of a Dump Combustor,* Ph.D. Dissertation, Stanford University, 1990.

[31] Morse, P.M., Ingard, U., *Theoretical Acoustics,* Princeton University Press, 1968.

[32] Munt, R.M., *The Interaction of Sound With a Subsonic Jet Issuing from a Semi-Infinite Cylindrical Pipe,* Journal of Fluid Mechanics, Vol. 83, pp. 609-640, 1977.

[33] Neumeier, Y., Lubarsky, E., Heising, R., Israeli, O., Neumaier, M., Zinn, B.T., *Liquid Injector Actuator for Control of Combustion Processes,* 34th Aerospace Sciences Meeting and Exhibit, AIAA 98-3540.

[34] Pierce, A.D., *Acoustics - An Introduction to Its Physical Principles and Applications,* Acoustical Society of America, 1989.

[35] Poinsot, T., Trouve, A., Veynante, D., Candel, S., Esposito, E., *Vortex-Driven Acoustically Coupled Combustion Instabilities,* Journal of Fluid Mechanics, Vol. 177, pp. 265-292, 1987.

[36] Richards, J.S., *An Exploration of Secondary Fuel Injection as Actuation For Control of Combustion Instabilities in a Laminar Premixed Tube Combustor,* Master's Thesis, Virginia Polytechnic Institute and State University, May 2000.

[37] Rienstra, S.W., Hirschberg, A., *An Introduction to Acoustics,* website: http://www.win.tue.nl/~sjoerdr/papers/boek.pdf.

[38] Rump, K.M., Heister, S.D., *Modeling the Effect of Unsteady Chamber Conditions on Atomization Processes,* Journal of Propulsion and Power, Vol. 14 No. 4, pp. 576-578, 1998.

[39] Saunders, W.R., Vaudrey, M.A., Eisenhower, B.A., Vandsburger, U., Fannin, C.A., *Perspectives on Linear Compensator Design for Active Combustion Control,* 37th AIAA Aerospace Sciences Meeting, AIAA 99-0717.

[40] Straub, D.L., Richards, G.A., *Effect of Fuel Nozzle Configuration on Premix Combustion Dynamics,* ASME 98-GT-492. Stockholm, Sweden, 1998.

[41] Washio, S., Takahashi, S., Yonguang, Y., Yamaguchi, S., *Study of Unsteady Orifice Flow Characteristics in Hydraulic Oil Lines,* Journal of Fluids Engineering, Vol. 118, pp. 743-748, 1996.

[42] Yu, K., Wilson, K.J., Schadow, K.C. *Active Instability Suppression by Controlled Injection of Liquid Fuel,* 33rd AIAA/ASME/SAE/ASEE Joint Propulsion Conference, AIAA 97-3324.

Appendix A: Specifications of Several Delevan Atomizers

The atomizers used in this study were a pressure-swirl (simplex) type, used in the VACCG combustor in a non-premixed, swirl-stabilized setup. It should be noted that transition of the current combustor to accommodate an LDI configuration will require the use of this type of atomizer, and the intent of the present research was to provide preliminary baseline performance characteristics of such a configuration. The specifications for these atomizers are shown in Table A.1.

Contact information: Delevan, Inc. Fuel Metering Products, P.O. Box 969, Hwy 302 South, Bamberg, South Carolina 29003, website: www.delavan.co.uk.

Table A.1: Specifications for several Delevan atomizers.

Atomizer Part Number	**Flow Number (lb/hr/$\sqrt{\text{psi}}$)**	**Pressure Lower Bound (psi)**	**Flow Rate Lower Bound (gph)**	**Orifice Diameter (in)**
WDB 0.40	0.26	75	0.31	0.008
WDB 0.50	0.32	75	0.39	0.0083
WDB 0.75	0.48	75	0.58	0.0092
WDB 1.00	0.64	75	0.77	0.011
WDB 2.00	1.28	75	1.55	0.013
WDB 3.00	1.93	75	2.32	0.015
WDB 4.00	2.57	40	2.26	0.016

Appendix B: Actuator Specifications

The piezoelectric drivers and amplifiers used in this work were manufactured by Piezomechanik GmbH. These actuators had specifications as shown in Table B.1. The specifications for the amplifiers are shown in Table B.2. The LE150/14/20 amplifier was chosen for the PSt150/14/20 actuator, and two LE1000/100 amplifiers were chosen for the PSt1000/10/150 and PSt1000/16/500 actuators. The RCV1000/7 amplifier was a switching amplifier that was used to experiment with the bandwidth capabilities of the PSt1000/16/500 actuator. The amplifier uses the reactive energy generated by the actuator to boost the instantaneous current output of the amplifier. It can be seen that the amplifier may provide seven times the instantaneous current of the conventional LE1000/100 amplifier. It was advised by the manufacturer to run at high frequencies (above 200 Hz) for only a short period of time in order to avoid excessive thermal loading that can potentially damage the stack.

Contact information: Piezomechanik attn: Dr. Lutz Pickelmann, Berg-am-Laim-Str.64, D-81673 Mnchen, website: www.piezomechanik.com.

[1]There were two LE 1000/100 amplifiers dedicated for each of the PSt 1000/10/150 and PSt 1000/16/500 actuators.

Table B.1: Piezoelectric actuator specifications.

Specification	**PSt150/14/20**	**PSt1000/10/150**	**PSt1000/16/500**
Length (in)	1.4	5.7	17
Free Displacement: Reported/Measured (μm)	20.9/20	150/–	500/453
Blocked Force (lbf)	1570	900	2700
Max. Tensile Force (lbf)	225	160	340
Resonance: Reported/Measured (kHz)	30/7	5/–	1.8/–
Electrical Capacitance (μF)	7.2	0.39	2.1
Stiffness: Reported/Measured (N/μm)	250/202	17/–	17/15
g_{33} (m^2/C)	13.2	24.4	–
c_{33}^E (pC/N)	18.1	18.7	–
d_{33} (pm^2/N)	650	410	–

Table B.2: Driving amplifier specifications.

Specification	**LE150/200**	**LE1000/100**[1]	**RCV1000/7**
Input Voltage Range (V)	0-5	0-5	0-5
Output Voltage Range (V)	0-150	0-1000	0-1000
Max. Current (A)	2	1	7
Full-Scale Bandwidth (Hz) @ Capacitance (μF)	590 @ 7.2	816 @ 0.39 150 @ 2.1	1300 @ 2.1
Max. Power (W)	300	1000	2200

Appendix C: MATLAB-Generated Transmission Line Models

Piston-Atomizer Model

```
% Piston-atomizer acoustic model
% tube with atomizer driven by piston with two side-branches.
%
% Jonathan DeCastro
% 9/11/02

clear all
close all

%system inputs
f = linspace(0,800,800); %frequency range, Hz
Vref = .707*0.02; %rms reference voltage, V
DeltaP = 230; %mean atomizer pressure drop, psi
R = sqrt(125)/1; %atomizer resistance, sqrt(psi)/gph
no_turns = 1; %supply valve # of turns open

Vair_amb = 3e-8; %piston air volume (ambient), m^3
Vair_ambn = 2e-8; %nozzle air volume (ambient), m^3

% section 1: piston chamber
D1 = 1.5*.0254; %m
S1 = pi*D1^2/4;
L1 = 0.625*.0254; %m

% section 2: area reduction between chamber and tube
D2 = 0.8*.0254; %m
S2 = pi*D2^2/4;
L2 = 0.8*.0254; %m

% section 3: inlet tube
D3 = 0.175*.0254; %m
S3 = pi*D3^2/4;
L3 = 3.75*.0254; %m

% section 4, inlet valve chamber
D4 = 0.175*.0254; %m
S4 = pi*D4^2/4;
L4 = 0.785*.0254; %m

% section 5, inlet valve constriction
L5 = 0.5*.0254; %m

% section 5a, inlet tube
D5a = 0.175*.0254; %m
S5a = pi*D5a^2/4;
L5a = 2*.0254; %m

% section 6: tube length between piston and bleed branch
D6 = 0.175*.0254; %m
S6 = pi*D6^2/4;
L6 = 11.625*.0254; %m

% section 7: bleed branch
```

```
D7 = 0.175*.0254; %m
S7 = pi*D7^2/4;
L7 = 3*.0254; %m

% section 8, bleed valve chamber
D8 = 0.52*.0254; %m
S8 = pi*D8^2/4;
L8 = 0.785*.0254; %m

% section 9: tube coil between bleed branch and end section
D9 = 0.175*.0254; %m
S9 = pi*D9^2/4;
L9 = (5*12+11.75)*.0254; %m

% section 10: tube at end section, before atomizer
D10 = 0.175*.0254; %m
S10 = pi*D10^2/4;
L10 = 3.285*.0254; %m

%atomizer dimensions
Dn1 = 0.52*.0254;  %m
Sn1 = pi*Dn1^2/4;
Ln1 = 0.2*.0254; %m

Dn2 = 0.08*.0254;  %m
Sn2 = pi*Dn2^2/4;
Ln2 = 0.02*.0254; %m

Dn3 = 0.15*.0254; %m
Sn3 = pi*Dn3^2/4;
Ln3 = 0.2*.0254; %m

Wn4 = 1.5/64/2*.0254; %m
Sn4 = 4*Wn4^2;
Ln4 = 0.03*.0254; %m
Dn4 = sqrt(4*Sn4/pi); %m

Dn5 = 0.01*.0254; %m
Sn5 = pi*Dn5^2/4;
Ln5 = 0.04*.0254; %m

%Dn6 = 0.0002; %0.4 orifice, m
Dn6 = 0.00028; %1.0 orifice, m
Sn6 = pi*Dn6^2/4;
Ln6 = 0.02*.0254; %m

L_meas1 = L6 - 4.625*.0254; %transducer location #2, m
L_meas2 = L9 - 3*.0254; %transducer location #5, m

P0 = (DeltaP + 14.7)*6894.76; %mean pressure, Pa

%liquid parameters
rho_1 = 997; %density, kg/m^3
c_1 = 1440; %sound speed, m/s
mu = 8.55e-4; %viscosity, kg/(m*s)
Pr = 5.83; %Prandtl Number
be = 1.53e-4; %thermal expansion coefficient, 1/K
cp = 4.179; %specific heat, kJ/(kg*K)
T = 300; %ambient temperature, K
SG = rho_1/997; %specific gravity

%air parameters
gamma = 1.4; %adiabatic specific heat ratio
R = 8314.5; %universal gas constant, J/(kmol*K)
```

```
mw = 28.85;     %molecular weight, kg/kmol
Rair = R/mw; %gas constant, J/(kg*K)
rho_2 = P0/(Rair*T); %density, kg/m^3
c_2 = sqrt(gamma*Rair*T); %sound speed, m/s

rc = rho_1*c_1; %specific acoustic impedance

w = 2*pi*f;
k_0 = w/c_1; %wave number

% absorption coefficient
delta = mu/(2*rho_1)*(4/3 + T*be^2*c_1.^2/cp/Pr);
eta = sqrt(w*mu/(rho_1*c_1.^2));
alpha_c = w.^2.*delta./c_1.^3; %classical absorption coefficient
alpha_w = 2^(-3/2)*eta.*(1 + T*be^2*c_1.^2/cp/Pr^.5)*pi*D4/S4; %viscosity absorption coefficient
k_1 = k_0 + (1 - j)*alpha_w;

% %mechanical impedance of stack & piston
ka = 202e6*877e5/(202e6 + 877e5); %stiffness (stack & bracket), N/m
ma = 0; %mass, kg
ca = 0; %damping, kg/s
Z_m = ca + j*(w*ma - ka*ones(size(w))./w); %mechanical impedance

Gp = ka*20e-6/148; %piezo constant, ka*d33*L/t, N/V
Ga = 30; %amplifier gain, Vstack/Vref

% nozzle orifice and impedance calculations
FN = 1/R*8.3454e-03*rho_1*1.5174e-006; %atomizer flow number, kg/s/sqrt(Pa)
Qn = FN*sqrt(DeltaP*6894.76)/rho_1; %mean flow rate, m^3/sec
t_o = 2.7*(Dn6*FN*mu/(rho_1*sqrt(DeltaP)))^0.25; %film sheet thickness, m

if t_o < Dn6/2
   Sn6 = pi/4*(Dn6^2 - (Dn6 - 2*t_o)^2);
end
Dn6 = sqrt(4*Sn6/pi);

Z_L = (0*j + 1e-20)*rc*ones(size(w)); %pressure release

% inlet valve orifice and impedance calculations
Cd = 0.6;
if no_turns <= 1
   Cv = 0.0013*no_turns;
else
        Cv = 0.0036*no_turns - 0.0023; %bypass valve flow coefficient, gpm/sqrt(psi)
end

FNv = Cv*60*8.3454E-03*rho_1*1.5174e-006;

S5 = sqrt(rho_1/(2*6895))*Cv*60*1.052e-6/Cd;
D5 = sqrt(4*S5/pi);

Z_5 = 2*rho_1^2*Qn*S5/FNv^2*ones(size(k_0)); %mean gradient
Z_5a = rc*ones(size(w)); %infinite tube

% nozzle impedances
rn2 = Dn2/2;
Z_n2 = (1 - Dn2/Dn1)*(rc*(k_0.^2*rn2^2)./(1 + k_0.^2*rn2^2) + j*w*rho_1*rn2./(1 + k_0.^2*rn2^2)); %junction

rn3 = Dn3/2;
Z_n3 = (1 - Dn2/Dn3)*(rc*(k_0.^2*rn3^2)./(1 + k_0.^2*rn3^2) + j*w*rho_1*rn3./(1 + k_0.^2*rn3^2)); %junction

rn4 = sqrt(Sn4/pi);
Z_n4 = 2*rho_1^2*Qn*Sn4/FN^2 + (1 - Dn4/Dn3)*j*w*rho_1*rn4./(1 + k_0.^2*rn4^2); %mean gradient
```

```
Vn6 = Qn/Sn6;
rn6 = Dn6/2;
Z_n6 = rho_1*Vn6*(Sn5/Sn6 - Sn6/Sn5)*ones(size(k_0)) + (1 - Dn6/Dn5)*j*w*rho_1*rn6./(1 + k_0.^2*rn6^2); %junction

% piston air impedance
La = 0; %m
Sa = L1*D1/2*.0254;
Vair = Vair_amb*(101350/P0)^(1/gamma);
Z_a = Sa*j*(w*rho_1*La/Sa - gamma*P0*ones(size(w))./(Vair*w));

% nozzle air impedance
Sa1 = Ln3*Dn3/2*.0254;
Vairn = Vair_ambn*(101350/P0)^(1/gamma);
Z_an = Sa1*j*(w*rho_1*La/Sa1 - gamma*P0*ones(size(w))./(Vairn*w));

% transmission line matrix
for index = 1:length(k_1)

    k = k_1(index);
    const = [S1+Z_m(index)/rc S1-Z_m(index)/rc zeros(1,40); %piston face
         S1*exp(-j*k*L1/2) -S1*exp(j*k*L1/2) -S1 S1 zeros(1,14) -Sa Sa zeros(1,22);
         exp(-j*k*L1/2) exp(j*k*L1/2) -1 -1 zeros(1,38);
         exp(-j*k*L1/2) exp(j*k*L1/2) zeros(1,16) -1 -1 zeros(1,22);
         zeros(1,18) (-Z_a(index)/rc + 1)*exp(-j*k*La) (Z_a(index)/rc + 1)*exp(j*k*La) zeros(1,22); %piston air bubble

        0 0 S1*exp(-j*k*L1/2) -S1*exp(j*k*L1/2) -S2 S2 zeros(1,36);
         0 0 exp(-j*k*L1/2) exp(j*k*L1/2) -1 -1 zeros(1,36);

        zeros(1,4) S2*exp(-j*k*L2) -S2*exp(j*k*L2) -S3 S3 -S6 S6 zeros(1,32);
         zeros(1,4) exp(-j*k*L2) exp(j*k*L2) -1 -1 0 0 zeros(1,32);
         zeros(1,4) exp(-j*k*L2) exp(j*k*L2) 0 0 -1 -1 zeros(1,32);
         zeros(1,6) S3*exp(-j*k*L3) -S3*exp(j*k*L3) 0 0 0 0 -S4 S4 zeros(1,28);
         zeros(1,6) exp(-j*k*L3) exp(j*k*L3) 0 0 0 0 -1 -1 zeros(1,28);
         zeros(1,12) S4*exp(-j*k*L4) -S4*exp(j*k*L4) zeros(1,22) -S5 S5 zeros(1,4);
         zeros(1,12) exp(-j*k*L4) exp(j*k*L4) zeros(1,22) (-Z_5(index)/rc - 1) (Z_5(index)/rc - 1) zeros(1,4);
         zeros(1,36) S5*exp(-j*k*L5) -S5*exp(j*k*L5) -S5a S5a 0 0;
         zeros(1,36) exp(-j*k*L5) exp(j*k*L5) -1 -1 0 0;
         zeros(1,38) (-Z_5a(index)/rc + 1)*exp(-j*k*L5a) (Z_5a(index)/rc + 1)*exp(j*k*L5a) 0 0; %inlet branch

        zeros(1,8) S6*exp(-j*k*L6) -S6*exp(j*k*L6) -S9 S9 0 0 0 0 -S7 S7 zeros(1,24);
         zeros(1,8) exp(-j*k*L6) exp(j*k*L6) -1 -1 0 0 0 0 0 0 zeros(1,24);
         zeros(1,8) exp(-j*k*L6) exp(j*k*L6) 0 0 0 0 0 0 -1 -1 zeros(1,24);
         zeros(1,16) exp(-j*k*L7) exp(j*k*L7) zeros(1,22) -1 -1;
         zeros(1,16) S7*exp(-j*k*L7) -S7*exp(j*k*L7) zeros(1,22) -S8 S8;
         zeros(1,40) (-1e50 + 1)*exp(-j*k*L8) (1e50 + 1)*exp(j*k*L8); %bleed branch

        zeros(1,10) S9*exp(-j*k*L9) -S9*exp(j*k*L9) 0 0 -S10 S10 zeros(1,26);
         zeros(1,10) exp(-j*k*L9) exp(j*k*L9) 0 0 -1 -1 zeros(1,26);
         zeros(1,14) S10*exp(-j*k*L10) -S10*exp(j*k*L10) 0 0 0 0 -Sn1 Sn1 zeros(1,20);
         zeros(1,14) exp(-j*k*L10) exp(j*k*L10) 0 0 0 0 -1 -1 zeros(1,20);
        zeros(1,20) Sn1*exp(-j*k*Ln1) -Sn1*exp(j*k*Ln1) -Sn2 Sn2 zeros(1,18);
         zeros(1,20) exp(-j*k*Ln1) exp(j*k*Ln1) (-Z_n2(index)/rc - 1) (Z_n2(index)/rc - 1) zeros(1,18);
        zeros(1,22) Sn2*exp(-j*k*Ln2) -Sn2*exp(j*k*Ln2) -Sn3 Sn3 zeros(1,16);
         zeros(1,22) exp(-j*k*Ln2) exp(j*k*Ln2) (-Z_n3(index)/rc - 1) (Z_n3(index)/rc - 1) zeros(1,16);

         zeros(1,24) Sn3*exp(-j*k*Ln3/2) -Sn3*exp(j*k*Ln3/2) zeros(1,6) -Sn3 Sn3 -Sa Sa zeros(1,6);
         zeros(1,24) exp(-j*k*Ln3/2) exp(j*k*Ln3/2) zeros(1,6) -1 -1 0 0 zeros(1,6);
         zeros(1,24) exp(-j*k*Ln3/2) exp(j*k*Ln3/2) zeros(1,6) 0 0 -1 -1 zeros(1,6);
         zeros(1,34) (-Z_an(index)/rc + 1)*exp(-j*k*La) (Z_an(index)/rc + 1)*exp(j*k*La) zeros(1,6); %nozzle air bubble

         zeros(1,26) -Sn4 Sn4 zeros(1,4) Sn3*exp(-j*k*Ln3/2) -Sn3*exp(j*k*Ln3/2) zeros(1,8);
         zeros(1,26) (-Z_n4(index)/rc - 1) (Z_n4(index)/rc - 1) zeros(1,4) exp(-j*k*Ln3/2) exp(j*k*Ln3/2) zeros(1,8);
         zeros(1,26) Sn4*exp(-j*k*Ln4) -Sn4*exp(j*k*Ln4) -Sn5 Sn5 zeros(1,12);
         zeros(1,26) exp(-j*k*Ln4) exp(j*k*Ln4) -1 -1 zeros(1,12);
```

```
        zeros(1,28) Sn5*exp(-j*k*Ln5) -Sn5*exp(j*k*Ln5) -Sn6 Sn6 zeros(1,10);
        zeros(1,28) exp(-j*k*Ln5) exp(j*k*Ln5) (-Z_n6(index)/rc - 1) (Z_n6(index)/rc - 1) zeros(1,10);
        zeros(1,30) (-Z_L(index)/rc + 1)*exp(-j*k*Ln6) (Z_L(index)/rc + 1)*exp(j*k*Ln6) zeros(1,10)]; %atomizer exit plane

   input = [Gp*Ga*Vref;zeros(41,1)];

   coef = const\input;
   A_1(index) = coef(9);
   B_1(index) = coef(10);
   A_2(index) = coef(15);
   B_2(index) = coef(16);
   A_3(index) = coef(31);
   B_3(index) = coef(32);
end

T_p1 = (A_1.*exp(-j*k_1*L_meas1) + B_1.*exp(j*k_1*L_meas1));
phi_p1 = unwrap(angle(T_p1))*180/pi;
mag_p1 = abs(T_p1);

T_p2 = (A_2.*exp(-j*k_1*L_meas2) + B_2.*exp(j*k_1*L_meas2));
phi_p2 = unwrap(angle(T_p2))*180/pi;
mag_p2 = abs(T_p2);

T_v3 = (A_3.*exp(-j*k_1*Ln6) - B_3.*exp(j*k_1*Ln6))*Sn6/rc;
phi_v3 = unwrap(angle(T_v3))*180/pi;
mag_v3 = abs(T_v3);


figure
subplot(2,1,1)
plot(f,20*log10(mag_p1/1e-6))
title('Post-Piston FRF')
ylabel('Pressure (SPL)')
grid on
subplot(2,1,2)
plot(f,phi_p1)
ylabel('Phase (deg)')
xlabel('Frequency (Hz)')
grid on

figure
subplot(2,1,1)
plot(f,20*log10(mag_p2/1e-6))
title('Pre-Atomizer FRF')
ylabel('Pressure (SPL)')
grid on
subplot(2,1,2)
plot(f,phi_p2)
ylabel('Phase (deg)')
xlabel('Frequency (Hz)')
grid on

figure
subplot(2,1,1)
plot(f,20*log10(mag_v3*951019/Vref))
title(['Post-Atomizer Flow Rate'])
ylabel('Volume Velocity/Input Voltage (dB gal/hr/V)')
grid on
subplot(2,1,2)
plot(f,phi_v3)
ylabel('Phase (deg)')
xlabel('Frequency (Hz)')
grid on
```

Throttle Valve-Atomizer Model

```
% Valve-atomizer acoustic model
% tube driven by throttle valve with supply branch, bypass branch, and atomizer.
%
% Jonathan DeCastro
% 1/27/03

clear all
close all

% system inputs
f = linspace(0,800,800); %frequency range, Hz
Vref = .707*0.02; %rms reference voltage, V
x_off = 700e-6; %mean stack offset, m
DeltaP = 300; %mean atomizer pressure drop, psi
R = sqrt(125)/1; %atomizer resistance, sqrt(psi)/gph
no_turns = 1e-3; %bypass valve # of turns open

Vair_amb = 5e-9; %upstream chamber air, section 3 (ambient), m^3
Vair_amb1 = 6e-9; %downstream chamber air, section 5 (ambient), m^3
Vair_ambn = 1e-8; %nozzle air volume, section N3 (ambient), m^3

% section 1: inlet valve orifice
D1 = 0.1*.0254; %m
S1 = pi*D1^2/4;
L1 = 0.5*.0254; %m

% section 2: inlet tube
D2 = 0.175*.0254; %m
S2 = pi*D2^2/4;
L2 = 9*.0254; %m

% section 3: valve inlet port
D3 = 0.75*.0254; %m
S3 = pi*D3^2/4;
L3 = 0.5*.0254; %m

% section 4: inlet valve chamber
D4 = 2*.0254; %m
S4 = pi*D4^2/4;
L4 = 1.5*.0254; %m

% section 5: bleed port
D5 = 11/32*.0254; %m
S5 = pi*D5^2/4;
L5 = 0.5*.0254; %m

% section 6: bleed branch
D6 = 0.175*.0254; %m
S6 = pi*D6^2/4;
L6 = 5.25*.0254; %m

% section 7: bleed valve area increase
D7 = 0.52*.0254; %m
S7 = pi*D7^2/4;
L7 = 0.785*.0254; %m

% section 8a: valve stem face
D8 = 1.203*.0254; %m
D9 = 1.087*.0254; %m
Dstem = 0.381*.0254; %m
S8a = .005*pi*D8^2/4
S8a1 = .005*(pi*D9^2/4 - pi*Dstem^2/4);
```

```
% section 8b: valve stem clearance
h_off = 0.7071*x_off;
C8 = pi*1.203*.0254; %m
S8b = h_off*C8;
L8b = 0.082*.0254; %m

% section 9: outlet valve chamber
D9 = 1.087*.0254; %m
Dstem = 0.381*.0254; %m
S9 = pi*D9^2/4 - pi*Dstem^2/4;
L9 = 1.5*.0254; %m

% section 10: outlet valve port
D10 = 0.75*.0254; %m
S10 = pi*D10^2/4;
L10 = 1*.0254; %m

% section 11: tube length between outlet and 2nd side branch
D11 = 0.175*.0254; %m
S11 = pi*D11^2/4;
L11 = 14.25*.0254; %m

% section 12: bypass branch
D12 = 0.175*.0254; %m
S12 = pi*D12^2/4;
L12 = 3*.0254; %m

% section 13: bypass valve orifice
D13 = 0.07*.0254; %m
S13 = pi*D13^2/4;
L13 = 0.5*.0254; %m

% section 14: bypass tube
D14 = 0.125*.0254; %m
S14 = pi*D14^2/4;
L14 = 2*.0254; %m

% section 15: tube coil between 2nd side branch and end section
D15 = 0.175*.0254; %m
S15 = pi*D15^2/4;
L15 = (6*12+3)*.0254 + 35.625*.0254; %(8-foot) m

% section 16: area increase at end section
D16 = 0.175*.0254; %m
S16 = pi*D16^2/4;
L16 = 8.25*.0254; %m

% atomizer dimensions
Dn1 = 0.52*.0254; %m
Sn1 = pi*Dn1^2/4;
Ln1 = 0.2*.0254; %m

Dn2 = 0.2*.0254; %m
Sn2 = pi*Dn2^2/4;
Ln2 = 0.02*.0254; %m

Dn3 = 0.15*.0254; %m
Sn3 = pi*Dn3^2/4;
Ln3 = 0.2*.0254; %m

Wn4 = 1.5/64/2*.0254; %m
Sn4 = 4*Wn4^2;
Ln4 = 0.03*.0254; %m
```

```
Dn4 = sqrt(4*Sn4/pi); %m

Dn5 = 0.04*.0254; %m
Sn5 = pi*Dn5^2/4;
Ln5 = 0.04*.0254; %m

%Dn6 = 0.0002; %0.4 orifice, m
Dn6 = 0.00028; %1.0 orifice, m
Sn6 = pi*Dn6^2/4;
Ln6 = 0.02*.0254; %m

L_meas1 = L11 - 11*.0254; %transducer location #4, m
L_meas2 = L16 - 5*.0254; %transducer location #5, m

P0 = (DeltaP + 14.7)*6894.76; %mean pressure, Pa

% liquid parameters
rho_1 = 997; %H20 density, kg/m^3
%rho_1 = 860; %kerosene density, kg/m^3
c_1 = 1450; %H20 sound speed, m/s
%c_1 = 1320; %kerosene sound speed, m/s
mu = 8.55e-4; %viscosity, kg/(m*s)
Pr = 5.83; %Prandtl Number
be = 1.53e-4; %thermal expansion coefficient, 1/K
cp = 4.179; %specific heat, kJ/(kg*K)
T = 300; %ambient temperature, K
SG = rho_1/997; %specific gravity

% air parameters
gamma = 1.4; %adiabatic specific heat ratio
R = 8314.5; %universal gas constant, J/(kmol*K)
mw = 28.85;     %molecular weight, kg/kmol
Rair = R/mw; %gas constant, J/(kg*K)
rho_2 = P0/(Rair*T); %density, kg/m^3
c_2 = sqrt(gamma*Rair*T); %sound speed, m/s
rc = rho_1*c_1; %specific acoustic impedance

w = 2*pi*f;
k_0 = w/c_1; %wave number

% absorption coefficient
delta = mu/(2*rho_1)*(4/3 + T*be^2*c_1.^2/cp/Pr);
eta = sqrt(w*mu/(rho_1*c_1.^2));
alpha_c = w.^2.*delta./c_1.^3; %classical absorption coefficient
alpha_w = 2^(-3/2)*eta.*(1 + T*be^2*c_1.^2/cp/Pr^.5)*pi*D11/S11; %viscosity absorption coefficient
k_1 = k_0 + (1 - j)*alpha_w;

% %mechanical impedance of stack and valve
ka = 16e6; %stiffness (stack & bracket), N/m
ma = 0; %mass, kg
ca = 0; %damping, kg/s
Z_m = ca + j*(w*ma - ka*ones(size(w))./w);

Gp = ka*500e-6/1000; %piezo constant, ka*d33*L/t [N/V]
Ga = 200; %amplifier gain, Vstack/Vref

% empirical pressure gradient source
G = 30.77*6895*0.496*ones(size(w))./(j*w + 0.496); %based on 300-psi upstream pressure, 1.0 atomizer, no bypass, Pa/Vref

% inlet valve impedance
Z_0 = rc*ones(size(w)); %infinite tube

% bypass valve orifice and impedance calculations
Cd = 0.6;
```

```
if no_turns <= 1
   Cv = 0.0013*no_turns;
else
        Cv = 0.0036*no_turns - 0.0023; %bypass valve flow coefficient, gpm/sqrt(psi)
end

FNv = Cv*60*8.3454E-03*rho_1*1.5174e-006;
Qv = FNv*sqrt(DeltaP*6894.76)/rho_1;

S13 = sqrt(rho_1/(2*6895))*Cv*60*1.052e-6/Cd;
D13 = sqrt(4*S13/pi);

Z_13 = 2*rho_1^2*Qv*S13/FNv^2*ones(size(k_0)); %mean gradient
Z_14 = rc*ones(size(w)); %infinite tube

% nozzle orifice and impedance calculations
FN = 1/R*8.3454E-03*rho_1*1.5174e-006; %atomizer flow number, kg/s/sqrt(Pa)
Qn = FN*sqrt(DeltaP*6894.76)/rho_1; %mean flow rate, m^3/sec
t_o = 2.7*(Dn6*FN*mu/(rho_1*sqrt(DeltaP)))^0.25; %film sheet thickness, m

if t_o < Dn6/2
   Sn6 = pi/4*(Dn6^2 - (Dn6 - 2*t_o)^2);
end
Dn6 = sqrt(4*Sn6/pi);

Z_L = (0*j + 1e-20)*rc*ones(size(w)); %pressure release

% throttle valve mean gradient impedance
Ap = pi*((D8 + D9)/2)^2/4;
Ao = pi*((D8 + D9)/2)*x_off;

Cv_1 = 5.886e4*Ao/sqrt(1.3+.2*(Ap^2/Ao^2))/1.316e6;
Z_8b = 2*(Qn + Qv)*S8b/Cv_1*ones(size(w));

% nozzle impedances
rn2 = Dn2/2;
Z_n2 = (1 - Dn2/Dn1)*(rc*(k_0.^2*rn2^2)./(1 + k_0.^2*rn2^2) + j*w*rho_1*rn2./(1 + k_0.^2*rn2^2)); %junction

rn3 = Dn3/2;
Z_n3 = (1 - Dn2/Dn3)*(rc*(k_0.^2*rn3^2)./(1 + k_0.^2*rn3^2) + j*w*rho_1*rn3./(1 + k_0.^2*rn3^2)); %junction

rn4 = sqrt(Sn4/pi);
Z_n4 = 2*rho_1^2*Qn*Sn4/FN^2 + (1 - Dn4/Dn3)*j*w*rho_1*rn4./(1 + k_0.^2*rn4^2); %mean gradient

Vn6 = Qn/Sn6;
rn6 = Dn6/2;
Z_n6 = rho_1*Vn6*(Sn5/Sn6 - Sn6/Sn5)*ones(size(k_0)) + (1 - Dn6/Dn5)*j*w*rho_1*rn6./(1 + k_0.^2*rn6^2); %junction

% upstream air impedance
La = 0; %m
Sa = L4*D4/2*.0254;
Vair = Vair_amb*(101350/P0)^(1/gamma);
Z_a = Sa*j*(w*rho_1*La/Sa - gamma*P0*ones(size(w))./(Vair*w));

% downstream air impedance
Sa1 = L9*D9/2*.0254;
Vair1 = Vair_amb1*(101350/P0)^(1/gamma);
Z_a1 = Sa1*j*(w*rho_1*La/Sa1 - gamma*P0*ones(size(w))./(Vair1*w));

% nozzle air impedance
San = Ln3*Dn3/2*.0254;
Vairn = Vair_ambn*(101350/P0)^(1/gamma);
Z_an = San*j*(w*rho_1*La/San - gamma*P0*ones(size(w))./(Vairn*w));
```

```
% transmission line matrix
for index = 1:length(k_1)

    k = k_1(index);
    const = [(-Z_0(index)/rc + 1) (Z_0(index)/rc + 1) zeros(1,62); %inlet line
         S1*exp(-j*k*L1) -S1*exp(j*k*L1) -S2 S2 zeros(1,60);
         exp(-j*k*L1) exp(j*k*L1) -1 -1 zeros(1,60);
         0 0 S2*exp(-j*k*L2) -S2*exp(j*k*L2) -S3 S3 zeros(1,58);
         0 0 exp(-j*k*L2) exp(j*k*L2) -1 -1 zeros(1,58);
         0 0 0 0 S3*exp(-j*k*L3) -S3*exp(j*k*L3) -S4 S4 zeros(1,56);
         0 0 0 0 exp(-j*k*L3) exp(j*k*L3) -1 -1 zeros(1,56);
         zeros(1,6) S4*exp(-j*k*L4/2) -S4*exp(j*k*L4/2) -S4 S4 zeros(1,24) -Sa Sa zeros(1,28);
         zeros(1,6) exp(-j*k*L4/2) exp(j*k*L4/2) -1 -1 zeros(1,54);
         zeros(1,6) exp(-j*k*L4/2) exp(j*k*L4/2) zeros(1,26) -1 -1 zeros(1,28);
         zeros(1,34) (-Z_a(index)/rc + 1)*exp(-j*k*La) (Z_a(index)/rc + 1)*exp(j*k*La) zeros(1,28); %air bubble

         zeros(1,8) S4*exp(-j*k*L4/4) -S4*exp(j*k*L4/4) -S4 S4 zeros(1,18) -S5 S5 zeros(1,32);
         zeros(1,8) exp(-j*k*L4/4) exp(j*k*L4/4) -1 -1 zeros(1,52);
         zeros(1,8) exp(-j*k*L4/4) exp(j*k*L4/4) zeros(1,20) -1 -1 zeros(1,32);
         zeros(1,30) S5*exp(-j*k*L5) -S5*exp(j*k*L5) -S6 S6 zeros(1,30);
         zeros(1,30) exp(-j*k*L5) exp(j*k*L5) -1 -1 zeros(1,30);
         zeros(1,32) S6*exp(-j*k*L6) -S6*exp(j*k*L6) zeros(1,28) -S7 S7;
         zeros(1,32) exp(-j*k*L6) exp(j*k*L6) zeros(1,28) -1 -1;
         zeros(1,62) (-1e50 + 1)*exp(-j*k*L7) (1e50 + 1)*exp(j*k*L7); %valve bleed

         zeros(1,10) S4*exp(-j*k*L4/4) -S4*exp(j*k*L4/4) -S8a S8a 0 0 0 0 -S8b S8b zeros(1,44);
         zeros(1,10) exp(-j*k*L4/4) exp(j*k*L4/4) -1 -1 zeros(1,50);
         zeros(1,10) exp(-j*k*L4/4) exp(j*k*L4/4) 0 0 0 0 0 0 (-Z_8b(index)/rc - 1) (Z_8b(index)/rc - 1) zeros(1,44);
        zeros(1,12) S8a*exp(-j*k*0) S8a*exp(j*k*0) -(S8a1 + Z_m(index)/rc) -(S8a1 - Z_m(index)/rc) zeros(1,48); %dipole source
         zeros(1,12) exp(-j*k*0) -exp(j*k*0) -1 1 zeros(1,48);
         zeros(1,14) S8a1*exp(-j*k*0) -S8a1*exp(j*k*0) -S9 S9 S8b*exp(-j*k*L8b) -S8b*exp(j*k*L8b) zeros(1,44);
         zeros(1,14) exp(-j*k*0) exp(j*k*0) -1 -1 zeros(1,46);
         zeros(1,16) -1 -1 exp(-j*k*L8b) exp(j*k*L8b) zeros(1,44);

         zeros(1,16) exp(-j*k*0) exp(j*k*0) zeros(1,30) -1 -1 zeros(1,14); %pressure gradient source
         zeros(1,16) S9*exp(-j*k*0) -S9*exp(j*k*0) zeros(1,30) -S9 S9 zeros(1,14);
         zeros(1,48) S9*exp(-j*k*L9/2) -S9*exp(j*k*L9/2) 0 0 -S9 S9 -Sa Sa zeros(1,8);
         zeros(1,48) exp(-j*k*L9/2) exp(j*k*L9/2) 0 0 -1 -1 0 0 zeros(1,8);
         zeros(1,48) exp(-j*k*L9/2) exp(j*k*L9/2) 0 0 0 0 -1 -1 zeros(1,8);
         zeros(1,54) (-Z_a1(index)/rc + 1)*exp(-j*k*La) (Z_a1(index)/rc + 1)*exp(j*k*La) zeros(1,8); %air bubble

         zeros(1,20) -S10 S10 zeros(1,30) S9*exp(-j*k*L9/2) -S9*exp(j*k*L9/2) zeros(1,10);
         zeros(1,20) -1 -1 zeros(1,30) exp(-j*k*L9/2) exp(j*k*L9/2) zeros(1,10);
         zeros(1,20) S10*exp(-j*k*L10) -S10*exp(j*k*L10) -S11 S11 zeros(1,40);
         zeros(1,20) exp(-j*k*L10) exp(j*k*L10) -1 -1 zeros(1,40);
         zeros(1,22) S11*exp(-j*k*L11) -S11*exp(j*k*L11) -S12 S12 -S15 S15 zeros(1,36);
         zeros(1,22) exp(-j*k*L11) exp(j*k*L11) -1 -1 0 0 zeros(1,36);
         zeros(1,22) exp(-j*k*L11) exp(j*k*L11) 0 0 -1 -1 zeros(1,36);
         zeros(1,24) S12*exp(-j*k*L12) -S12*exp(j*k*L12) zeros(1,24) -S13 S13 zeros(1,12);
         zeros(1,24) exp(-j*k*L12) exp(j*k*L12) zeros(1,24) (-Z_13(index)/rc - 1) (Z_13(index)/rc - 1) zeros(1,12);
         zeros(1,50) S13*exp(-j*k*L13) -S13*exp(j*k*L13) zeros(1,8) -S14 S14 zeros(1,2);
         zeros(1,50) exp(-j*k*L13) exp(j*k*L13) zeros(1,8) -1 -1 zeros(1,2);
         zeros(1,60) (-Z_14(index)/rc + 1)*exp(-j*k*L14) (Z_14(index)/rc + 1)*exp(j*k*L14) zeros(1,2); %bypass valve

         zeros(1,26) S15*exp(-j*k*L15) -S15*exp(j*k*L15) -S16 S16 zeros(1,34);
         zeros(1,26) exp(-j*k*L15) exp(j*k*L15) -1 -1 zeros(1,34);
         zeros(1,28) S16*exp(-j*k*L16) -S16*exp(j*k*L16) 0 0 0 0 0 0 -Sn1 Sn1 zeros(1,26);
         zeros(1,28) exp(-j*k*L16) exp(j*k*L16) 0 0 0 0 0 0 -1 -1 zeros(1,26);
         zeros(1,36) Sn1*exp(-j*k*Ln1) -Sn1*exp(j*k*Ln1) -Sn2 Sn2 zeros(1,24);
         zeros(1,36) exp(-j*k*Ln1) exp(j*k*Ln1) (-Z_n2(index)/rc - 1) (Z_n2(index)/rc - 1) zeros(1,24);
         zeros(1,38) Sn2*exp(-j*k*Ln2) -Sn2*exp(j*k*Ln2) -Sn3 Sn3 zeros(1,22);
         zeros(1,38) exp(-j*k*Ln2) exp(j*k*Ln2) (-Z_n3(index)/rc - 1) (Z_n3(index)/rc - 1) zeros(1,22);
        zeros(1,40) Sn3*exp(-j*k*Ln3/2) -Sn3*exp(j*k*Ln3/2) zeros(1,14) -Sn3 Sn3 -Sa Sa zeros(1,4);
         zeros(1,40) exp(-j*k*Ln3/2) exp(j*k*Ln3/2) zeros(1,14) -1 -1 0 0 zeros(1,4);
```

```
          zeros(1,40) exp(-j*k*Ln3/2) exp(j*k*Ln3/2) zeros(1,14) 0 0 -1 -1 zeros(1,4);
          zeros(1,58) (-Z_an(index)/rc + 1)*exp(-j*k*La) (Z_an(index)/rc + 1)*exp(j*k*La) zeros(1,4); %air bubble

          zeros(1,42) -Sn4 Sn4 zeros(1,12) Sn3*exp(-j*k*Ln3/2) -Sn3*exp(j*k*Ln3/2) zeros(1,6);
          zeros(1,42) (-Z_n4(index)/rc - 1) (Z_n4(index)/rc - 1) zeros(1,12) exp(-j*k*Ln3/2) exp(j*k*Ln3/2) zeros(1,6);
         zeros(1,42) Sn4*exp(-j*k*Ln4) -Sn4*exp(j*k*Ln4) -Sn5 Sn5 zeros(1,18);
          zeros(1,42) exp(-j*k*Ln4) exp(j*k*Ln4) -1 -1 zeros(1,18);
          zeros(1,44) Sn5*exp(-j*k*Ln5) -Sn5*exp(j*k*Ln5) -Sn6 Sn6 zeros(1,16);
          zeros(1,44) exp(-j*k*Ln5) exp(j*k*Ln5) (-Z_n6(index)/rc - 1) (Z_n6(index)/rc - 1) zeros(1,16);
          zeros(1,46) (-Z_L(index)/rc + 1)*exp(-j*k*Ln6) (Z_L(index)/rc + 1)*exp(j*k*Ln6) zeros(1,16)]; %atomizer exit plane

   input = [zeros(20,1);Gp*Ga*Vref;zeros(4,1);G(index)*Vref*exp(j*3*pi/2);zeros(38,1)];

   coef = const\input;
   A_1(index) = coef(23);
   B_1(index) = coef(24);
   A_2(index) = coef(29);
   B_2(index) = coef(30);
   A_3(index) = coef(47);
   B_3(index) = coef(48);
end

T_p1 = (A_1.*exp(-j*k_1*L_meas1) + B_1.*exp(j*k_1*L_meas1));
phi_p1 = unwrap(angle(T_p1))*180/pi;
mag_p1 = abs(T_p1);

T_p2 = (A_2.*exp(-j*k_1*L_meas2) + B_2.*exp(j*k_1*L_meas2));
phi_p2 = unwrap(angle(T_p2))*180/pi;
mag_p2 = abs(T_p2);

T_v3 = (A_3.*exp(-j*k_1*Ln6) - B_3.*exp(j*k_1*Ln6))*Sn6/rc;
phi_v3 = unwrap(angle(T_v3))*180/pi;
mag_v3 = abs(T_v3);


figure
subplot(2,1,1)
plot(f,20*log10(mag_p1/1e-6))
title('Post-Valve FRF')
ylabel('Pressure (SPL)')
grid on
subplot(2,1,2)
plot(f,phi_p1)
ylabel('Phase (deg)')
xlabel('Frequency (Hz)')
grid on

figure
subplot(2,1,1)
plot(f,20*log10(mag_p2/1e-6))
title('Pre-Atomizer FRF')
ylabel('Pressure (SPL)')
grid on
subplot(2,1,2)
plot(f,phi_p2)
ylabel('Phase (deg)')
xlabel('Frequency (Hz)')
grid on

figure
subplot(2,1,1)
plot(f,20*log10(mag_v3*951019/Vref))
title(['Post-Atomizer Flow Rate'])
ylabel('Volume Velocity/Input Voltage (dB gal/hr/V)')
```

```
grid on
subplot(2,1,2)
plot(f,phi_v3)
ylabel('Phase (deg)')
xlabel('Frequency (Hz)')
grid on
```

Appendix D: dSPACE GUI for Combustor Control

The dSPACE graphic user interface (GUI) interface used in the throttle valve combustion control experiments on the VACCG combustor outlined in Chapter 4 is shown in Figure D.1. The GUI was developed with C++ code in order for the user to easily perform phase shifting control experiments. The phase shifter consisted of gain and phase adjuster interfaces. Along with the phase shifter, an adaptive control suite developed by Greenwood [12] was also implemented to validate the performance of those algorithms. Throttle valve control required a mean position controller, which could be monitored and controlled in the GUI. Namely, the user may input appropriate values for the compensator gain that affect the controller's rise time and stability characteristics, and the mean pressure reference. For A/D and D/A channel information, the reader is referred to Figure 4.11.

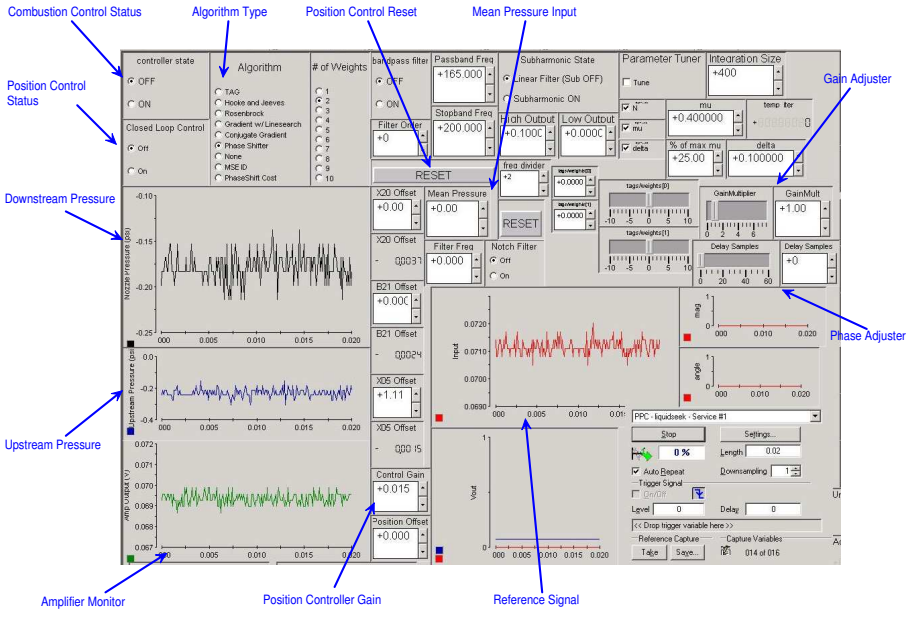

Figure D.1: dSPACE GUI used for combustion control.

Appendix E: Combustor Control Data

Table E.1: Combustor control data with throttle valve; upstream pressure: 430 psi, atomizer: WDA 0.5, data taken on 12/9/02.

Downstream Pressure (psi)	**Air Flow Rate (scfm)**	**Thermal Power (kW)**	**A/F Ratio**	**Equivalence Ratio, ϕ**	**Bypass Valve Turns Open**	**Total Flow Number $\left(\mathrm{lb/hr/\sqrt{psi}}\right)$**	**Reference Voltage Amplitude (V)**	**Percent Modulation (%)**	**Limit Cycle Amplitude (SPL)**	**Amplitude Reduction (dB)**	**Approx. Limit Cycle (Hz)**	**Approx. Phase (deg)**
45	17.5	11.1	37.4	0.40	6.0	8.6	1.4	86	157.3	3.3	105	266
45	19.5	11.1	41.7	0.36	6.0	8.6	1.4	86	157.4	4.1	105	260
45	20.5	11.1	43.9	0.34	6.0	8.6	1.4	86	157.2	4.5	105	260
45	20.7	11.1	44.3	0.34	6.0	8.6	1.4	86	157.3	6.4	105	260
45	20.9	11.1	44.7	0.33	6.0	8.6	1.4	86	157.3	3.5	105	278
45	21.5	11.1	46.0	0.32	6.0	8.6	1.4	86	156.9	8.9	105	248
45	22.5	11.1	48.1	0.31	6.0	8.6	1.6	100	157.2	11.3	105	242
45	23.5	11.1	50.3	0.30	6.0	8.6	1.6	100	157.0	29.0	105	248
55	23.5	12.3	45.5	0.33	6.0	8.6	1.3	62	158.5	3.4	105	266
55	23.5	12.3	45.5	0.33	6.0	8.6	1.3	62	158.5	4.5	105	260
55	24.3	12.3	47.0	0.32	6.0	8.6	0.8	44	156.3	29.3	105	248
55	22.5	12.3	43.5	0.34	6.0	8.6	0.8	44	157.2	5.2	105	266
55	25.1	12.3	48.6	0.31	6.0	8.6	0.8	44	156.1	29.1	105	266
65	23.5	13.3	41.8	0.36	5.3	7.5	1.0	56	158.5	3.1	105	260
65	23.5	13.3	41.8	0.36	5.3	7.5	–	67	166.0	10.6	105	248
65	23.5	13.3	41.8	0.36	5.3	7.5	0.9	41	166.0	9.0	105	260
65	23.5	13.3	41.8	0.36	5.7	8.1	–	100	166.0	10.9	105	260
65	23.5	13.3	41.8	0.36	5.7	8.1	1.0	61	159.1	4.0	105	284
65	23.5	13.3	41.8	0.36	6.0	8.6	1.1	80	159.1	4.2	105	260
65	24.3	13.3	43.3	0.34	6.0	8.6	1.6	100	158.3	6.8	105	260
65	25.2	13.3	44.9	0.33	6.0	8.6	0.8	37	157.5	28.5	105	254
65	25.2	13.3	44.9	0.33	6.0	8.6	0.4	19	157.5	1.4	105	254

Table E.1: (Continued)

Downstream Pressure (psi)	**Air Flow Rate (scfm)**	**Thermal Power (kW)**	**A/F Ratio**	**Equivalence Ratio, ϕ**	**Bypass Valve Turns Open**	**Total Flow Number $\left(\text{lb/hr}/\sqrt{\text{psi}}\right)$**	**Reference Voltage Amplitude (V)**	**Percent Modulation (%)**	**Limit Cycle Amplitude (SPL)**	**Amplitude Reduction (dB)**	**Approx. Limit Cycle (Hz)**	**Approx. Phase (deg)**
65	25.2	13.3	44.9	0.33	6.0	8.6	0.6	30	157.5	2.2	105	254
65	25.2	13.3	44.9	0.33	6.0	8.6	0.8	37	157.5	3.3	105	254
85	25.0	15.3	38.9	0.38	5.0	7.1	1.1	55	159.7	1.8	105	284
85	25.0	15.3	38.9	0.38	5.0	7.1	1.2	62	159.7	2.3	105	260
85	25.0	15.3	38.9	0.38	5.3	7.5	1.2	62	159.7	2.7	105	260
105	25.0	17.0	35.0	0.43	4.0	5.5	1.3	49	160.5	1.1	105	284
105	25.0	17.0	35.0	0.43	5.0	7.1	1.3	77	160.7	1.8	105	272

Table E.2: Combustor control data with throttle valve; upstream pressure: 430 psi, atomizer: WDA 0.5, data taken on 12/11/02.

Downstream Pressure (psi)	**Air Flow Rate (scfm)**	**Thermal Power (kW)**	**A/F Ratio**	**Equivalence Ratio, ϕ**	**Bypass Valve Turns Open**	**Total Flow Number** $\left(\mathrm{lb/hr/\sqrt{psi}}\right)$	**Reference Voltage Amplitude (V)**	**Percent Modulation (%)**	**Limit Cycle Amplitude (SPL)**	**Amplitude Reduction (dB)**	**Approx. Limit Cycle (Hz)**	**Approx. Phase (deg)**
45	20.5	11.1	43.9	0.34	6.0	8.6	1.1	16	156.9	28.9	105	260
55	22.5	12.3	43.5	0.34	6.0	8.6	0.8	39	157.8	28.8	105	266
55	20.5	12.3	41.6	0.36	6.0	8.6	1.3	78	158.0	29.0	105	266
75	21.5	14.1	35.6	0.42	6.0	8.6	1.4	100	160.6	2.5	105	272
75	22.5	14.1	37.3	0.40	6.0	8.6	–	73	159.4	30.4	105	266
85	22.5	15.1	35.0	0.43	6.0	8.6	1.5	100	160.5	2.4	105	278
85	23.5	15.1	36.6	0.41	6.0	8.6	–	54	159.7	30.7	105	278
85	22.5	15.1	35.0	0.43	4.0	5.5	–	76	160.5	2.2	105	266
85	22.5	15.3	35.0	0.43	6.0	8.6	–	84	160.4	3.4	105	272
85	21.5	15.3	33.5	0.45	6.0	8.6	–	84	161.1	3.2	105	284
85	24.5	15.3	38.1	0.39	6.0	8.6	–	65	159.4	32.4	105	266
85	25.3	15.3	39.4	0.38	6.0	8.6	–	41	159.2	32.2	105	266

Table E.3: Combustor control data with throttle valve; upstream pressure: 480 psi, atomizer: WDA 0.5, data taken on 12/16/02.

Downstream Pressure (psi)	**Air Flow Rate (scfm)**	**Thermal Power (kW)**	**A/F Ratio**	**Equivalence Ratio, ϕ**	**Bypass Valve Turns Open**	**Total Flow Number $\left(\mathrm{lb/hr/\sqrt{psi}}\right)$**	**Reference Voltage Amplitude (V)**	**Percent Modulation (%)**	**Limit Cycle Amplitude (SPL)**	**Amplitude Reduction (dB)**	**Approx. Limit Cycle (Hz)**	**Approx. Phase (deg)**
45	21.5	11.1	46.0	0.32	6.0	8.6	2.4	100	160.4	3.8	98	265
45	23.5	11.1	50.3	0.30	6.0	8.6	2.4	100	158.3	3.9	98	303
45	25.5	11.1	54.6	0.27	6.0	8.6	–	12	156.0	15.0	100	298
65	19.5	13.3	34.7	0.43	6.0	8.6	–	100	162.5	3.2	100	293
65	21.5	13.3	38.3	0.39	6.0	8.6	2.8	100	162.4	3.2	103	267
65	23.5	13.3	41.8	0.36	6.0	8.6	2.4	85	161.5	3.6	101	295
65	25.5	13.3	45.4	0.33	6.0	8.6	2.3	97	160.3	4.1	103	290
65	27.5	13.3	49.0	0.30	6.0	8.6	2.4	12	157.4	23.4	103	295
85	22.5	15.3	35.0	0.43	5.5	7.9	2.5	80	162.9	2.2	107	241
85	24.5	15.3	38.1	0.39	5.5	7.9	–	80	163.0	4.7	107	277
85	27.1	15.3	42.2	0.35	5.3	7.5	–	80	162.8	4.9	107	277
85	28.3	15.3	44.1	0.34	5.5	7.9	–	16	160.3	26.3	107	241
100	24.5	16.5	35.2	0.42	5.5	7.9	–	63	163.7	3.0	104	275
100	26.5	16.5	38.0	0.39	5.5	7.9	2.0	62	163.3	3.9	104	263
100	28.5	16.5	40.9	0.36	5.5	7.9	2.0	63	162.7	8.8	104	246
100	30.3	16.5	43.5	0.34	6.0	8.6	–	37	157.0	14.5	103	295

Vita

Jonathan A. DeCastro was born in November 8, 1977 and raised in Farmington, New York, a small town outside Rochester. During his childhood, he enjoyed his many interests, such as playing basketball, going downhill skiing, playing guitar, and watching Star Trek reruns. In 1992, Jonathan attended his first class as a freshman at McQuaid Jesuit High School, where he would embark on several curricular and extracurricular activities. There, he played more basketball and became involved with lacrosse and track. In 1996, he would enroll at Virginia Tech in the Aerospace Engineering program. Looking for a change, he switched majors to Mechanical Engineering to explore a more broad range of topic areas and graduated Cum Laude in 2001. As a natural extension of his senior design project, he sought a graduate degree in the topic area of active combustion control, under Dr. William Saunders. In February 2003, he successfully defended his thesis and plans to start a career, build his own house, and enjoy the outdoors.